154
2-3-95 JS

ANL-94/39

Energy Technology Division
Energy Technology Division
Energy Technology Division
Energy Technology Division
Energy Technology Division
Energy Technology Division

Practical Superconductor Development for Electrical Power Applications

Annual Report for FY 1994

Argonne National Laboratory, Argonne, Illinois 60439
operated by The University of Chicago
for the United States Department of Energy under Contract W-31-109-Eng-38

DISTRIBUTION OF THIS DOCUMENT IS UNLIMITED

Argonne National Laboratory, with facilities in the states of Illinois and Idaho, is owned by the United States government, and operated by The University of Chicago under the provisions of a contract with the Department of Energy.

DISCLAIMER

This report was prepared as an account of work sponsored by an agency of the United States Government. Neither the United States Government nor any agency thereof, nor any of their employees, makes any warranty, express or implied, or assumes any legal liability or responsibility for the accuracy, completeness, or usefulness of any information, apparatus, product, or process disclosed, or represents that its use would not infringe privately owned rights. Reference herein to any specific commercial product, process, or service by trade name, trademark, manufacturer, or otherwise, does not necessarily constitute or imply its endorsement, recommendation, or favoring by the United States Government or any agency thereof. The views and opinions of authors expressed herein do not necessarily state or reflect those of the United States Government or any agency thereof.

Reproduced from the best available copy.

Available to DOE and DOE contractors from the
Office of Scientific and Technical Information
P.O. Box 62
Oak Ridge, TN 37831
Prices available from (615) 576-8401

Available to the public from the
National Technical Information Service
U.S. Department of Commerce
5285 Port Royal Road
Springfield, VA 22161

DISCLAIMER

Portions of this document may be illegible in electronic image products. Images are produced from the best available original document.

Distribution Category:
Electric Power Applications
(UC-1394)

ANL-94/39

ARGONNE NATIONAL LABORATORY
9700 South Cass Avenue
Argonne, Illinois 60439

PRACTICAL SUPERCONDUCTOR DEVELOPMENT FOR ELECTRICAL POWER APPLICATIONS

ANNUAL REPORT FOR FY 1994

U. Balachandran

Contributors:

T. R. Askew
Y. S. Cha
S. E. Dorris
J. T. Dusek
J. E. Emerson
K. C. Goretta
K. E. Gray†
J. D. Hettinger†
J. G. Hu†
J. R. Hull
R. T. Kampwirth†
D. S. Kupperman
M. T. Lanagan
J. S. Luo††
M. Marinelli
V. A. Maroni††
R. L. McDaniel
N. Merchant††
D. J. Miller†
R. C. Niemann
J. J. Picciolo
J. L. Routbort
D. Singh
J. P. Singh
M. Tetenbaum††
V. R. Todt†
K. L. Uherka
C. A. Youngdahl

Energy Technology Division

October 1994

Work supported by

U.S. DEPARTMENT OF ENERGY
Office of Energy Efficiency and Renewable Energy

†Materials Science Division.
††Chemical Technology Division.

MASTER

DISTRIBUTION OF THIS DOCUMENT IS UNLIMITED

Contents

Abstract vii

1 Introduction 1

2 Technical Progress in 1993–1994 1

2.1 Bi–Pb–Sr–Ca–Cu–O Superconductors 1

2.1.1 Phase Development 1

2.1.2 Tape and Coil Development 9

2.2 Tl–M–Sr–Ba–Ca–Cu–O Superconductors 27

2.2.1 Technical Achievement and Progress 27

2.2.2 Planned Activities 32

2.3 YBCO and HBCCO Superconductors 33

2.3.1 Melt–Processed YBCO 33

2.3.2 HBCCO and New Materials 35

2.4 Properties of Bulk High–T_c Superconductors 36

2.4.1 Characterization Methods 36

2.4.2 Electrical Characterization of Superconductors 36

2.4.3 Contact Resistivity 39

2.4.4 Mechanical Properties 40

2.4.5 Nondestructive Evaluation 42

2.5 Applications and Devices 47

2.5.1 Operation of R & A Superconducting Magnet 47

2.5.2 Measurement Facilities 48

2.5.3 Current–Lead Performance 48

2.5.4 Superconducting Magnetic Bearings 51

2.6 Fundamental Studies 54

2.6.1 Evaluation of Weak Links 54

2.6.2 Vortex Motion 54

2.7 Additional Interactions 56

References 56

Figures

1 J_c versus total heat-treatment time at 825°C in 8% O_c for PIT specimens with $Pb_{0.4}$ (with trace Ca_2PbO_4), $Pb_{0.4}$ (no Ca_2PbO_4), and $Pb_{0.3}$ (no Ca_2PbO_4) 3

2 Microstructure of "standard" $Sr_{2.0}$ sample and $Sr_{1.9}$ sample after 50 h at 825°C in 8% O_2 4

3 EMF results by oxygen titration for Pb-doped Bi-2212 powder 6

4 Comparison of EMF results for Pb-doped Bi-2212 and Pb-doped Bi-2223 at 815°C 7

5 Comparison of log pO_2 versus reciprocal absolute temperature in lower plateau region for Pb-doped Bi-2212, Pb-doped Bi-2223, and the CuO-Cu_2O system 8

6 FTIR spectra recorded for KBr pellets containing three Bi-2223 powders with different total carbon levels as indicated 9

7 Adjusted infrared spectra of samples 414-5-2 and 400-145-2 10

8 Raman microprobe spectra of Bi-2212 grain in a pressed pellet containing mostly Bi-2212, with Ca_2PbO_4 as a minor second phase; multiphase region of the same pellet; and Ca_2PbO_4 dispersed in a KBr pellet 11

9 Imaging Raman microscope (IRM) study of a Bi-2212 pressed pellet containing Ca_2PbO_4 as a second phase 12

10 Filling Ag tubes with precursor powder 13

11 High-T_c test magnet fabricated from 16 pancake coils 13

12 Field generated by high-T_c magnet vs. background field at 4.2 and 27 K 14

13 I_c at 77 K of conductor containing 37 filaments 14

14 Texture factor for Bi-2223 and Bi-2212, and ratio of Bi-2223 to Bi-2212 + Bi-2223 15

15 Texture factor for Bi-2223, and the ratio of Bi-2223 to Bi-2212 + Bi-2223 16

16 Computer-assisted image analysis of grain orientation across thickness of tape for one-powder composite heat treated at 825°C in 7.5% O_2 for 100 min and 5400 min 17

17 Scanning electron microscope images of warped specimen and as-rolled specimen of two-powder Bi-2223/Ag composite conductor after heat treatment at 820°C in 7.5% O_2 for 150 h 18

18 Differential thermal analysis curve for "liquid phase" composition detected in one-powder Bi-2223/Ag composite 19

19 Conversion vs. temperature plot for MP-361 and OP-361 Bi-2223/Ag multifilaments heat treated in 7.5% O_2 for 1500 min; conversion vs. time plot for MP-361 and OP-361 Bi-2223/Ag multifilaments heat treated at 810°C in 7.5% O_2 20

20 Bi-2223 tapes were fabricated from our two-powder process and given a series of annealings at 815°C in 8% O_2/92% N_2 21

21 Improvement of J_c by heat treatment of PIT tapes with intermittent pressing..... 21

22 Dependence of J_c on tape thickness 21

23 Variation of J_c with sintering temperature 22

24 Longitudinal view showing two of four wires in core of sample made by the Ag wire-in-tube method 24

25 Schematic diagram of flowing powder 25

26 Dilatometer data for bulk Bi-2223 sample 26

27 Density improvement by intermittent CIPing 26

28 Onset of melting correlated with J_c for Tl-1223 tapes 28

29 Bright-field transmission electron micrograph and selected area diffraction patterns from indicated regions for (Tl,Bi)-1223 wire in as-rolled condition 30

30 Scanning electron micrographs of sandwich-type conductor prepared with plate-shaped Tl-1223 grains 31

31 Levitation force vs. distance between YBCO superconductors and permanent magnet 34

32 Photograph of harvested Nd-123 seed crystals 35

33 Critical current test data from sinter-forged Bi-2223 bar at 77 K 37

34 J_c variation with temperature of sample sectioned from sinter-forged Bi-2223 bar 37

35 Power loss vs. AC current in sinter-forged Pb-BSCCO bar at 77 K 38

36 AC downlinks 39

37 Schematic stress/strain curves at 825°C for materials shown 42

38 Variation of ultrasonic echo transit time relative to that at 780°C for ribbon consisting of NaCl sheathed with Ag 44

39 Change in ultrasonic echo transit time vs. NaCl volume fraction 45

40 Change in ultrasonic echo transit time as a function of temperature for three phase-pure Tl-1223/Ag ribbons 45

41 Change in ultrasonic echo transit time as a function of temperature for three doped Tl-1223/Ag ribbons 46

42 Change in ultrasonic echo transit time as a function of temperature for Bi-2223/Ag ribbons provided by ASC 46

43 Residual strains in Bi-2223/Ag monofilament supplied by ASC 47

44 Variation of magnetic flux density with current at center of R & A magnet 49

45 Heat leak rate as a function of liquid-He level in cryostat 49

46 Rotational rate vs. time for vacuum spin-down of 11.3 g permanent magnet disk rotor 53

47 Magnet and cryochamber used in large FTA vacuum chamber 53

48 Plots of electric field vs. critical current density for Tl-2212 films and J_c vs. field for Tl-2212 films 55

Tables

1 Effect of oxygen pressure on phase stability of Ag/Bi-2223 composite made with Pb-doped Bi-2223 5

2 Summary of powder flow characteristics 25

3 Electrical properties during thermomechanical sequence 26

4 Summary of property data for monolithic and fiber/composite bars 41

PRACTICAL SUPERCONDUCTOR DEVELOPMENT FOR ELECTRICAL POWER APPLICATIONS

ANNUAL REPORT FOR FY 1994

Abstract

Development of useful high-critical-temperature superconductors requires synthesis of superconducting compounds; fabrication of wires, tapes, and films from these compounds; production of composite structures that incorporate stabilizers or insulators; and design and testing of efficient components. This report describes technical progress of research and development efforts aimed at producing superconducting components in the Y-Ba-Cu, (Bi,Pb)-Sr-Ca-Cu, (Tl,Pb,Bi)-(Ba,Sr)-Ca-Cu, and Hg-Ba-Ca-Cu-O oxide systems. Topics discussed are synthesis and heat treatment of high-T_c superconductors, formation of monolithic and composite conductors, characterization of structures and superconducting and mechanical properties, and fabrication and testing of prototype components. Collaborations with industry and academia are documented.

1 Introduction

The superconductor program at Argonne National Laboratory (ANL) includes bulk and film processing development directed toward improving the properties of high-T_c superconductors, developing processing methods for production of commercial conductors, and fabricating and testing prototype conductors. Team relationships with industrial and academic partners are integral to this program. The principal objective of the ANL program is to develop methods to fabricate and use structurally reliable high-T_c superconductors for the generation, transmission, and storage of electrical energy. Ceramic processing and joining techniques are being developed to provide useful conductors from one or several of the high-T_c superconductors. Work has focused on superconductors based on yttrium-barium-copper oxide (YBCO), bismuth-strontium-calcium-copper oxide, lead-doped bismuth-strontium-calcium-copper oxide, pure and metal-doped (M, where M is bismuth, lead, vanadium, chromium, or neodymium) thallium-strontium-barium-calcium-copper oxide, and mercury-barium-calcium-copper oxide (HBCCO).

There are several requirements for monolithic and composite conductors in the form of wires, tapes, films, or other shapes. For most applications, the conductors must be capable of carrying large currents in the presence of large magnetic fields and must be strong, flexible, and chemically and cryogenically stable. Potential applications for such conductors include transmission lines, motors, generators, transformers, magnetic energy storage devices, and electronics. The principal impediments to the use of bulk high-T_c superconductors are low critical current density (J_c) in large applied magnetic fields, relatively poor mechanical properties, and need for very long lengths with uniform properties. Processing methods for the improvement of all have been and continue to be developed. The goals of ceramic fabrication include promoting high conductivity by obtaining phase-pure final materials and imparting favorable grain alignment, maximizing flux pinning through microstructural control, and increasing flexibility and reliability by minimizing microstructural flaws and optimizing the strength and toughness of each material.

This report reviews the technical progress and status of (1) Bi-based and Tl-based high-T_c wires and tapes, which constitute the main focus of materials efforts; (2) YBCO and HBCCO superconductors; (3) characterization of superconducting and electrical properties, microstructures, and mechanical properties; (4) investigations of fundamental properties; and (5) fabrication and testing of prototype superconducting devices. Interactions with industry and academia are also documented.

2 Technical Progress in 1993–1994

2.1 Bi–Pb–Sr–Ca–Cu–O Superconductors

2.1.1 Phase Development

Work on the two-powder process has focused on improving the alignment and connectivity of Bi-2223 grains to increase the J_c of powder-in-tube (PIT) tapes. The two-powder process provides good control over the final microstructure. In the past year, effects of total Pb-content and Sr-content on the microstructures and properties of tapes were explored. Only the composition of the Bi-2212 intermediate precursor was changed; all other aspects of the two-powder process were the same as described previously (Dorris et al., 1993; Poeppel et al., 1993).

In work (Dorris et al., 1994) on how the methods for introducing Pb to Bi-2223 affect phase development and properties of 2223 tapes, it was found that incorporating Pb directly into the 2212 phase is greatly superior to introducing Pb through an additional compound such as Ca_2PbO_4 or PbO. This conclusion was supported by microstructural evidence on both the micrometer and nanometer scale and by inductive T_c traces, but the most dramatic evidence was that the J_c (0 T, 77 K) values progressively and consistently increased as the Ca_2PbO_4 content of the starting powder decreased and the Pb-content of 2212 increased.

To determine whether the improvement in J_c resulted from the decrease in Ca_2PbO_4 content or the increase in Pb content of 2212, PIT tapes were fabricated from three powders [partly in collaboration with American Superconductor Corporation (ASC)]. The first powder was made by the standard two-powder process and consisted of $Bi_{1.8}Pb_{0.4}Sr_{2.0}Ca_{1.0}Cu_{2.0}O_8$, Ca_2CuO_3, CuO, and a small amount of Ca_2PbO_4 (estimated by X-ray diffraction to be less than 5 wt.%). A small amount of Ca_2PbO_4 is typically present in the standard two-powder process because the Pb content exceeds the solubility limit for Pb in 2212 (Majewski et al., 1994). The second powder was identical to the first in all respects except that the 2212 had been annealed according to a proprietary ASC process to eliminate Ca_2PbO_4. In the third powder, Ca_2PbO_4 was eliminated by reducing the Pb content to 0.3, which is below the solubility limit for Pb in 2212; the phases present in this powder were $Bi_{1.8}Pb_{0.3}Sr_{2.0}Ca_{1.0}Cu_{2.0}O_8$, Ca_2CuO_3, and CuO. All three powders were then subjected to the same thermomechanical PIT process, resulting in tapes with final core thicknesses of ≈100 μm. J_c (0 T, 77 K) and microstructures of three tapes were compared after heat-treatment times of 50–150 h at 820–825°C in 8% O_2.

The powders with $Pb_{0.4}$, one with Ca_2PbO_4 and one without, were nearly identical in terms of J_c and microstructure at all heat-treatment times, but the $Pb_{0.3}$ sample was significantly different. The J_c data are shown in Fig. 1. Whereas the two $Pb_{0.4}$ samples contained only ≈3–5% second phases after 150 h at 820°C in 8% O_2 and J_c was ≈15,000 A/cm^2, the $Pb_{0.3}$ tape contained ≈15–18% second phases and was essentially nonsuperconducting for all heat-treatment times. These results show that a small change in overall composition can significantly alter the final microstructure, and indicate that the total Pb content is more important than the presence of a small amount of Ca_2PbO_4. The results are consistent with the idea that formation of a Pb-rich liquid is important for the formation of Bi-2223. It is reasonable to believe that the two $Pb_{0.4}$ samples form a Pb-rich liquid because they exceed the solubility limit for Pb in 2212, but the $Pb_{0.3}$ sample does not form the liquid because its Pb content is below the solubility limit. As a result, Bi-2223 formation is much slower in the $Pb_{0.3}$ sample and J_c is much lower. Present efforts at ANL are focusing on the two-powder process with Pb contents > $Pb_{0.4}$, to see if increasing the amount of liquid leads to higher density, more extensive grain growth, and better grain-to-grain connectivity.

Scanning electron microscopy (SEM) and energy dispersive analysis of X-rays (EDX) have shown that the second phases of Ag-clad tapes made by the two-powder process consist primarily of the so-called 14:24 alkaline earth cuprate (AEC) phase with a Sr:Ca ratio of ≈3:2 and the 2:1 AEC with a Sr:Ca ratio of ≈1:1. Because Sr is present in the initial phase assemblage only in the 2212, the relatively high Sr contents in the second phases indicate that strontium is exsolved during formation of the Bi-2223 phase; this suggests that the overall Sr-content may be higher than optimum. This speculation is consistent with findings in literature that report the most phase-pure Bi-2223 is obtained with slightly Sr-deficient compositions.

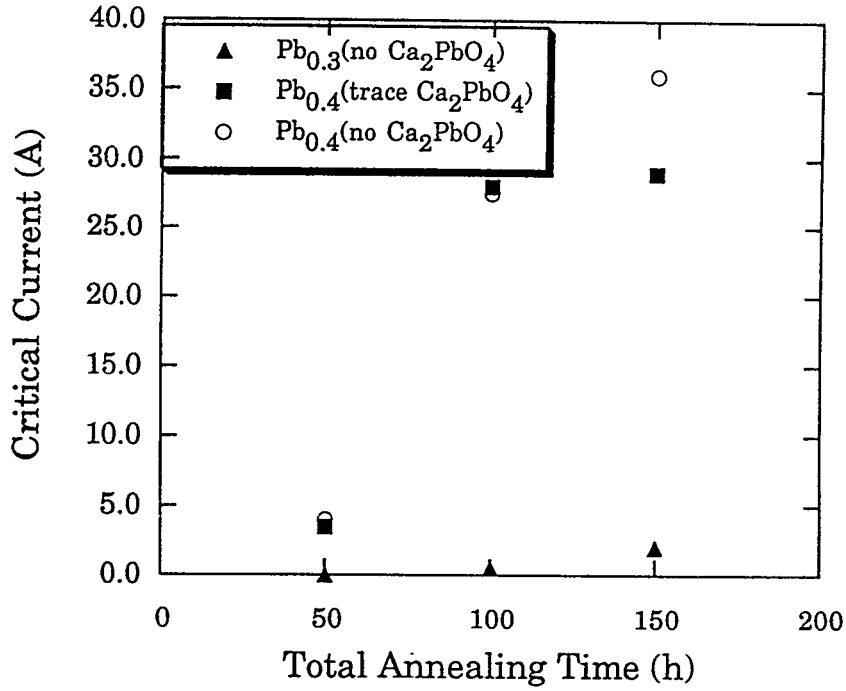

Fig. 1. J_c (0 T, 77 K) versus total heat-treatment time at 825°C in 8% O_2 for PIT specimens with $Pb_{0.4}$ (with trace Ca_2PbO_4), $Pb_{0.4}$ (no Ca_2PbO_4), and $Pb_{0.3}$ (no Ca_2PbO_4). Each J_c (0 T, 77 K) value is average of measurements made on three separate samples.

To study the effect of Sr-content on the microstructure and properties of Bi-2223, PIT tapes were made with the Sr-deficient compositions $Sr_{1.8}$ and $Sr_{1.9}$. The so-called $Sr_{1.9}$ powder consisted of $Bi_{1.8}Pb_{0.4}Sr_{1.9}Ca_{1.0}Cu_{2.0}O_8$, Ca_2CuO_3, and CuO, and the $Sr_{1.8}$ powder consisted of $Bi_{1.8}Pb_{0.4}Sr_{1.8}Ca_{1.0}Cu_{2.0}O_8$, Ca_2CuO_3, and CuO. The only difference between these powders and powder prepared by the standard two-powder process was the total Sr content. Preparation of the powders was identical to the standard process in all other regards. After making PIT tapes from the powders, J_c (0 T, 77 K) was measured and the microstructures were examined by SEM/EDX after heat-treatment times of 50-150 h at 820-825°C in 8% O_2.

Examination of the microstructures revealed two pronounced effects of total Sr content. First, unlike tapes made by the standard two-powder process, where Sr content is $Sr_{2.0}$, the Sr-deficient tapes did not contain Sr-rich 14:24 AEC as a second phase. Instead, the second phases were CuO and 2:1 AEC with a Sr:Ca ratio of ≈1:12. The total Sr content of second phases was significantly lower in the Sr-deficient powders than in the standard powder. These results are consistent with those of Majewsky et al. (1991), who reported the presence of 14:24 at higher Sr contents but not at lower Sr contents. Second, the Bi-2223 grains were noticeably larger and the density was higher in the Sr-deficient compositions. Figure 2 compares the microstructures of a Sr-deficient sample to that of a standard $Sr_{2.0}$ sample. A small change in overall composition significantly influenced the final microstructure. Because larger grain size and higher density may significantly affect the grain connectivity, which may influence superconducting properties, we are continuing to investigate the effects of Sr content on Bi-2223 tapes.

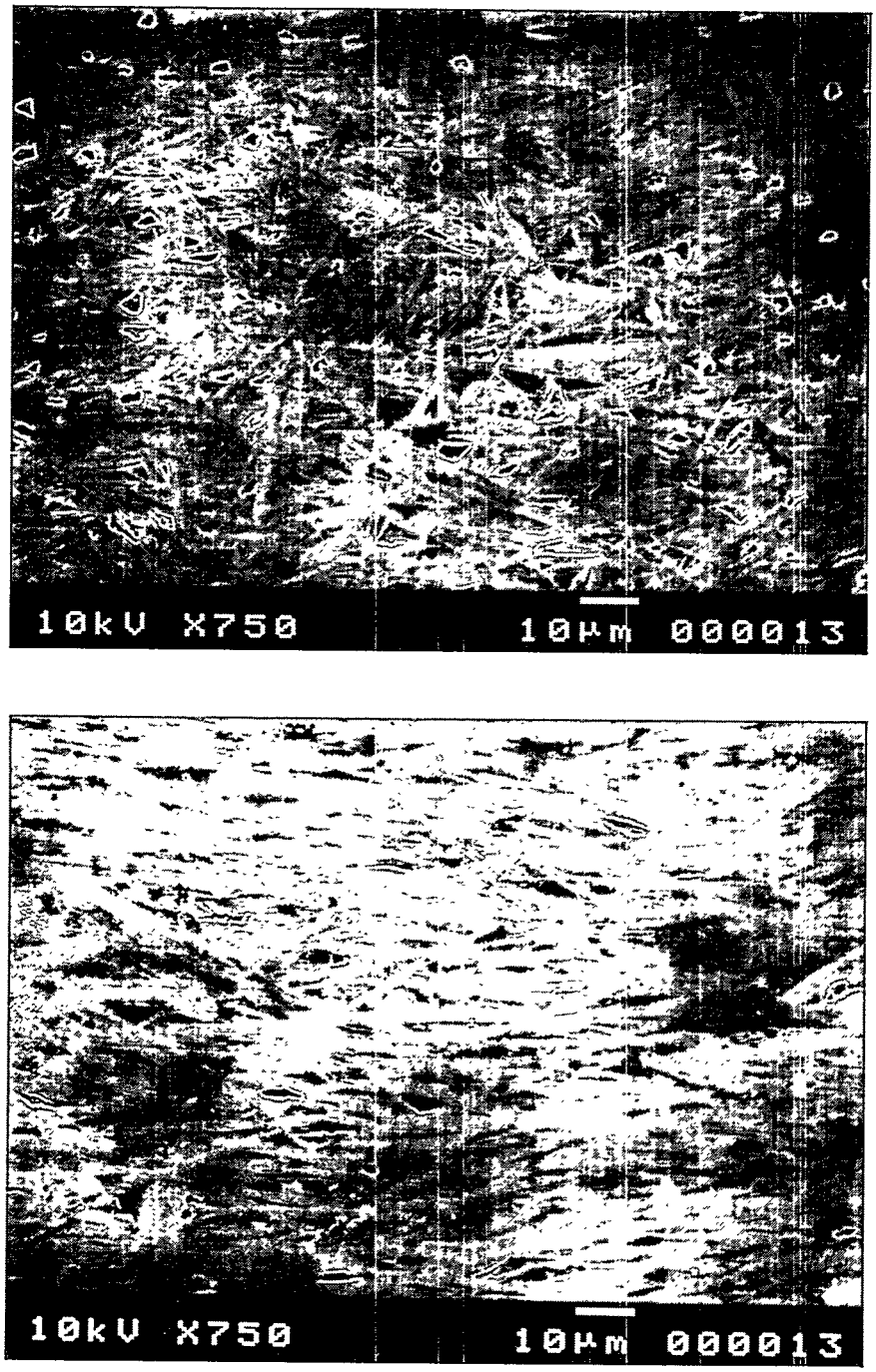

Fig. 2. Microstructure of (a) "standard" $Sr_{2.0}$ sample and (b) $Sr_{1.9}$ sample after 50 h at 825°C in 8% O_2.

Thermodynamics and phase stability of Bi–2212 and Bi–2223

Electromotive force (EMF) measurements of oxygen fugacity as a function of oxygen stoichiometry and temperature in the layered bismuth cuprates are continuing. The coulometric titration technique, employing an yttria–doped zirconia electrolyte, is being used to investigate the thermodynamic behavior of various high–T_c cuprates as a function of oxygen partial pressure (pO_2), oxygen stoichiometry, and temperature. Investigations of

Pb-doped Bi-2223 powder samples prepared at ANL and Ames Laboratory have been reported (Poeppel et al., 1993), and work is now in progress on a Pb-doped Bi-2212 powder.

X-ray diffraction analysis indicated that the as-received Pb-doped Bi-2212 sample was essentially single phase with evidence of a trace of Ca_2PbO_4. Chemical analysis by inductively coupled plasma/atomic emission spectroscopy (ICP/AES), combined with iodometric analysis of the oxygen coefficient, gave the composition as $Bi_{1.82}Pb_{0.40}Sr_{2.10}Ca_{1.04}Cu_{2.00}O_{8.62}$. The results of EMF measurements on this sample are shown in Fig. 3, where equilibrium oxygen pressures calculated for isotherms in the temperature range 700-815°C are plotted as a function of x in Pb-doped $(Bi,Pb)_2Sr_2Ca_2Cu_3O_x$. In accordance with previous measurements on Pb-doped Bi-2223, it is seen that large changes in pO_2 occur as x approaches the lower plateau region. As is shown in Fig. 4, for measurements made at 815°C, the shapes of the isotherms are similar for Pb-doped Bi-2223 and Pb-doped Bi-2212, although there is evidence of a predecomposition of the Bi-2223 sample prior to reaching the final plateau.

Thermodynamic assessments of the partial molar entropy, $\Delta\approx(O_2)$, and enthalpy, $\Delta(O_2)$, of solution of oxygen confirm that the final plateau regions for Bi-2212 and Bi-2223 can be represented by the diphasic CuO-Cu_2O system (Fig. 5). Once reached in the EMF experiment, it is not possible to recover from the lower plateau and return to the Bi-2223 phase. The predecomposition of the Bi-2223 sample is known from prior work to involve formation of Bi-2212, Bi-2201, and alkaline earth cuprates.

In related work addressing the stability of Bi-2223, an Ag/Bi-2223 composite conductor was prepared from nearly phase-pure Pb-doped Bi-2223 obtained from Ames Laboratory. Specimens of this composite conductor were equilibrated in 0.01-21% O_2 at 815°C for 100 h. The results (Table 1) indicate that Bi-2223 in an Ag sheath is stable at 815°C for oxygen pressures between 2 and 13%. At 0.01% O_2, the sample decomposed to CaO and an amorphous phase; at 21% O_2, a multiphase (Bi-2212/Bi-2223/alkaline earth cuprate) transformation occurred. These results are in excellent agreement with our prior EMF measurements on the same Pb-doped Bi-2223 powder performed by oxygen titration (Poeppel et al., 1993).

Table 1. Effect of oxygen pressure on phase stability of Ag/Bi-2223 composite made with Pb-doped Bi-2223 (395-21). Specimens were heat treated at 815°C for 6000 min.

Oxygen Pressure (atm)	Dominant Layered Phase	Minor Layered Phase
1.0×10^{-4}	Amorphous	--
1.0×10^{-2}	Bi-2223	Bi-2201
2.0×10^{-2}	Bi-2223	--
7.5×10^{-2}	Bi-2223	--
9.8×10^{-2}	Bi-2223	--
13.0×10^{-2}	Bi-2223	Bi-2201
21.0×10^{-2}	Bi-2223 (53%) Bi-2212 (47%)	Bi-2201

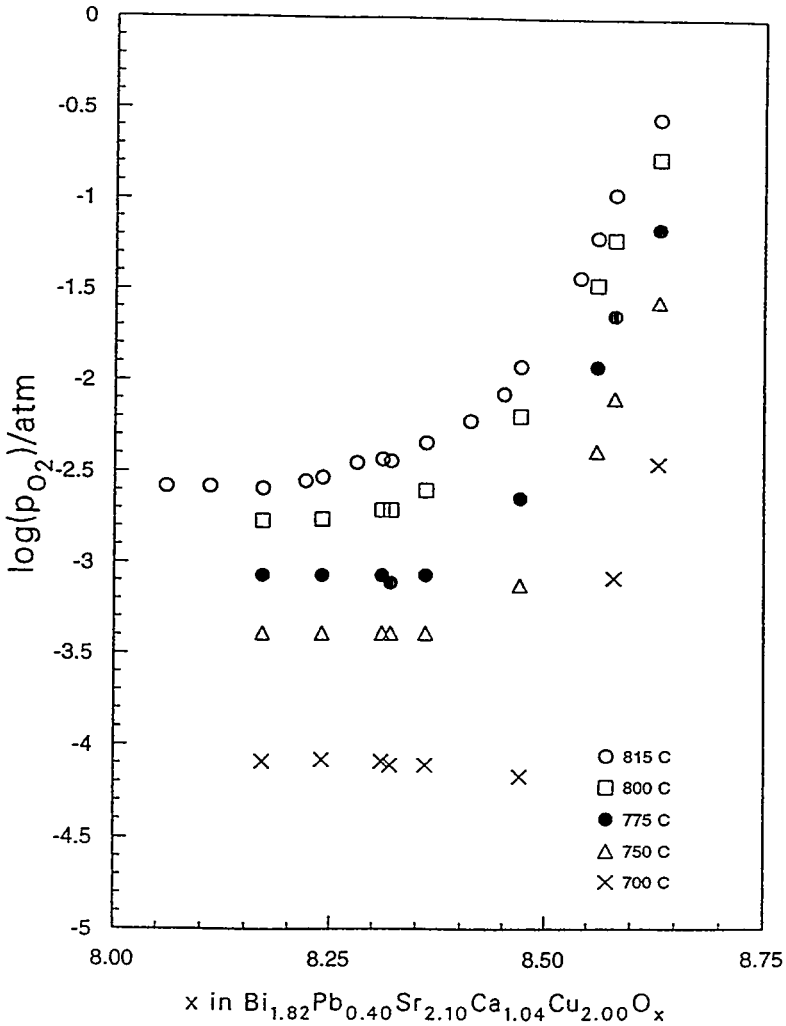

Fig. 3. EMF results by oxygen titration for Pb-doped Bi-2212 powder with overall stoichiometry of $Bi_{1.8}Pb_{0.4}Sr_{2.1}Ca_{1.0}Cu_{2.0}O_x$ and starting x = 8.62.

Analysis of carbon impurities and second phases

We have developed two spectroscopic methods for analyzing the chemical state of impurity and intermediate species in Bi-2223 precursor powders and Bi-2223/Ag composites. One technique involves use of infrared absorption spectroscopy to detect and quantify carbon-containing impurities. Carbon is believed to be deleterious to the production of high-performance Bi-2223/Ag composite conductors (Flükiger et al., 1992; Seibt et al., 1993). In exploring specimens of these powders by Fourier transform infrared (FTIR) spectroscopy with the KBr pellet method, we found that nearly all Bi-2223 and Bi-2212 powders contain detectable quantities of carbonate, even when the total carbon content is in the few hundred ppm range. Attempts to develop a quantification procedure based on standards of $CaCO_3$ and $SrCO_3$ indicated that a significant fraction of the carbon present in most samples is in the form of carbonate. There are, however, evidences of other forms of carbon in the infrared spectra and we are attempting to characterize these forms in a more definitive manner. Some powders excised from partially processed

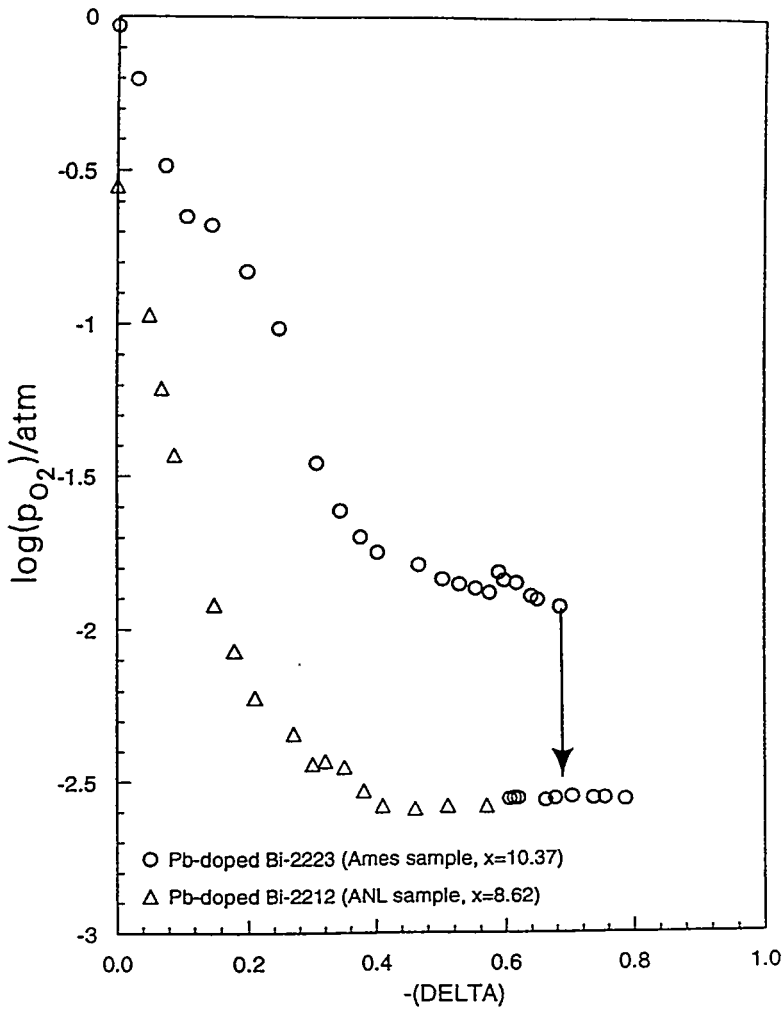

Fig. 4. Comparison of EMF results for Pb-doped Bi-2212 and Pb-doped Bi-2223 at 815°C. Log of O_2 pressure is plotted against change in oxygen content (due to electrochemical titration) relative to initial value of x in $(Bi,Pb)_2Sr_2Ca_{1/2}Cu_{2/3}O_{x+\partial}$ (where $\partial = 0$).

Bi-2223/Ag composites also show evidence of residual carbonate. We are seeking to determine whether this carbonate survived the processing procedure or was picked up during post-process handling.

Figure 6 presents FTIR spectra of three Bi-2223 precursor powders of differing total carbon levels as determined with a LECO Carbon Analyzer. The sloping background is caused by light-scattering effects associated with the opacity of the ceramic. The peak in the 1420 to 1470 cm^{-1} range is due mainly to the carbonate anion. The other peak in the extrapolated spectra at ≈1100 cm^{-1} is associated with carbonaceous matter. Application of our quantification procedure to these results indicates that a large fraction of the total carbon present in samples a and b can be accounted for by carbonate. We are still studying the origin of the ≈1100 cm^{-1} peak in the Fig. 6 insets, but have by spectral processing techniques been able to subtract this peak and its associated component at ≈1400 cm^{-1} in the inset for the low carbon sample (414-6-3) from the spectra for the high-carbon

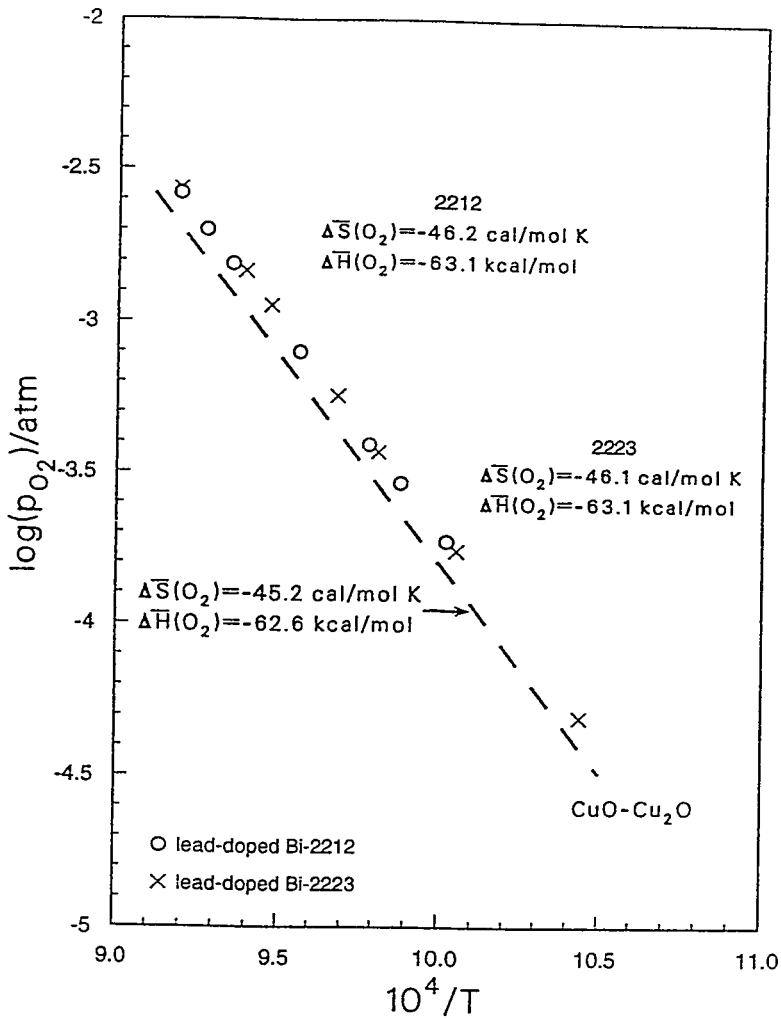

Fig. 5. Comparison of log pO2 versus reciprocal absolute temperature in lower plateau region for Pb–doped Bi–2212, Pb–doped Bi–2223, and the CuO–Cu2O system (dashed line).

samples (414–5–2 and 400–145–2). These subtractions (Fig. 7), leave spectra that contain the known carbonate frequencies at ≈1470 and ≈860 cm^{-1}, together with additional absorption features between 1400 and 1200 cm^{-1} that we have not fully elucidated.

The second spectroscopic method under study involves the use of imaging Raman microscopy to search for Ca_2PbO_4 and other Pb–containing species in Bi–2223 precursor powders and Bi–2223/Ag composites. Figure 8 shows micro–Raman spectra at selected locations on the surface of a pressed pellet composed primarily of Bi–2212 and an amount of Ca_2PbO_4 that is clearly measurable by X–ray diffraction. The top spectrum in Fig. 8 was taken with the laser spot focused on a single large Bi–2212 grain; it contains bands that are characteristic of Bi–2212. The middle spectrum was taken with the laser defocused slightly and positioned over a multiphase region of the pellet. The bottom spectrum was obtained from a KBr pellet containing a few weight percent Ca_2PbO_4. The strong band at ≈530 cm^{-1} is the signature peak for Ca_2PbO_4.

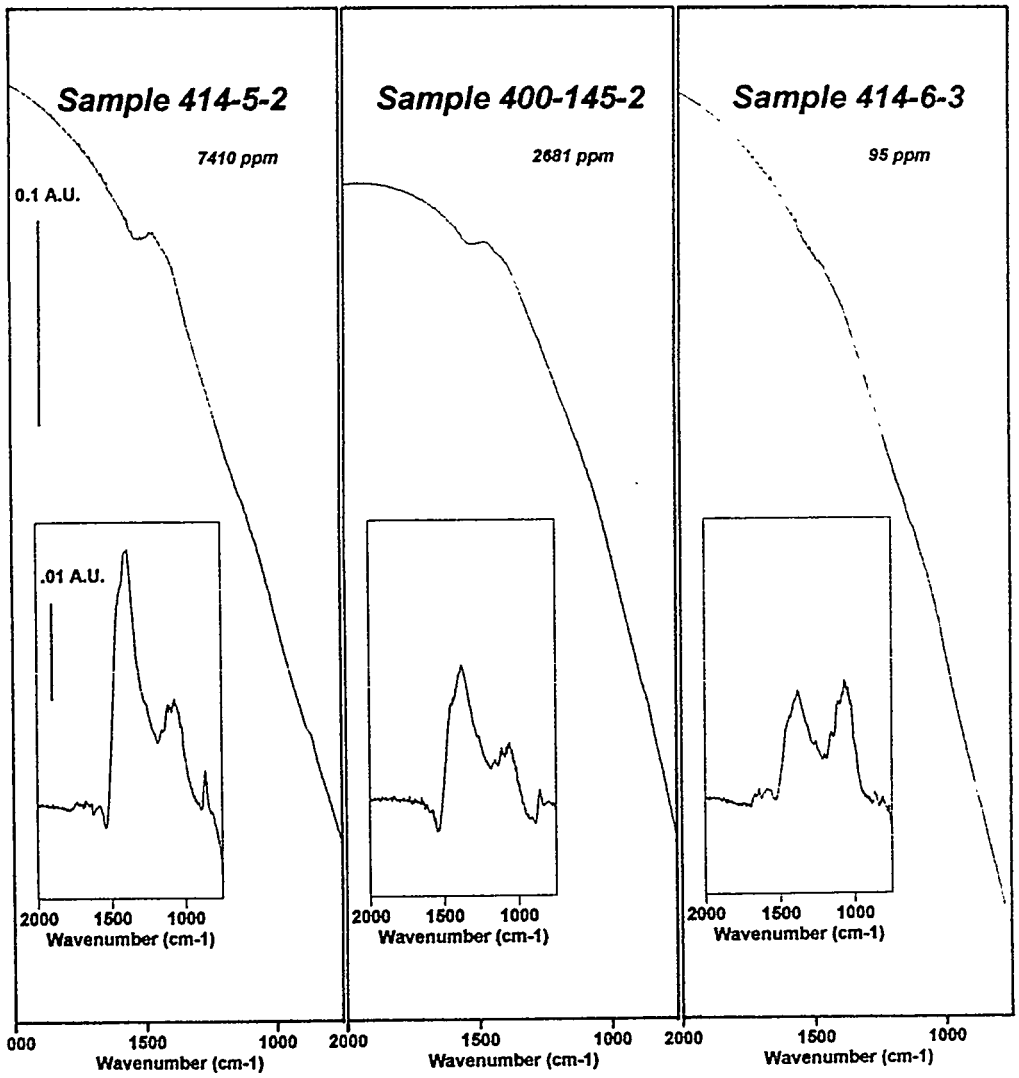

Fig. 6. FTIR spectra recorded for KBr pellets containing three Bi–2223 powders with different total carbon levels as indicated; inset spectra were obtained by constructing a smoothed background.

Figure 9 was obtained with the imaging Raman microscope in the spatial–resolution mode. The left image is of scattering at 700 cm^{-1} from the Bi–2212 pellet over a spot size ≈40 μm in diameter and is intended to serve as a background. The white spots in this image are produced by an unidentified fluorescing species that undoubtedly contributes the high background counts at 700 cm^{-1} in the upper and middle spectra in Fig. 8. The middle image in Fig. 9 is the scattering map at 525 cm^{-1} (the peak of the strong Ca_2PbO_4 band). The intense–scattering whiter areas indicate a dispersion of Ca_2PbO_4 around a Bi–2212 grain that lies in the bracketed area. These results illustrate the potential of imaging Raman microscopy for probing the location of specific Pb–containing phases.

2.1.2 Tape and Coil Development

Bi–based superconductors are more difficult to densify than conventional oxide materials, which generally can be sintered to greater than 90% of the theoretical density. In contrast, the density of Bi–based superconductors decreases upon heat treatment;

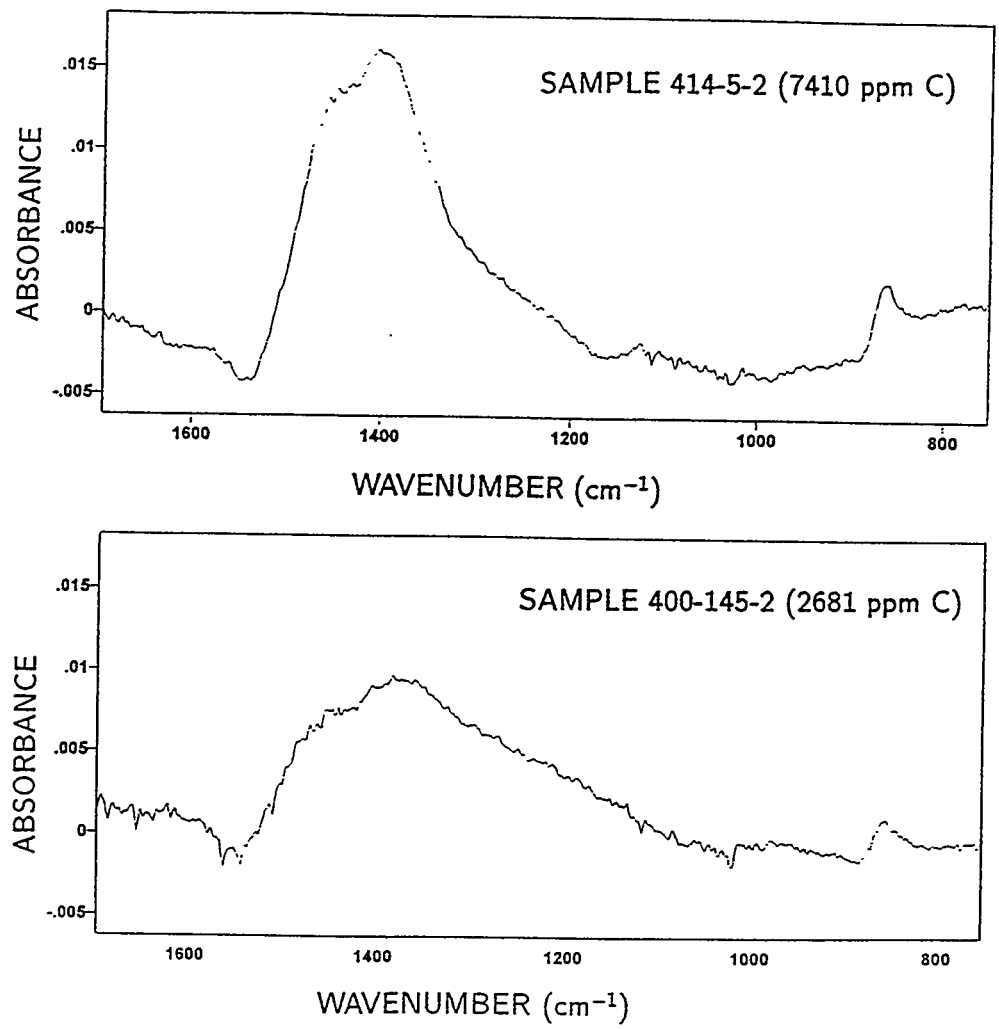

Fig. 7. Adjusted infrared spectra of samples 414–5–2 and 400–145–2 obtained by nulling out components of extrapolated spectrum for low–carbon sample 414–6–3.

therefore, heat treatment must be combined with mechanical deformation to increase density (Dawley et al., 1994).

Intermagnetics General Corporation tapes and coils

We continue to work closely with Intermagnetics General Corporation (IGC) on superconductor wire development. The goal of the partnership is to fabricate long lengths of commercially viable conductors capable of operating at temperatures and magnetic fields greater than those obtained by low–T_c superconductors.

By the PIT process and a series of thermomechanical treatments, consisting of uniaxial pressing and heat treatment, high J_c values have been obtained in short–length samples (Balachandran et al., 1994b). Because uniaxial pressing is not suitable for fabricating long lengths of conductors, a two–step rolling and heat–treatment procedure was developed. Compact and robust pancake coils were fabricated from these conductors (Haldar et al., 1994). The coils and test magnets made from the coils were characterized at 4.2, 27, 64, and 77 K in various applied fields.

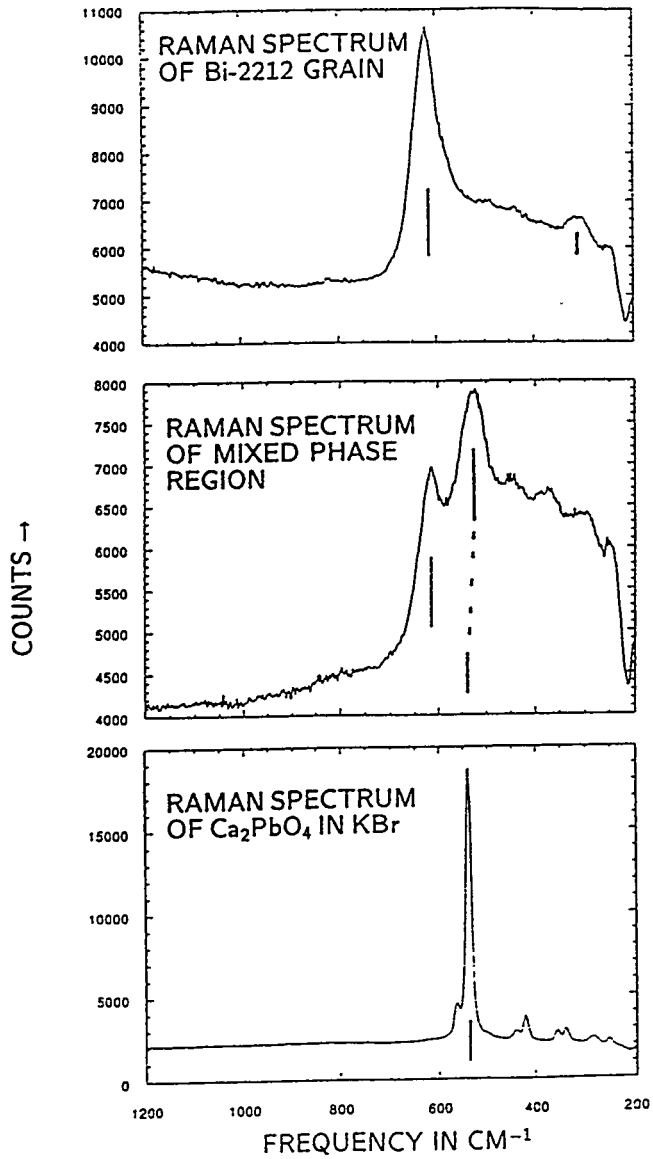

Fig. 8.
Raman microprobe spectra of (a) Bi-2212 grain in a pressed pellet containing mostly Bi-2212, with Ca_2PbO_4 as a minor second phase; (b) multiphase region of the same pellet; and (c) Ca_2PbO_4 dispersed in a KBr pellet.

Ag-clad Bi-2223 conductors were fabricated by packing partially reacted precursor powder into high-purity Ag tubes, drawing the tubes through a series of dies, and rolling to a final thickness of ≈0.1 mm. Short lengths of the Ag-clad Bi-2223 tapes exhibited J_c values >4 x 10^4 A/cm^2 at 77 K. Success with short tapes encouraged us to develop techniques for fabricating long lengths of mono- and multifilament conductors. Conductors of up to several hundred meters in length have been fabricated.

The long-length conductors are fabricated by packing powders into large-diameter Ag tubes (Fig. 10). At 77 K, J_c values of ≈1.5 x 10^4 A/cm^2 have been achieved in 70-m-long conductors. Pancake-shaped coils were fabricated by the wind-and-react approach; test magnets were then fabricated by stacking the pancake coils and connecting them in series. A test magnet containing ≈480 m of monofilament conductor generated a record-high magnetic field of 2.6 T at 4.2 K and zero applied field (Balachandran et al., 1993a and 1994a). Recently, another magnet was fabricated with 16 pancake coils, each containing three 16 m lengths of Bi-2223 conductor (Fig. 11). Total length of the conductor in the magnet was ≈768 m. Figure 12 shows the characteristics of this magnet at 4.2 K and 27 K,

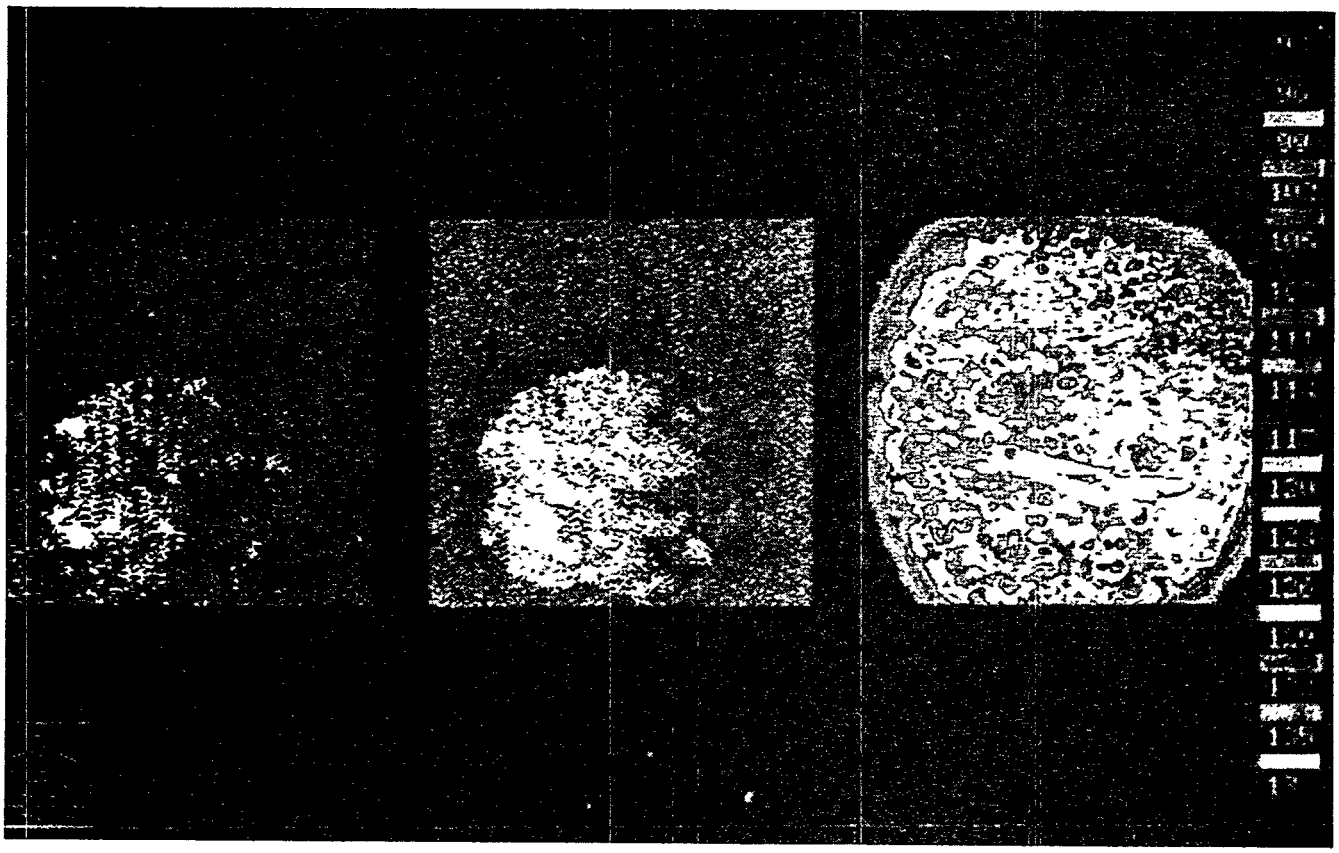

Fig. 9. Imaging Raman microscope (IRM) study of a Bi-2212 pressed pellet containing Ca_2PbO_4 as a second phase; left image was obtained for an IRM scan at 700 cm^{-1} (background), middle image was obtained for a scan at 530 cm^{-1}, and right image is a white-light view that encompasses the region covered in the IRM images.

in a background field of ≈20 T at 4.2 K. The magnet generated a field of 1 T at 4.2 K in a 20 T background field. This result is very encouraging because it indicates the possibility of using high-T_c magnets as inserts in low-T_c magnets to form hybrids for generating very high fields. Figure 13 shows the critical current (I_c) as a function of length of a multifilament conductor containing 37 filaments. Total length of the conductor is 230 m. The plot shows that consistent I_c values have been obtained in long multifilament conductors. These results are an indication of the recent improvement in the development of mono- and multifilament high-T_c conductors.

Reaction-induced texture

ANL and the American Superconductor Corporation (ASC) have been engaged in a joint research project to elucidate the mechanism of texture evolution in Ag/Bi-2223 composite conductors. Texture of the current-carrying layered phase is essential to achievement of high-performance levels in high-T_c composite superconductors. Accordingly, mechanisms that give rise to texture during PIT processing of Ag/Bi-2223 composites must be understood in the context of processing these technologically interesting composites. Results of the joint ANL-ASC study, based on X-ray diffraction measurements and computerized analysis of SEM images, demonstrate that significant texturing of Bi-2223 occurs during heat treatment of the Ag-sheathed composites. Evidence for this reaction-induced texture (RIT) in a one-powder composite obtained from ASC is shown in Fig. 14.

Fig. 10.
Filling Ag tubes with precursor powder.

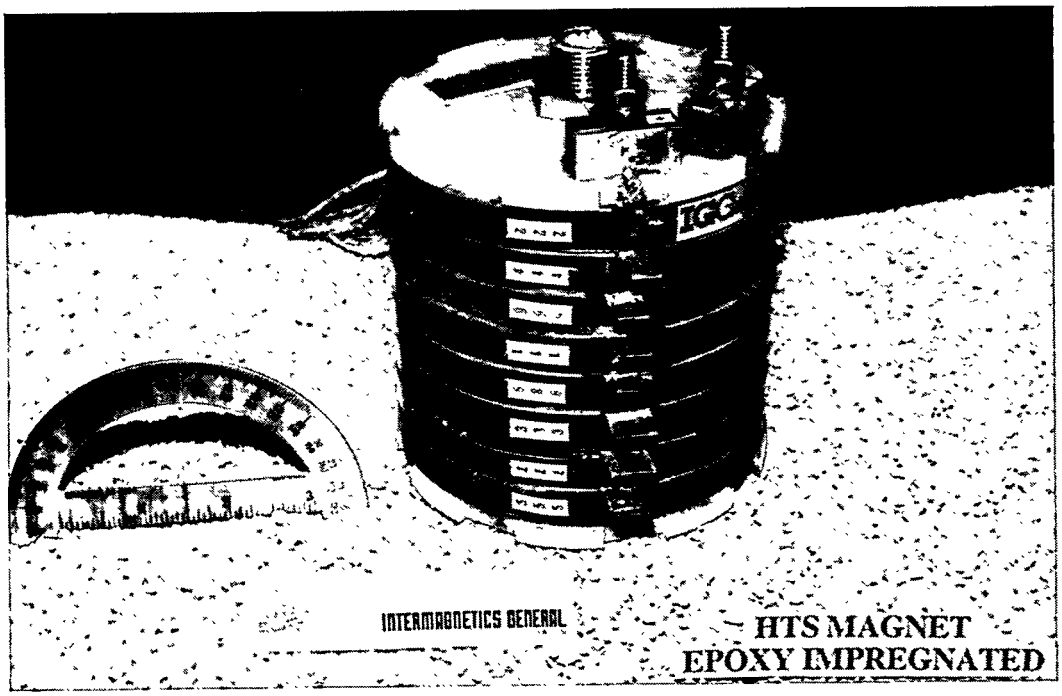

Fig. 11. High-T_c test magnet fabricated from 16 pancake coils.

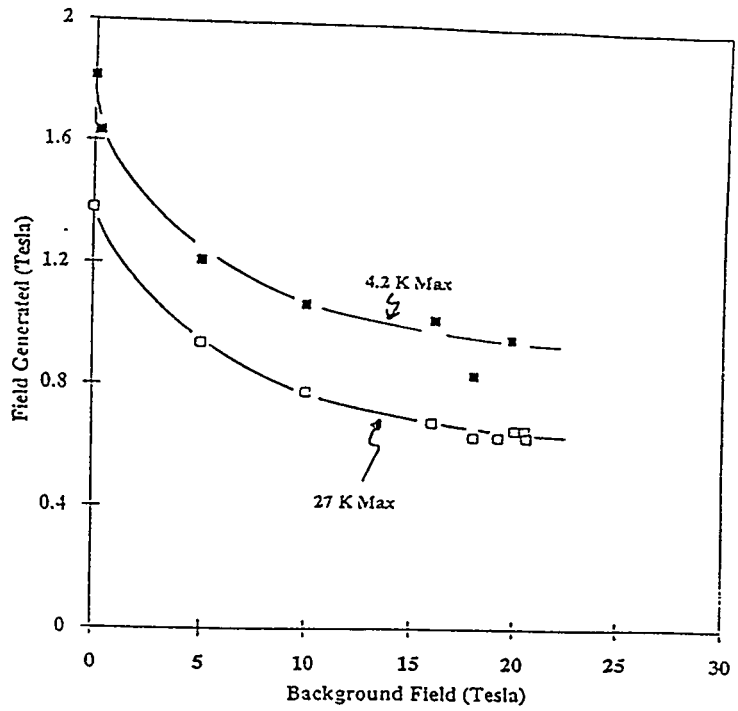

Fig. 12. Field generated by high–T_c magnet vs. background field at 4.2 and 27 K.

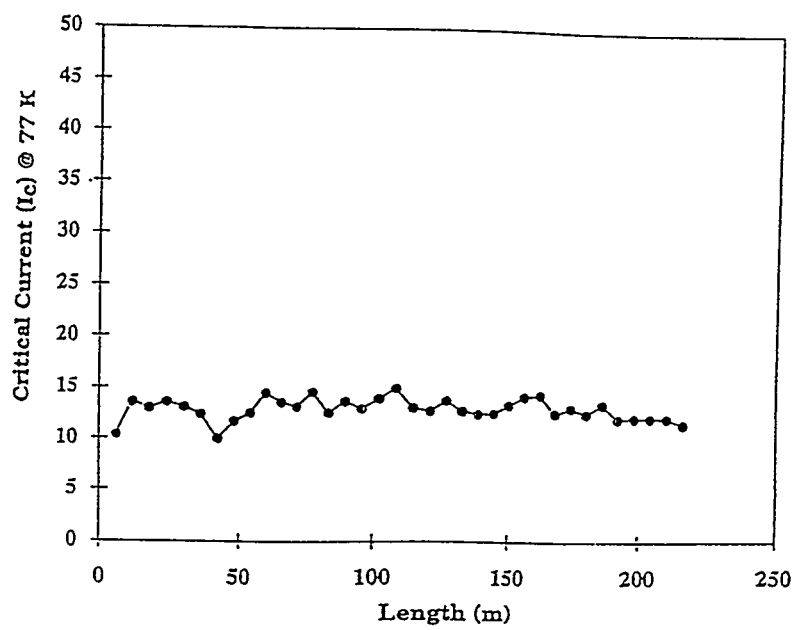

Fig. 13. I_c at 77 K of conductor containing 37 filaments.

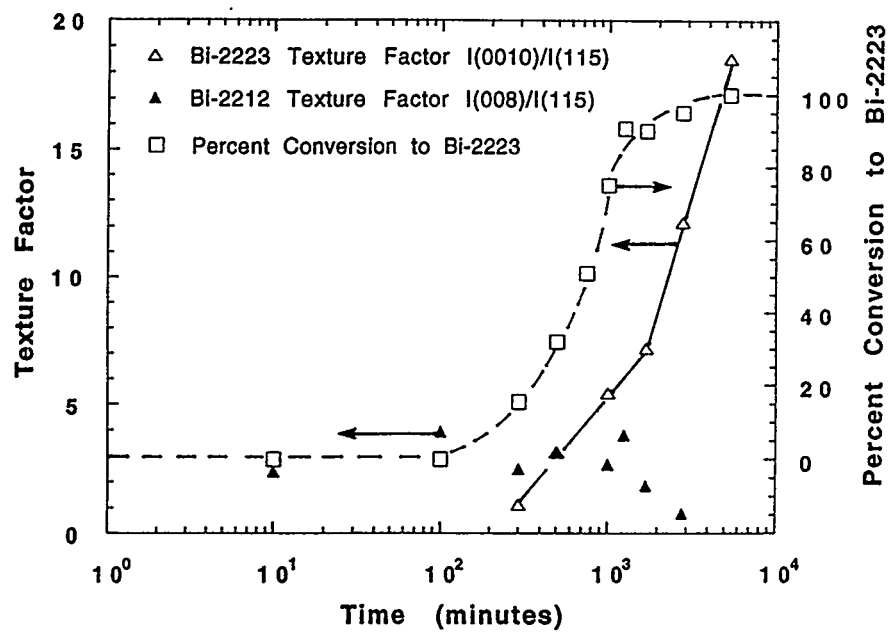

Fig. 14. Texture factor for Bi-2223 and Bi-2212, and ratio of Bi-2223 to Bi-2212 + Bi-2223, as a function of time at 825°C in 7.5% O_2 for one-powder composite.

The temporal dependence of the Bi-2223 to Bi-2212 + Bi-2223 ratio and the preferred orientation of Bi-2212 and Bi-2223 during heat treatment at 825°C in 7.5% O_2/balance N_2 are provided in this figure.

The induction period and sigmoidal transformation kinetics reflected by the conversion curve have been discussed previously by Luo et al. (1993). The ratio of the intensity of the [008] or [0010] reflection to that of the corresponding polycrystalline [115] reflection provides a measure of the c-axis texture of the Bi-2212 or Bi-2223 grains, respectively. The results shown in Fig. 14 demonstrate that the texture of Bi-2223 increases dramatically during heat treatment. Specifically, the texture factor for Bi-2223 increases by a factor of 20 from initial formation at ≈300 min to complete transformation at ≈5400 min. For Bi-2223, the time rate of change of the texture is similar to, but lags behind, that of the volume fraction. In contrast, the texture factor for Bi-2212 is initially about 2 and does not change significantly over the course of the heat treatment.

The development of RIT in a two-powder composite is shown in Fig. 15. The kinetics of formation and preferred orientation of the Bi-2223 for the two-powder composite are similar to those for the one-powder composite. Even though full conversion to Bi-2223 was achieved for both powder types, the maximum texture factor measured for the two-powder composite (≈32) is 1.5 times that measured for the one-powder composite (≈20).

Evidence for RIT in the one-powder composite obtained through computerized image analysis is given in Fig. 16. The scatter diagrams in this figure show the orientation of superconductor grains across the thickness of the tape for the 100 and 5400 min samples in Fig. 14. After 100 minutes of heat treatment (Fig. 16a), where almost all of the layered phase is Bi-2212, the grains show no preferred orientation relative to the surface of the composite. However, after 5400 minutes of heat treatment (Fig. 16b), where almost all of the layered phase is Bi-2223, the grains exhibit a marked preferred orientation with

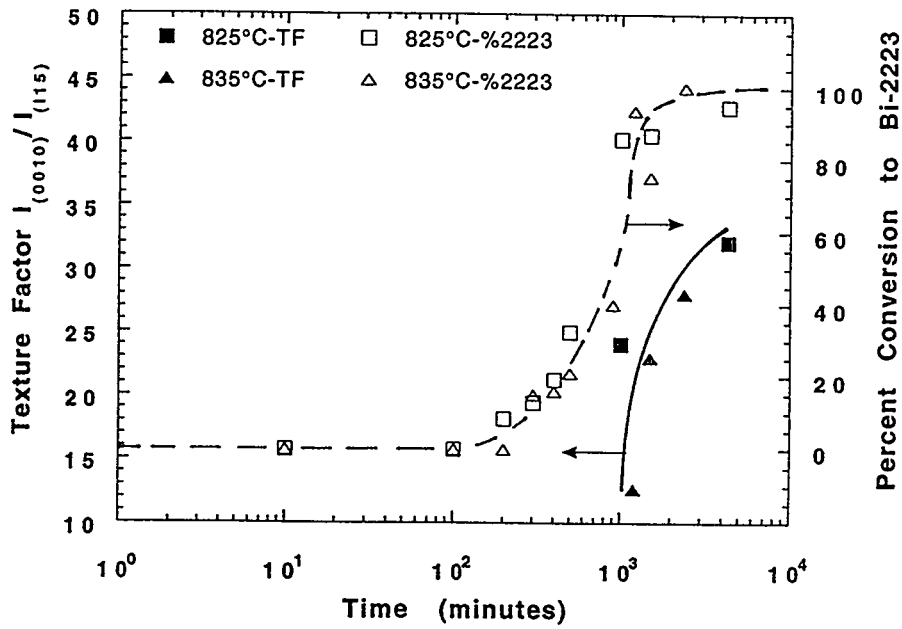

Fig. 15. Texture factor for Bi-2223, and the ratio of Bi-2223 to Bi-2212 + Bi-2223, as a function of time at 825 and 835°C in 7.5% O_2 for two-powder composite.

respect to the surface of the composite. Moreover, there is evidence in Fig. 16b that texture development is more pronounced at the interface between the ceramic core and the Ag sheath, suggesting that the Ag may locally promote RIT.

The methods to characterize texture demonstrate that the degree of preferred orientation of Bi-2223 increases dramatically during heat treatment of the composite. Because Bi-2223 is also forming during heat treatment, there are at least two possible texturing mechanisms. One is the preferential nucleation of oriented Bi-2223 grains, but we have previously found evidence that Bi-2223 forms via an intercalation mechanism (Luo et al., 1993). Intercalation should cause the Bi-2223 to inherit the crystallographic orientation of the parent Bi-2212 phase. Because the texture factor for Bi-2212 has an initial value of ≈2, the maximum amount of Bi-2223 texture that can be attributed to intercalation is at least one order of magnitude lower than that observed (≈20). In addition, given the time delay between the formation of Bi-2223 and the development of texture of the Bi-2223 grain, significant heterogeneous nucleation of Bi-2223 with preferred orientation can be ruled out.

Preferential growth of oriented Bi-2223 grains is the other possible texturing mechanism. Although Bi-2223 grains have been observed to penetrate into the Ag sheath at oblique angles (Feng et al., 1993), such grains are considerably less common than those that have c-axes perpendicular to the interface between the sheath and the filament. Microstructural evidence suggests that resistance to grain growth is lowest in the direction parallel to this interface. Because the growth of the Bi-2223 grains is constrained by the Ag, Ostwald ripening of Bi-2223 grains that occurs naturally at elevated temperatures will necessarily result in a textured microstructure. This growth in constrained volume may be driven by minimization of the interfacial free energy, subject to the unique geometric boundary conditions present in Ag/Bi-2223 composites. The constrained growth mechanism is consistent with the plot in Fig. 16b, which shows that the texture decreases as distance increases from the sheath.

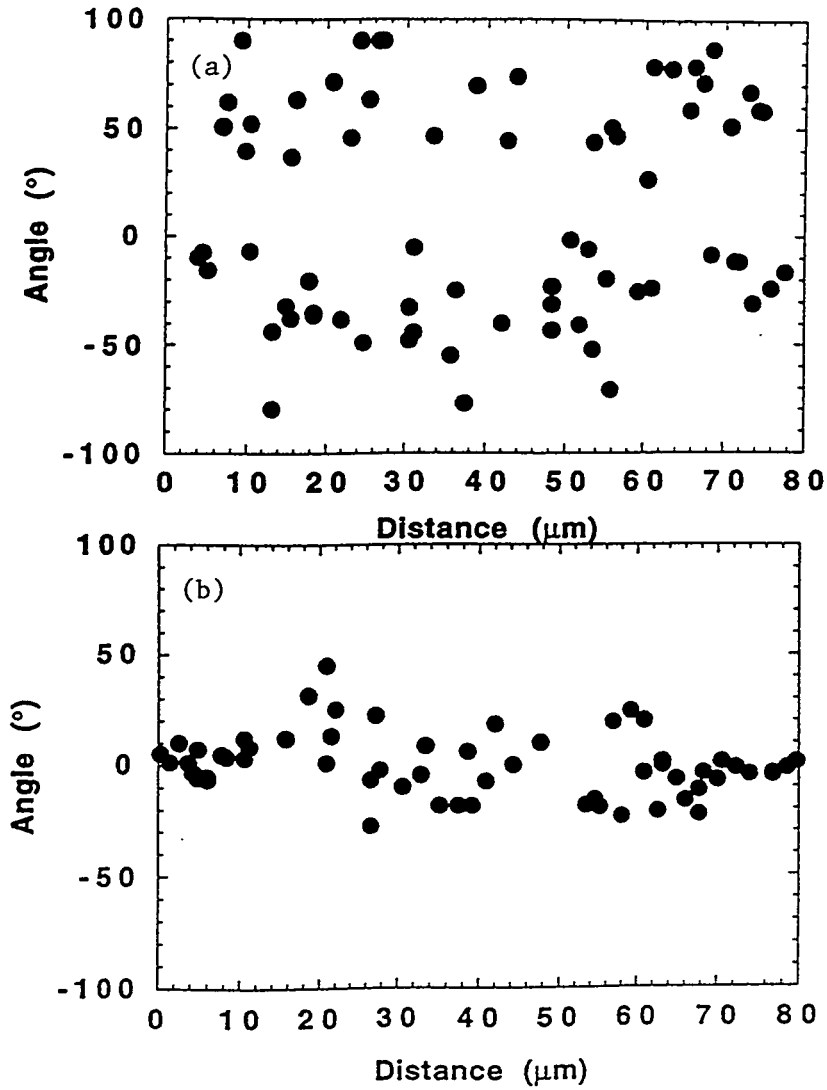

Fig. 16. Computer-assisted image analysis of grain orientation across thickness of tape for one-powder composite heat treated at 825°C in 7.5% O_2 for (a) 100 min and (b) 5400 min.

Additional experiments have been performed to more thoroughly investigate constrained growth aspects of the RIT mechanism. In one such experiment, a specimen of a two-powder Bi-2223/Ag monofilament was warmed to 100°C in the as-rolled condition (to anneal the Ag), warped with a pair of pliers (by squeezing along the transverse axis) to create open space inside the sheath, then heat treated at 820°C in 7.5% O_2 for 150 h. A specimen of the same two-powder composite in the as-rolled state (not warped) was heat treated along with the warped specimen for purposes of comparison. Insets a and b in Fig. 17 show the transverse cross sections of the warped and as-rolled specimens, respectively, after heat treatment. The consequences of warping, in terms of producing open space to relieve the constraining boundaries of the sheath, are clearly seen in these images. The grains of layered phase material in the warped sample (nearly all Bi-2223 from X-ray diffraction analysis on a peeled section of the specimen) are gathered in clumps. While there seems to be some evidence of a preferential grain direction in each clump (insets c and d in Fig. 17), these preferential directions bear no discernible relationship to the nearby Ag sheath surfaces, confirming our previous hypothesis that the mere presence of

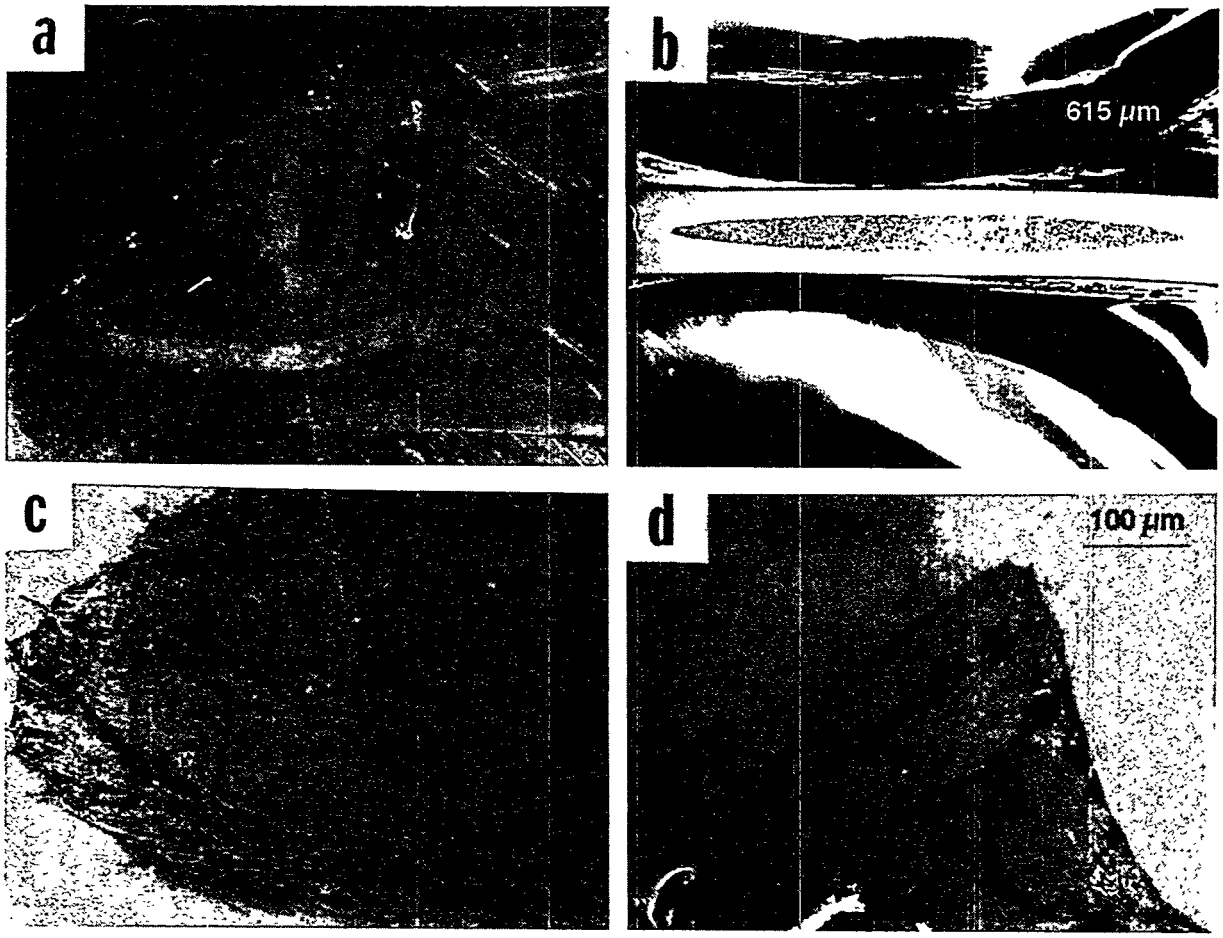

Fig. 17. Scanning electron microscope images of (a) warped specimen and (b) as-rolled specimen of two-powder Bi-2223/Ag composite conductor after heat treatment at 820°C in 7.5% O_2 for 150 h; insets (c) and (d) are higher-magnification images of selected regions of warped specimen.

an Ag surface in the vicinity of the powder reaction zone is not sufficient to induce texture throughout the whole core. It seems to be more likely that individual grains, which form early in the conversion process, may be acting as templates for neighboring grains leading to the type of grain colony development often seen in micrographs of fully processed Bi-2223/Ag composites. The presumption that grain growth in a constrained environment is responsible for RIT appears to be strongly supported by the results in Fig. 17. The influence of the Ag sheath on texture development does not reach much beyond the first 10 μm of a monofilament core even after hundreds of hours of heat treatment.

American Superconductor Corporation tapes

In additional collaborations with ASC, we have used transmission electron microscopy (TEM) and EDX to identify and quantify regions of amorphous material in Bi-2223/Ag composite conductors that had received <300 min of heat treatments in 7.5% O_2. ASC prepared an oxide powder mix with the metal atom stoichiometry of the amorphous material. We performed differential thermal analysis (DTA) on this powder, nominally

$Bi_{2.4}Pb_{1.8}Sr_{1.4}Ca_{1.2}Cu_{2.2}O_x$. A single endotherm is observed at ≈680°C (Fig. 18). The subject phase was clearly low melting and not easily reacted away on the time scale of the DTA cycles. Decomposition was more prevalent in 21% O_2 than in 7.5% O_2.

Work currently in progress is focused on reaction kinetics, phase evolution, and microstructure development in oxide–powder (OP) and metal–precursor (MP) multifilaments fabricated by ASC. Figure 19 presents results of reaction kinetics measurements on 361 filament OP and MP Bi–2223/Ag composites. The plot in Fig. 19a shows the dependence of percent conversion to Bi–2223 on temperature in 7.5% O_2 after 1500 min of heat treatment. The dashed curve is a representation of typical behavior under comparable conditions for two–powder Bi–2223/Ag monofilamentary composites. The reaction in the 361 OP composite leading to stable Bi–2223 takes place over a considerably narrower range of temperature and much more sluggishly than that observed for the 361 MP composite. Figure 19b contains a plot of % conversion to Bi–2223 verses time at 810°C in 7.5% O_2, together with a dashed curve that represents typical behavior of OP monofilaments under similar conditions.

Process–optimization studies

Our fabrication process starts from $Bi_{1.8}Pb_{0.4}Sr_2Ca_2Cu_3O_{10}$ powder that is composed of a known phase assemblage. In this case, the two–powder process is employed to take advantage of reaction sintering to achieve aligned microstructures. During the initial stages of heat treatment, Bi–2223 is formed as large grains with high aspect ratios. Previous work (Poeppel et al., 1993) revealed that most of the conversion from 2212 to 2223 occurs within 1000 min of heat treatment, and suggests that the reaction kinetics are governed by a liquid phase in the early stages of the process. However, to achieve high J_c values, significantly longer heat–treatment times are required.

A thermomechanical schedule was developed from J_c data taken on uniaxially pressed Ag–clad Bi–2223 tapes. These tapes were fabricated by our two–powder process and given a series of anneals at 815°C in flowing 8% O_2/92% N_2. Ten separate pressing sequences were used to determine empirically the optimal schedule. An example sequence is shown

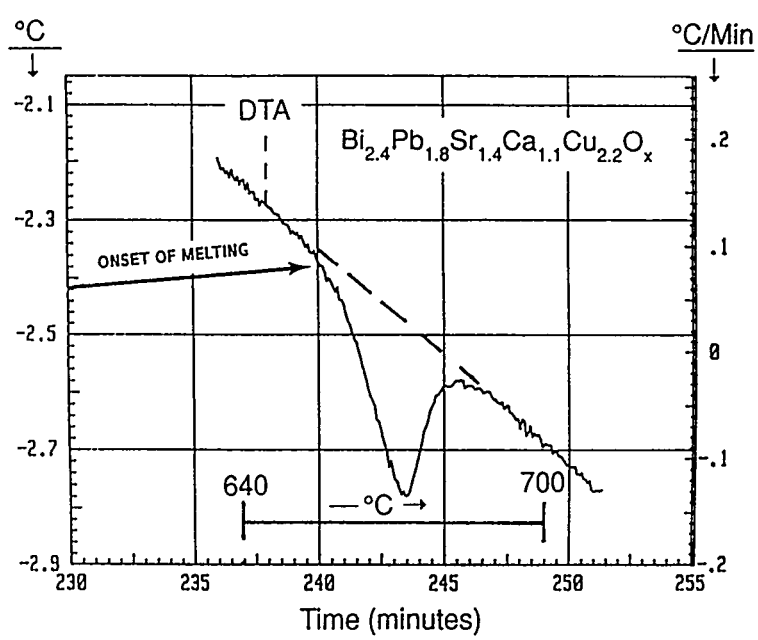

Fig. 18.
Differential thermal analysis curve for "liquid phase" composition detected in one–powder Bi–2223/Ag composite.

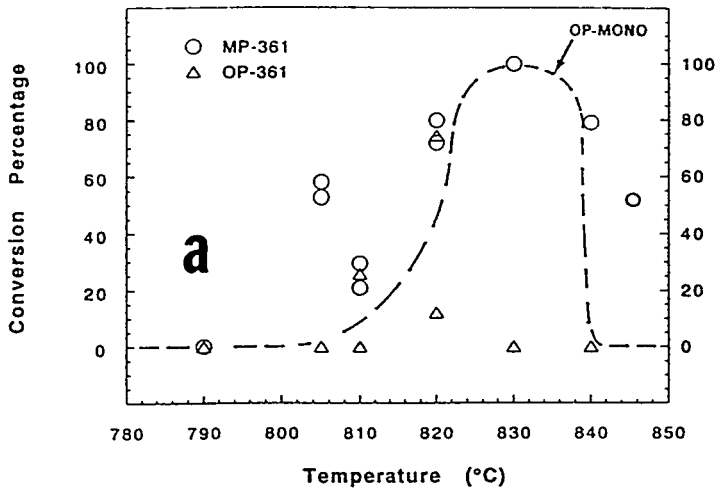

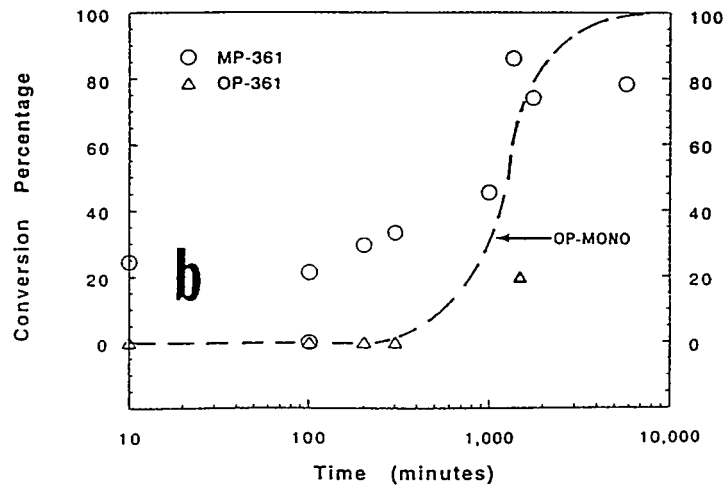

Fig. 19.
(a) Conversion vs. temperature plot for MP-361 and OP-361 Bi-2223/Ag multifilaments heat treated in 7.5% O_2 for 1500 min. (b) conversion vs. time plot for MP-361 and OP-361 Bi-2223/Ag multifilaments heat treated at 810°C in 7.5% O_2.

in Fig. 20. The individual data points define the time at which the thermal treatment was interrupted and the specimens were pressed. The results for 10 samples are shown in Fig. 21. In this figure, which is the slope of Fig. 20, the largest increase in I_c is for pressing between 40 and 140 h of heat treatment.

Other key parameters in PIT processing of Ag-sheathed Bi-2223 tapes, such as tape thickness, initial packing density, sintering temperature, and cooling rate, were also studied (Joo et al., 1993). The starting Bi-2223 powder was the standard two-powder mixture. For some tapes, a composite was prepared by adding 15 wt.% particulate Ag (Singh et al., 1993a and 1993b).

Tapes were rolled to various thicknesses, and the variation in J_c was studied. J_c increased with decreasing tape thickness to 120 μm. Further decreases in thickness resulted in an irregular Ag/core interface, which caused a decrease in J_c (see Fig. 22).

Tapes with different initial packing densities (45%, 35%, 28%, and 23%) were processed, and the effect of packing density on the Ag/core interface was examined. It was found that tapes with 45% initial density could sustain a regular Ag/core to a thickness as low as 90 μm. In contrast, for tapes with 23% initial density, sausaging (formation of an

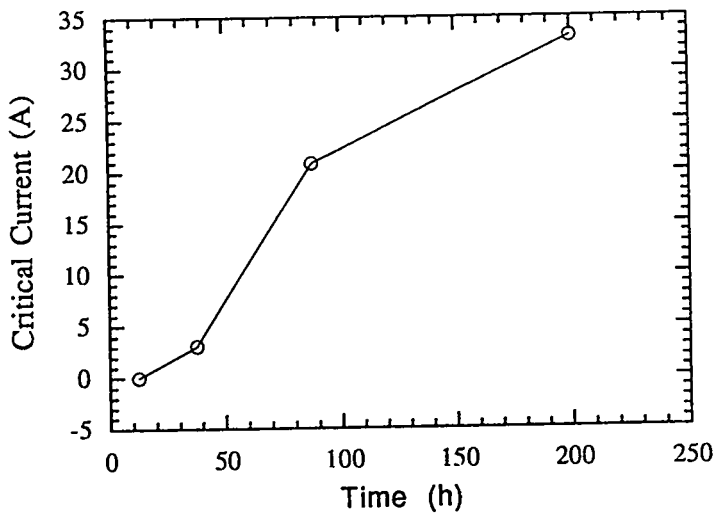

Fig. 20.
Bi-2223 tapes were fabricated from our two-powder process and given a series of annealings at 815°C in 8% O_2/92% N_2.

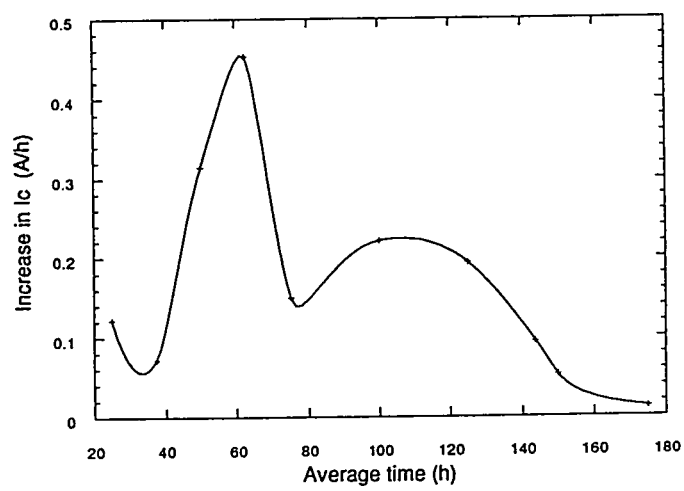

Fig. 21.
Improvement of I_c by heat treatment of PIT tapes with intermittent pressing.

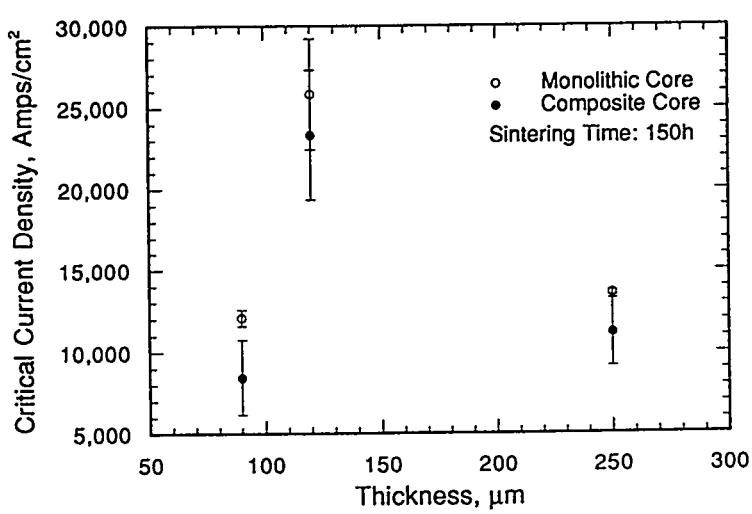

Fig. 22.
Dependence of J_c on tape thickness.

irregular interface) began when the tapes reached a thickness of ≈200 μm. This result suggests that higher initial packing density has a beneficial effect on the Ag/core interface and that higher J_c values may obtain.

Variation of J_c with sintering temperature was studied for both monolithic and composite Bi-2223 cores at 810°C–830°C in 8% O_2/92% N_2 (Fig. 23). Sintering at temperatures ≤ 810°C was inadequate for 2223 phase conversion, and sintering at ≥830°C led to dissociation of the 2223 phase and growth of second phases; both resulted in decreased J_c. The best J_c values were obtained between 815°C and 825°C.

The variation of J_c in this temperature range is related to its dependence on core density and distribution of second phases. With increase in sintering temperature, density increases are accompanied by increased dissociation of Bi-2223 to Bi-2212 and nonsuperconducting phases. These two competing phenomena control the J_c.

Preliminary studies on the effect of cooling rate and sintering temperature (815–825°C) on superconducting properties of Bi-2223 tapes indicate that there is a strong influence of cooling rate on J_c tapes sintered at 825°C. Faster cooling rates degraded J_c. On the other hand, the effect of cooling rate was less pronounced when the tapes were sintered at 815°C. This observation suggests that cooling rate becomes more important for partial-melt heat treatments. Cooling rate will influence the oxygen content in the cores, in turn affecting microstructure and superconducting properties.

Wire-in-tube processing

A method being tested as a means for improving grain alignment is the Ag wire-in-tube method. Small (127–508 μm diameter) Ag wires are added to the superconductor core to provide additional interface area between the Ag and superconductor. This may be desirable, because many investigators feel that the thin (≈5 μm), well-aligned layer of Bi-2223 that forms at the interface with the Ag sheath may carry most of the current, if not all. The well-known improvement in J_c that results from a decrease in core thickness is thought to occur because the interface layer accounts for a greater portion of the core in thinner tapes. The wire-in-tube method differs from the addition of particulate Ag, because the wires extend along the entire length of tape and provide a surface on which the Bi-2223 grains can align themselves. By contrast, when the Ag is not continuous, it can possibly act much like any other second phase, disrupting grain alignment and blocking the current path.

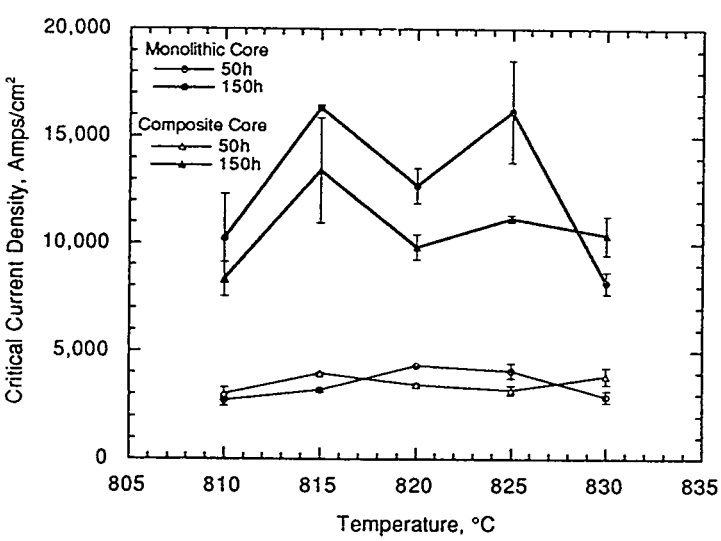

Fig. 23.
Variation of J_c with sintering temperature.

Although work in this area is in early stages, examination of a sample with four wires in the core shows that the wires are continuous and parallel to the sheath (Fig. 24a), and that after heat treatment a dense layer forms at all Ag/superconductor interfaces (Fig. 24b). The effect of the Ag wires on J_c is not conclusive at this point. In the future, we will continue testing the wire-in-tube method. The fraction of well-aligned interfacial material will be controlled by varying the number and size of wires in the core to test the importance of the interfacial region. If the interfacial region truly plays the crucial role that many investigators suspect, the wire-in-tube technique should improve the performance of PIT tapes.

Process for continuous tape production

The objective of work under an agreement with Andrew Corporation is to develop a continuous process for manufacturing clad high-T_c wire. Andrew has the expertise in manufacture of coaxial cable; ANL has the capabilities needed to support wire fabrication by providing superconductor powder, wire heat treatment, and conductor characterization.

The initial task was to synthesize a flowable superconducting powder for continuous feeding. Flowable powders are typically composed of spheres greater than 50 μm in diameter. Bi-2223 powder has a platelike morphology and an average particle size of ≈5 μm. Consequently, the powder tends to flow poorly. Organic binders can be used to set individual particles into agglomerates (Fig. 25).

Powder flow characteristics were examined by measuring powder flow rate into an Ag tube that was seam-welded by Andrew Corporation. Superconductor powder was uniformly loaded into a trough and the assembly was vibrated at 60 Hz. A significant increase in powder flow and reduced clogging of the funnel were achieved with use of agglomerated particles (Table 2). The funnel clogged several times with the as-synthesized powder. Future work will focus on incorporating a flowable powder into the production line at Andrew.

Hot rolling of tapes

Hot rolling continues to be examined as a means of fabricating Bi-based PIT tapes. To improve the effectiveness of hot rolling, efforts were undertaken to minimize sheath/core irregularities. Two approaches were to minimize the melting temperature of the Bi-2212 core and to improve the stiffness of the metallic sheath (Guo et al., 1994a; Schwartz et al., 1994).

Melting temperatures were decreased by addition of Li (Goretta et al., 1993, Guo et al., 1994b). Relatively good microstructures were obtained once the rolls were heated to ≈400°C, but the Li additions have tended to promote formation of second phases. Phase impurities are generally observed for Li-containing superconductors. No further work is planned on Li-containing Bi-2212 conductors until more highly phase-pure materials can be synthesized reproducibly.

Stiffer sheaths included Ag/7% Cu and Ti and its alloys. Preliminary work has shown that Cu diffusion into the Bi-2212 during heat treatment is significant, but that use of a Cu-deficient superconductor composition can minimize any deleterious effects. Ti diffusion was much less of a problem. In brief, smoother interfaces were obtained with all of the alloys than with a pure Ag sheath. To date, however, there has been no improvement in transport J_c compared with our convention PIT processing (Wu et al., 1994). Heat treatments for the tapes with alloys sheaths must differ from those for Ag-sheathed tapes. Optimal schedules have yet to be found, and additional heat-treatment studies are planned.

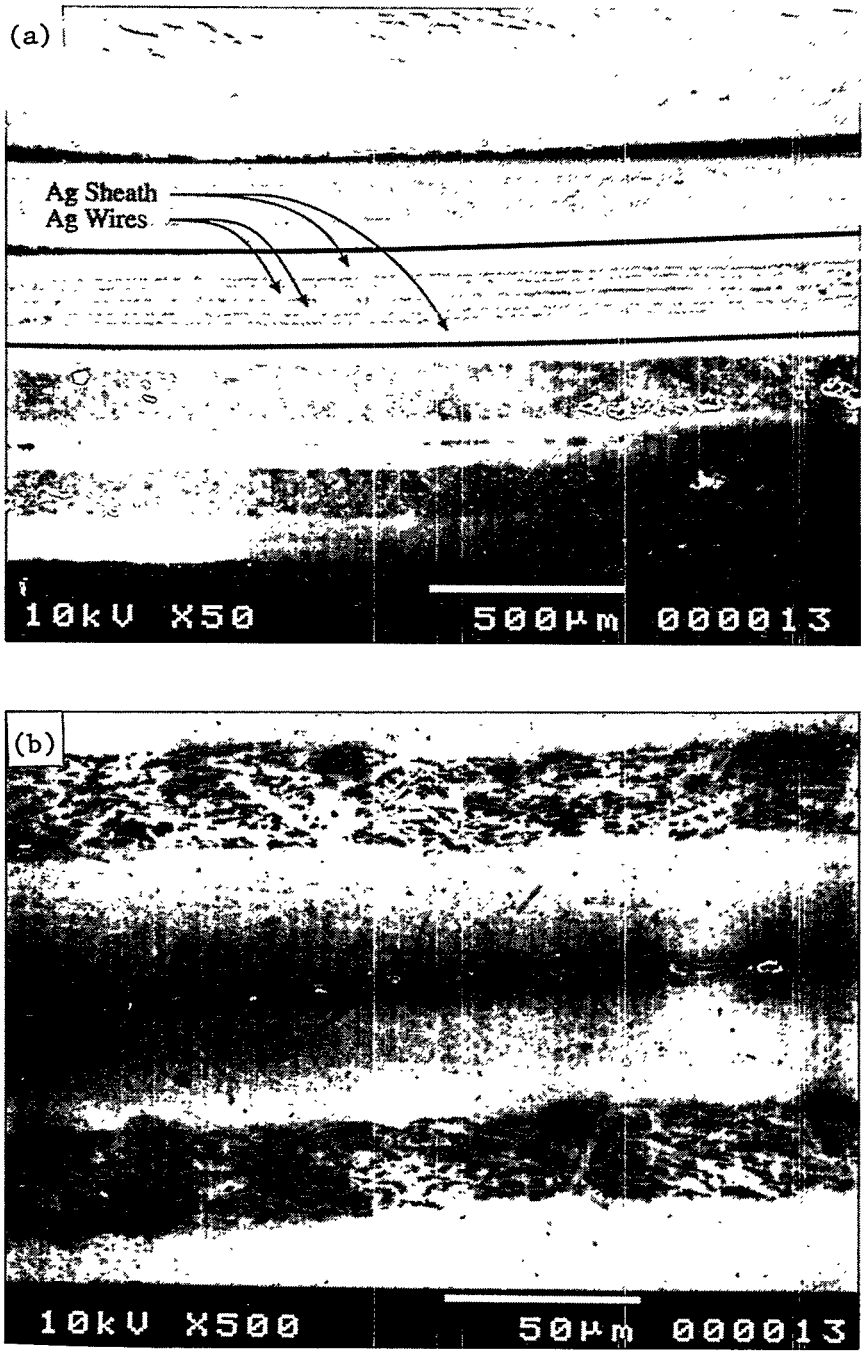

Fig. 24. Longitudinal view showing two of four wires in core of sample made by the Ag wire-in-tube method.

Bars and rods

Because of its T_c of 110 K, Bi-2223 may be superior to YBCO for moderate-J_c bulk applications at 77 K. Monolithic rods 1 m long have been made by cold isostatic pressing (CIPing). J_c values in zero applied field have reached 2 x 10^3 A/cm^2. Hot deformation in air at 845°C has produced bars with J_c values to 8 x 10^3 A/cm^2 and critical currents to >750 A (Chen et al., 1993a). The hot-deformation process has been scaled up to produce lengths of up to 20 cm.

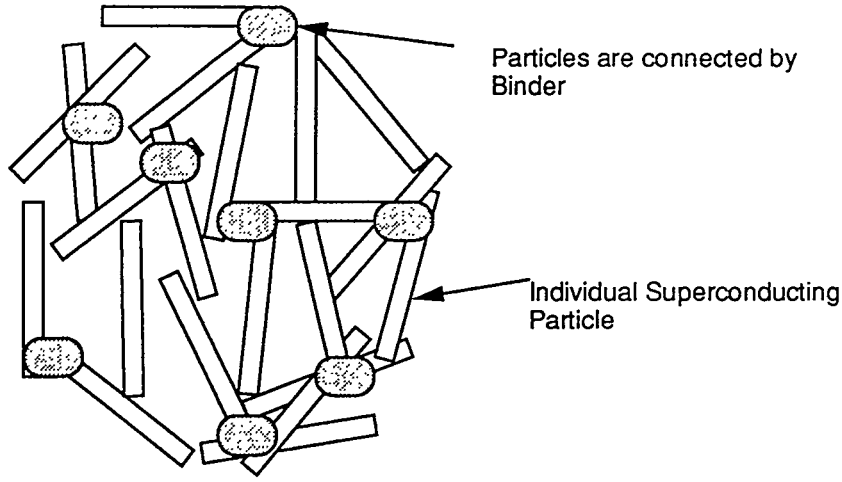

Fig. 25. Schematic diagram of flowing powder.

Table 2. Summary of powder flow characteristics

Powder	Flow (g/min)	Packing (g/cm^3)	% Theoretical Packing Density
As Synthesized	50	1.1	18
With Binder	200		
Heat Treated	200	2.7	42

Shrinkage data for bulk Bi-2223 bars reveal that there are two distinct regions of interest during processing (Fig. 26). Density increased during the initial stages of heat treatment and then decreased after approximately 17 h. These data suggest that liquid-phase sintering occurs during the initial stages of heat treatment and subsequent grain growth causes a decrease in density. Additional heat treatment and CIPing steps proved to be necessary to increase density and enhance J_c.

Thermomechanical processing for bulk Bi-2223 bars was based on a pressing-sequence study and dilatometer data. Figure 27 displays the density progression for a thermomechanical sequence. CIPing is not necessary during the early stages of sintering (<25 h) because densification naturally occurs during heat treatment. The first heat treatment process was carried out in air at 865°C for 50 h. Consistent with dilatometer data, density decreased with time. Additional density increase could, however, only be achieved by CIPing. A 30% increase in the final density was achieved by the thermomechanical process.

J_c improved for the three CIP/heat treatment cycles; this trend was observed for several specimens. The fourth CIP and heat treatment has only been explored for one specimen; thus it is not clear if the decrease is a general trend for the process (see Table 3). In addition to producing a superconducting bar for current-lead applications, this thermomechanical process provides a method to produce high-quality stock for sinter forging.

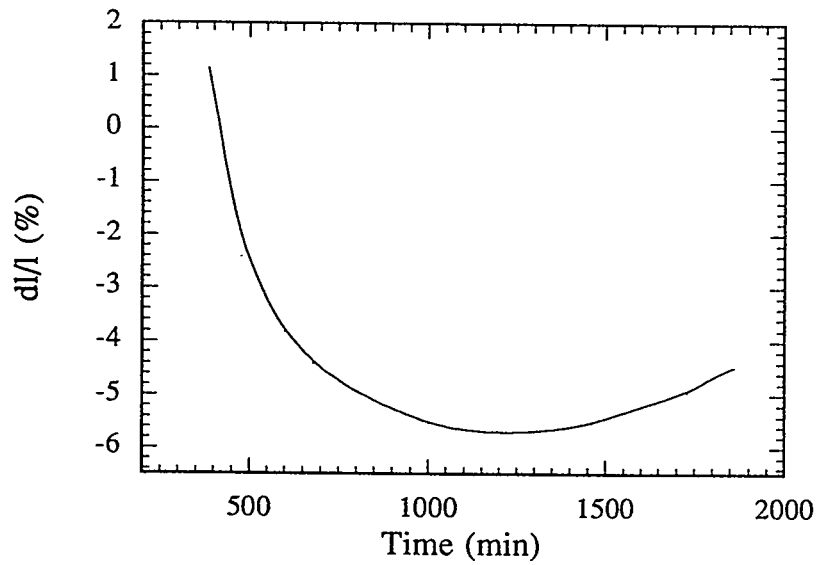

Fig. 26. Dilatometer data for bulk Bi-2223 sample.

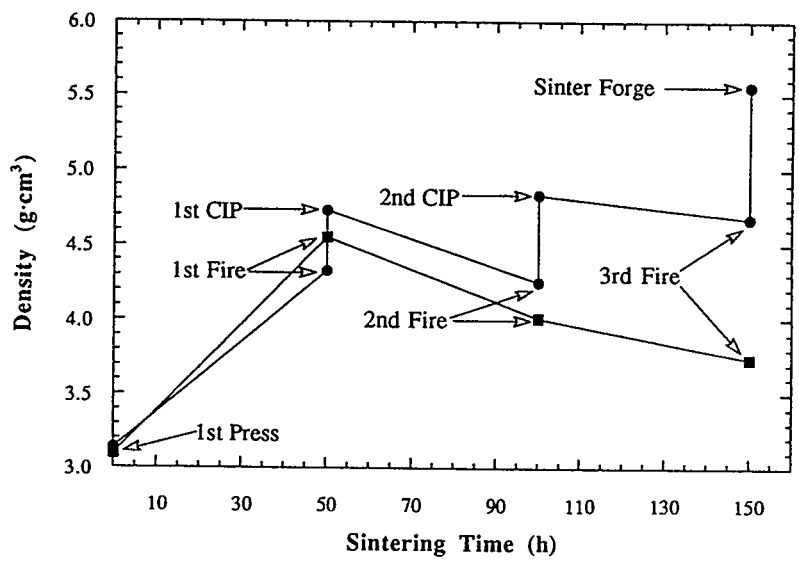

Fig. 27. Density improvement by intermittent CIPing. Control bar was heated for 150 h without intermediate pressing. Test bar was cold-isostatic pressed two times during the 150 h heat treatment.

Table 3. Electrical properties during thermomechanical sequence

Step	J_c (A/cm^2)
First CIP, First Heat Treatment	13
Second CIP, Second Heat Treatment	570
Third CIP, Third Heat Treatment	912
Fourth CIP, Fourth Heat Treatment	230

2.2 Tl–M–Sr–Ba–Ca–Cu–O Superconductors

The goal of this part of the ANL program is to develop a useful conductor for high-temperature, high-field applications, with Tl–1223 the most promising candidate at present. The rationale is the improved flux pinning properties of Tl–1223 at 77 K compared to Bi–2223 (Kim et al., 1991; Gray et al., 1994), and the potential for improved intergranular coupling, first demonstrated by General Electric (DeLuca et al., 1992). Our progress to date indicates that good phase purity and grain alignment are necessary, but not sufficient to obtaining the highest J_c in Tl–1223: it also is necessary to avoid significant intergranular weak links. Processing in the presence of a transient liquid phase seems to be a very effective way to accomplish this.

Our mission is to identify synthesis and processing procedures that will overcome the intergranular weak-link problem in Tl–1223. Our approach is to concentrate on finding and using transient-liquid phases at the crucial step in processing to assist in grain orientation and improved intergranular connectivity, while preserving reasonable phase purity. This program includes various powder-in-tube (PIT) configurations and thick (20–50 μm) coatings; much of it involves research agreements with General Electric (GE), Intermagnetics General, State University of New York at Buffalo (SUNY–Buffalo), and the Thallium Working Group. We also evaluate and quantify weak links by TEM and transport measurements.

2.2.1 Technical Achievement and Progress

Powder–in–tube Tl–1223

Based on our success with the two-powder process for Bi–2223 and the recommendations of last year's review panel, we have applied variants of the two-powder process to Tl–1223. Analogous to Bi–2223 superconductors, effects of starting phase assemblage and liquid-phase sintering on J_c were studied for Ag-clad 1223 tapes (Biondo et al., 1994).

Three different powders were synthesized from mixed oxides and carbonates: phase-pure Tl–1223, Tl–1212 + $CaCuO_2$, and Tl_2O_3 + 0223. The $CaCuO_2$ phase consisted of Ca_2CuO_3 and CuO phases. The 0223 phase consisted of $BaCuO_2$ and Ca_2CuO_3 phases. Tapes were made by a PIT process. Heat treatment temperatures were selected on the basis of acoustic velocity results (Poeppel et al., 1993). The dependence of melting temperature on pO_2 was determined for 100% O_2, 8% O_2/92% N_2 and 1% O_2/99% N_2 gas mixtures. Tapes were heat treated between 675°C and 920°C for 0.5 h.

All tapes had similar dependencies of J_c on heat-treatment conditions; only data from the phase-pure Tl–1223 powder are presented. Correlation between J_c and melting temperature is shown on Fig. 28. For 100% and 8% O_2, the heat treatment temperature at which J_c is a maximum was associated with the melting temperature. However, for 1% O_2, the heat-treatment temperature at which J_c is a maximum was significantly lower than the melting temperature.

Rapid sintering kinetics from solid-state diffusion is unlikely below 800°C (Routbort et al., 1993), and the melting point is about 800°C for Tl–1223 in 1% O_2. These data suggest that gas-phase sintering is important at low pO_2. This assumption is supported by the thermodynamic work of Holstein (1992), in which the Tl_2O_3 partial pressure is inversely proportional to pO_2. The partial pressure of Tl_2O (3×10^4 Pa) is potentially high enough to promote sintering and a small amount of connectivity between grains to support a transport current.

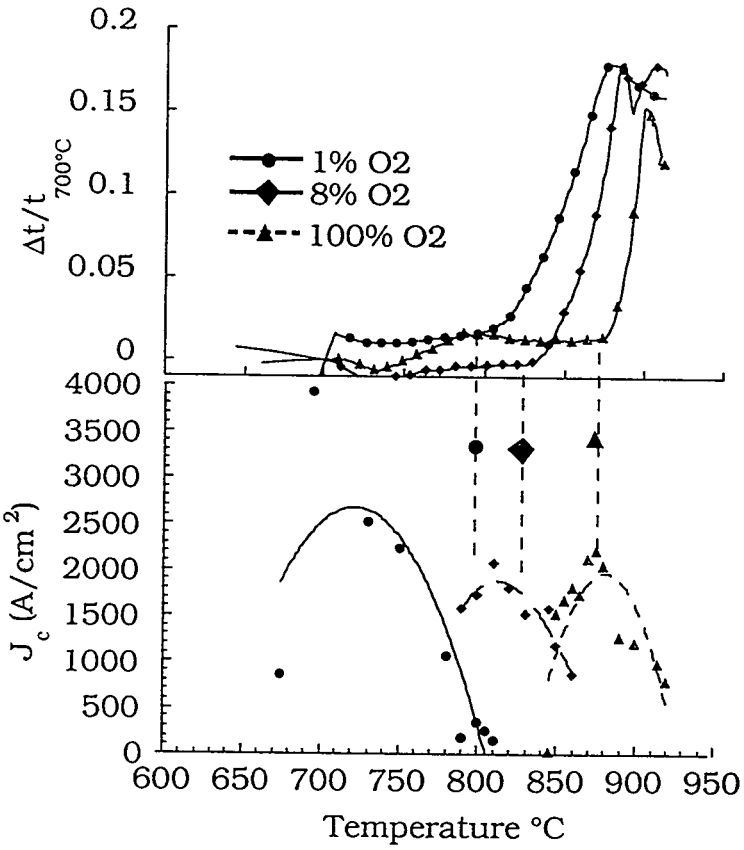

Fig. 28.
Onset of melting correlated with J_c for Tl-1223 tapes.

Preliminary microstructural data show that no texturing was observed for any of the annealing times or temperatures. In addition, a significant amount of porosity was found at low sintering temperatures.

Future work will focus on effects of stoichiometry and sintering conditions on liquid-phase formation. Melting temperature will be monitored by acoustic velocity and will be altered by Bi and Pb additions. The composition of the liquid phase will be determined from microstructural analysis of quenched specimens. In addition, effects of sintering atmosphere and temperature on microstructure and electrical properties will be examined.

We have continued to work with SUNY-Buffalo on fabrication of PIT tapes (Ren et al., 1994). The principal variable examined recently was carbon content of the starting powder. In these studies, $Ba_2Ca_2Cu_3O_x$ precursor was prepared in-house and $Pb_{0.5}Sr_{1.6}Ba_{0.4}Ca_2Cu_3O_x$ precursor was obtained from Sandia National Laboratories. These powders were heat treated in flowing O_2 at total pressure of ≈400 Pa. The resultant powders consisted of complex oxides, with total carbon concentrations of ≈300 ppm; they were combined with Tl_2O_3 powder and sealed into Ag tubes. Mechanical working into tapes was performed at SUNY-Buffalo, and heat treatments were performed at all three institutions. To date, J_c values have exceeded 10^4 A/cm^2 at 77 K. These values are approximately 50% of those obtained with higher-carbon-content powders produced at SUNY-Buffalo. All tapes were fired in short sections, and it is possible that carbon evolved easily during heating. If so, carbon content may not be of much importance in such experiments.

We have also studied the microstructure of PIT tapes made in collaboration with SUNY–Buffalo. Tapes examined exhibit the highest J_c values in the U.S., >2 x 10^4 A/cm^2 at 77 K, persisting to 24–m lengths (Ren and Wang, 1993). These tapes benefit from excellent mechanical processing and show a dense but unaligned microstructure. Our present studies of the microstructure of PIT wires have focused on identifying the crucial processing factors that lead to improved critical currents. By examining segments cut from wires at various stages in the process, we have been able to follow phase development and identify key factors in thermomechanical processing. For example, we have found that Tl–1212, which coexists with Tl–1223 in the early stages of processing, deforms preferentially, providing some cushion for the Tl–1223. In spite of this, the main benefit of the mechanical working is to increase the density in the core rather than improve the texture (Fig. 29).

We are currently carrying out similar studies on Tl–1223 films, in collaboration with SUNY–Buffalo. These films are grown by a vapor transport process and thus provide a valuable comparison with PIT technology and insight into the limits of texture development. Preliminary results suggest that Ag plays an important role in furthering formation of Tl–1223 by helping Tl–1212 and cuprate phases to combine. In the absence of Ag, this process is halted.

We have developed a new method for making sandwich–type conductors that incorporate large platelike grains of Tl–1223. Using this simple process, we have achieved a much higher degree of texture than has been attained in conventional PIT wires, although to date the transport properties have not been significantly better due to poor coupling of grains (Fig. 30).

The continued focus of this work will be to improve grain coupling without diminishing texture. These studies will utilize an optimized phase assemblage, determined from decomposition studies, to bond the aligned grains. The role of [001] twist grain boundaries is likely to be important due to their prevalence in textured polycrystalline conductors. We will study the transport behavior and microstructure of this type of boundary, using techniques we have developed to examine both transport and microstructure on the same grain boundary. Results of these measurements on individual boundaries will be used to refine models of I(V) behavior in polycrystalline samples.

In support of the PIT work, we have continued to synthesize small batches of high–quality Tl–1223 powders. Compositions prepared were $TlBa_2Ca_2Cu_3O_x$ (Tl–1223), $Tl_{0.78}Bi_{0.22}Sr_{1.6}Ba_{0.4}Ca_2Cu_3O_x$ (Bi–doped Tl–1223), $Tl_{0.6}Pb_{0.5}Sr_{1.6}Ba_{0.4}Ca_2Cu_3O_x$ (Pb–doped 1223), $Tl_{0.6}Cr_{0.5}Sr_{2.0}Ca_2Cu_3O_x$ (Cr–doped Tl–1223), and $Tl_{0.6}V_{0.5}Ba_{0.4}Sr_{1.6}Ca_2Cu_3O_x$ (Cr–doped Tl–1223). The Bi–doped compound is easy to synthesize in nearly phase–pure form (Ren and Wang, 1993). Work on the compound has been done in conjunction with SUNY–Buffalo. The Pb–doped compound has been studied in collaboration with Los Alamos National Laboratory (LANL) and Sandia National Laboratories. The CR and V doping studies are in collaboration with the University of Arkansas (Chen et al., 1993b; Li et al., 1994). All of the doped compounds examined exhibit improved irreversibility behavior relative to undoped Tl–1223.

Tl–1223 coatings

The successful GE process for Tl–1223 uses spray–pyrolyzed precursors which have significant porosity. We seek to determine if denser precursors can provide advantages of better intergrain connectivity after annealing. We have used pulsed–laser deposition (PLD) to make atomically dense precursors that exhibit highly textured, phase–pure Tl–1223 microstructures after annealing, with $J_c \approx 3x10^4$ A/cm^2 at 77 K. It appears, however, that

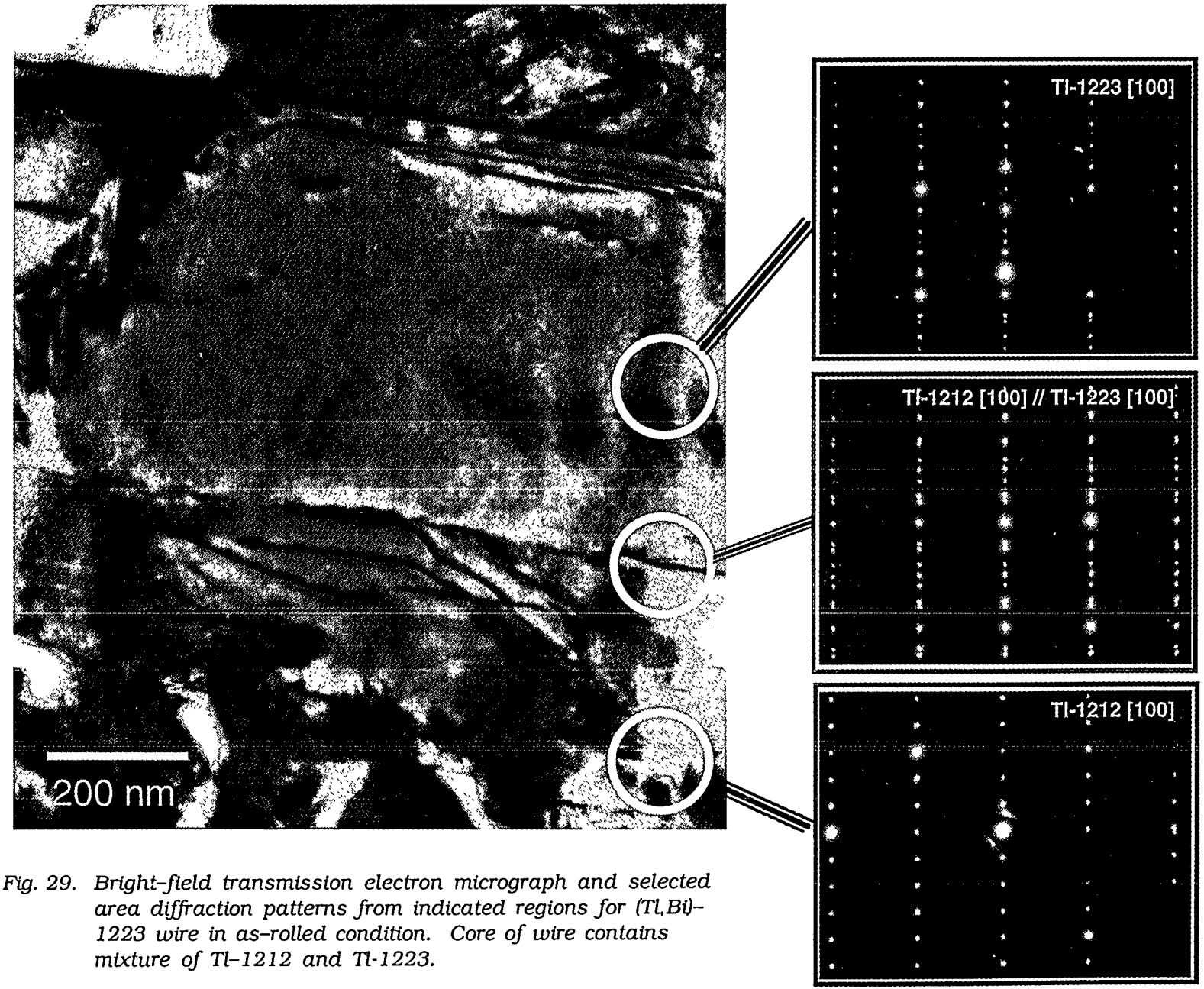

Fig. 29. Bright-field transmission electron micrograph and selected area diffraction patterns from indicated regions for (Tl,Bi)-1223 wire in as-rolled condition. Core of wire contains mixture of Tl-1212 and Tl-1223.

(a)

100 μm

(b)

10 μm

Fig. 30. Scanning electron micrographs of sandwich-type conductor prepared with plate-shaped Tl-1223 grains: (a) structure of wire observed at low magnification, revealing nonuniformity in core thickness; (b) reasonably well-aligned superconducting grains, despite presence of large fraction of impurity phases (dark).

the amount of Tl that can be incorporated by the vapor-transport method may be limited. While this may contribute to lower J_c, we also need to better control all cation concentrations.

Based on the GE success with spray pyrolysis and two-zone thallination to make 3 μm films of Tl-1223, we have developed an ink technique to make 20-50 μm coatings. Continued studies of the effects of Ag on growth show that films containing about 10 mol% Ag and annealed between 860 and 870°C produce phase-pure Tl-1223 with very strong 00*l* lines and platelike growth throughout the entire thickness. Ag-free precursors result in randomly oriented films with weak X-ray lines, small unmelted particles, and very poor J_c values. It is speculated that Ag acts as a flux to form a low-melting-point eutectic, after which it is rejected and segregates into small particles at the film surface. Similar studies done on Bi- and Sr-substituted films show little evidence for melting and improved orientation. However, they do show better J_c values (6800 A/cm^2 at 77 K in 16-μm-thick films) than in unsubstituted films, even though they have randomly oriented platelike growth. This technique is now being pursued at GE as well.

We have also made epitaxial deposits of Tl–1223, some of which were annealed at GE, with the goal of establishing the intrinsic field dependence and ultimate value of J_c within grains, i.e., without weak–link effects. There was an increase in J_c of about five times over the thicker, polycrystalline deposits of GE, but the irreversibility behavior was essentially the same. Samples were irradiated at the ANL ATLAS Heavy–Ion Accelerator, and while the irreversibility crossover increased by roughly the same factor of 3 that Oak Ridge National Laboratory (ORNL) staff found for Bi–2212 crystals, the low–field J_c at 77 K did not increase by the same factor. This is consistent with a J_c limitation by residual weak links, even in these "epitaxial" deposits; our progress has been the establishment of a new lower limit on potential J_c in Tl–1223.

2.2.2 Planned Activities

Phase development

This is the first key step for achieving our objective of overcoming the intergranular weak–link problem in Tl–1223. An optimized phase assemblage can provide controlled phase purity, the best reaction path, and improved reactivity, which translates into lower synthesis/processing temperatures. We previously found that a well–aligned, connected microstructure in Bi–2223 was aided by our two–powder process, and further decomposition studies revealed the two powders for Bi–2223, albeit a posteriori.

Thus, our main approach toward an optimized phase assemblage will be to use phases that evolve during the decomposition of Tl–1223. This approach is suggested by the fact that decomposition of Bi–2223 results in the same phase assemblage developed for the two–powder process, indicating that a knowledge of the decomposition products can be used to facilitate the search for an optimal phase assemblage. In these studies, samples will be equilibrated at high temperatures in various atmospheres and then quenched. The resultant phase assemblage will be identified by X–ray diffraction and electron microscopy. These phases will then be recombined to form Tl–1223, with particular emphasis on those assemblages that yield a transient–liquid phase. After our planned decomposition studies determine the optimized phase assemblage in Tl–1223, we will apply them to conventional PIT and thick deposits made from inks.

Improved grain connectivity

We have demonstrated that grain alignment alone will not yield high J_c for either PIT or thick coatings. Our approach will be to concentrate on finding and using transient–liquid phases at the crucial step in processing to assist in grain orientation and improved intergranular connectivity, while preserving reasonable phase purity. Specifically, we will search for transient–liquid phases by quenching during processing, using our acoustic velocity measurements as a guide, followed by TEM imaging to find amorphous signatures of transient liquids and their composition. We will study small variations on the optimized phase assemblages, if necessary, to provide the transient liquid. Such results can also guide us to appropriate compositions to be used to bond large, preformed, oriented grains of Tl–1223 in Ag sandwiches, and to determine if conditions can be found for reaction–induced texturing as we found in Bi–2223.

Low–temperature processing

This research, which is currently performed entirely by D. G. Hinks (ANL) with funding by the Department of Energy–Basic Energy Sciences, and National Science Foundation–Science and Technology Center for Superconductivity, offers the opportunity to drastically change the conditions under which HTS materials can be fabricated into

wires. For example, Hinks has synthesized phase-pure Tl-2201 and Tl-2212 at temperatures as low as 550°C. The method should be amenable to both PIT and coating technologies. We aim to develop this technique for Tl-1223 now, and possibly for other compounds in the future.

2.3 YBCO and HBCCO Superconductors

2.3.1 Melt-Processed YBCO

Melt-processed bulk YBCO superconductors have promise in applications such as low-friction superconductor/permanent magnet bearings and flywheel-energy-storage devices (Balachandran et al., 1993b). The properties of YBCO superconductors are improved by melt-processing because large grains align along the c-axis and flux-pinning properties are enhanced (Sengupta et al., 1994).

Fabrication of pellets

Stoichiometric YBCO powder was prepared (Balachandran et al., 1992) by calcination of Y_2O_3, $BaCO_3$, and CuO in low O_2 pressure. About 6-80 mol% fine agglomerates of 211 from a commercial source were mixed into the YBCO powder. For experiments with Pt additions, ≈0.5 wt.% fine Pt powder was mixed with YBCO and 211 by mortar and pestle. Pellets (2.5-4.5 cm in diameter, 0.3-1.0 cm thick) of YBCO, YBCO + 211, YBCO + Pt, and YBCO + 211 + Pt were pressed. A $Sm_{1+y}Ba_{2-y}Cu_3O_x$ (Sm-123) single crystal was embedded on the surface of the pressed sample for some experiments. Samples were heated to ≈1070°C, cooled at ≈1°C/h to ≈960°C, and then cooled at ≈60°C/h to room temperature. These melt-processed samples were then annealed in O_2. Levitation forces were measured over a small rare-earth permanent magnet (12.8 mm diameter, 5 mm thick, B = 2.8 kG).

Levitation force vs. distance between superconductor and the permanent magnet is shown in Fig. 31. Zero-gap force (Fo) can be obtained by extrapolating the data points toward zero. Solid-state sintered YBCO sample has Fo ≈0.18 N, whereas Fo values of melt-processed YBCO, YBCO + 211, and YBCO + Pt are ≈0.9 N, ≈1.0 N, and ≈1.4 N, respectively. Melt-processed YBCO prepared with a Sm-123 seed produced large domains of YBCO, and Fo was ≈4.9 N. Under an applied temperature gradient and using the seeding technique, we have now obtained Fo = 10 N. The increase in levitation force is the result of enhanced flux pinning, increase in domain size, and improvement in texture throughout the sample.

Preparation of seed crystals

Processing of commercially supplied large-domained YBCO pellets for levitation applications requires a large number of seed crystals to initiate heterogeneous nucleation and directional solidification during processing. To satisfy this need, a new method to grow and harvest a large number of $ReBa_2Cu_3O_x$ crystals has been developed. Re refers to a rare-earth element; neodymium is the preferred element because it forms the compound with the highest melting temperature (Osamura et al., 1991).

$Nd_{1+y}Ba_{2-y}Cu_3O_x$ (Nd-123) crystals are produced by a flux-growth method. Precursor powders of $BaCO_3$, CuO, and Nd_2O_3 (mole ratios between 3:10:1 and 6:20:1) are placed in an Al_2O_3 crucible and heated above the melting point of Nd-123 (Todt et al., 1994 and 1995). The melt is cooled slowly at ≈1°C/h to 1000°C, where the crucible contents are quenched to room temperature on a Cu block. For separation of flux and Nd-123 single crystals, a method has been developed that is based on capillary forces and the good wetting behavior between the Ba-Cu-O-rich flux and 211. The quenched mass consisting

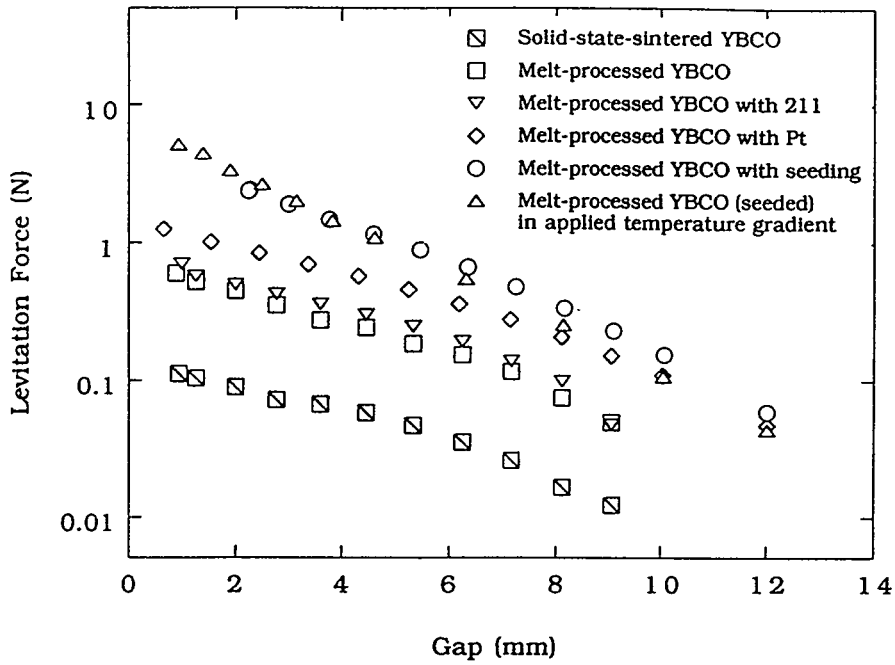

Fig. 31. Levitation force vs. distance between YBCO superconductors and permanent magnet.

of crystals and solidified flux is placed on a porous, presintered 211 substrate and then heated to about 1060°C, which is 10°C below the melting point of Nd–123 (Osamura et al., 1991). At this temperature, the flux penetrates the porous substrate easily because of capillary forces. The seed crystals remain on the surface. After cooling, the crystals can be harvested easily (Fig. 32). Several dozen single–crystal seeds can typically be harvested from a single 20–25 g batch.

Annealing studies

Oxygenation anneals for thick sections of YBCO can require many days. Quite some time ago, it was observed that the rate at which oxygen diffuses into YBCO increases with increasing oxygen content of the YBCO. This counterintuitive fact opens the possibility for significantly decreasing the time required to anneal YBCO.

Optimal properties are obtained when final oxygenation of YBCO takes place at ≈450°C. In general, an optimal annealing schedule will take advantage of initial higher temperatures and some sort of ramped cooling to increase the oxygen content gradually, but quickly. Recent modeling work for randomly oriented polycrystalline YBCO has shown that continuous cooling can be used and that the time needed to oxygenate a section can be reduced by one order of magnitude relative to simple isothermal holds at 450°C (Seoul and Cha, 1994). Although the final oxygen content is the same for both processes, the cooling offers two significant advantages: much shorter annealing times and reduced propensity to microcrack because transformation stresses are much lower at any given time.

The new method has recently been applied to large melt–textured pellets of YBCO. These pellets have strong c–axis textures, and thus oxygenation requires additional time because oxygen diffusion is slow in the c direction. Nevertheless, oxygenation annealings have been reduced from 10 days to 3 days, and the final properties of the pellets have exhibited slight improvements.

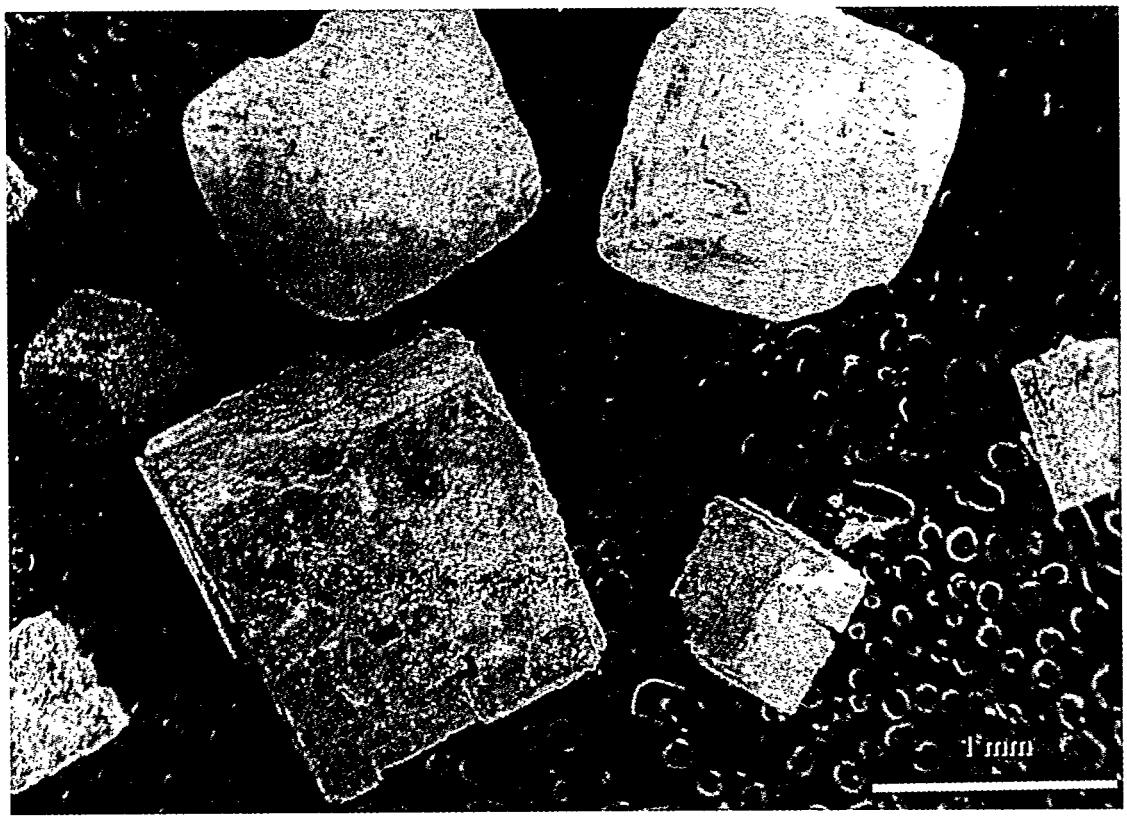

Fig. 32. Photograph of harvested Nd-123 seed crystals.

2.3.2 HBCCO and New Materials

Over the past year, we have examined various methods to produce dense, highly phase-pure specimens from HBCCO powders. To our knowledge, such materials have not been made. In a series of feasibility studies, the simplest compound, $HgBa_2CuO_x$ (Hg-1201), was synthesized in highly pure form (Wagner et al., 1993). The following methods were used for consolidation: PIT processing in an Ag sheath, hot forging, hot isostatic pressing in sealed PT cans, and shock compaction. The shock compaction was performed by W. J. Nellis of Lawrence Livermore Laboratory. The densest material produced to date, ≈80% dense, was shocked at 57 GPa pressure. Superconductivity was retained, although a post-shock annealing was required to optimize the fraction of superconducting material. These materials are now being examined by ANL and by M. J. Kramer of Ames Laboratory.

The low-temperature synthesis process of Hinks can be used to produce HBCCO compounds. It also may provide a convenient source of fine-grained powders (the initial Tl-2212 powders produced were ≈1-2 μm) for phase assemblages used in direct synthesis and as bonding phases for large, preformed, oriented grains. Another material besides Hg-1223 that shares excellent irreversibility behavior with Tl-1223 is (Cu,C)-Ba-Ca-Cu-O (1234), presently made by high-pressure synthesis, with T_c = 117 K. We would like to investigate low-pressure synthesis from a molten salt, an approach which lends itself to electrochemical means of control, for preparation of this material.

2.4 Properties of Bulk High–T_c Superconductors

2.4.1 Characterization Methods

Ceramic superconductor samples produced in ANL projects are characterized to help guide improvement of the chemical formulations and the forming and processing procedures. High-T_c products fabricated for application in devices also are characterized to evaluate product performance. The property of primary interest is the DC transport critical current of the sample, measured as a function of intensity of an applied magnetic field. Power loss due to AC transport, as a function of frequency, current, temperature, and ambient magnetic field, also is of interest for AC applications. Selected samples are tested to find the critical temperature, structural defects, strength of diamagnetic response, remanent–field strength, magnetic–shielding performance, and mechanical properties.

2.4.2 Electrical Characterization of Superconductors

DC characterization

Critical current tests have continued at an average rate of 158 samples per month. Substantial differences among batches of bulk material or formed products made continual screening necessary. The standard four–point resistance method was used with a 1 μV/cm criterion. Sample types consisted primarily of A–clad Bi–2223 tapes under development for magnetic coil applications and YBCO/Ag or Bi–2223 bars and rods for use in current leads. Results are discussed below and elsewhere in this report.

Tests of high–performance superconductors at high currents during this reporting period were supported by our 1200–A pulsed current facility. Tape samples at 77 K were tested individually in a low range, typically 30–50 A, and in parallel assemblies at higher currents. Individual sinter–forged bars of Bi–2223 with 0.5–0.6 cm^2 cross–sectional areas and critical currents to 710 A at 77 K were tested through and beyond their critical values: An example of bar performance is shown in Fig. 33. Applied magnetic fields typical of current–lead applications (50–100 G) decreased the critical current only a few percent. Critical current densities are somewhat higher than those of the melt–cast Bi–2212 discussed in the previous report (Poeppel et al., 1993).

Material from a longitudinally sectioned, sinter–forged bar was pulse–tested at a series of temperatures below 77 K and in applied magnetic fields to 4 kG; results are shown in Fig. 34. The change of slope at 30–35 K under applied magnetic fields may be a result of improved flux pinning below that temperature range (Kim et al., 1991).

AC losses and apparatus upgrade

A slight resistance to alternating current flow is displayed by high–T_c superconductors, even at currents well below the DC critical current, as reported previously (Poeppel et al., 1993). This resistance is associated with magnetic hysteresis of the material. However, appropriate design can limit this power loss to a value sufficiently small for advantageous use of the material in applications such as AC downlinks operated at power–line frequencies. AC losses were evaluated in support of design efforts.

Typical results from a sinter–forged Bi–2223 bar are shown in Fig. 35. The AC losses are less than those of melt–cast Bi–2212 rods of the same cross–sectional area (Poeppel et al., 1993), and this is consistent with the higher J_c of the sinter–forged products tested.

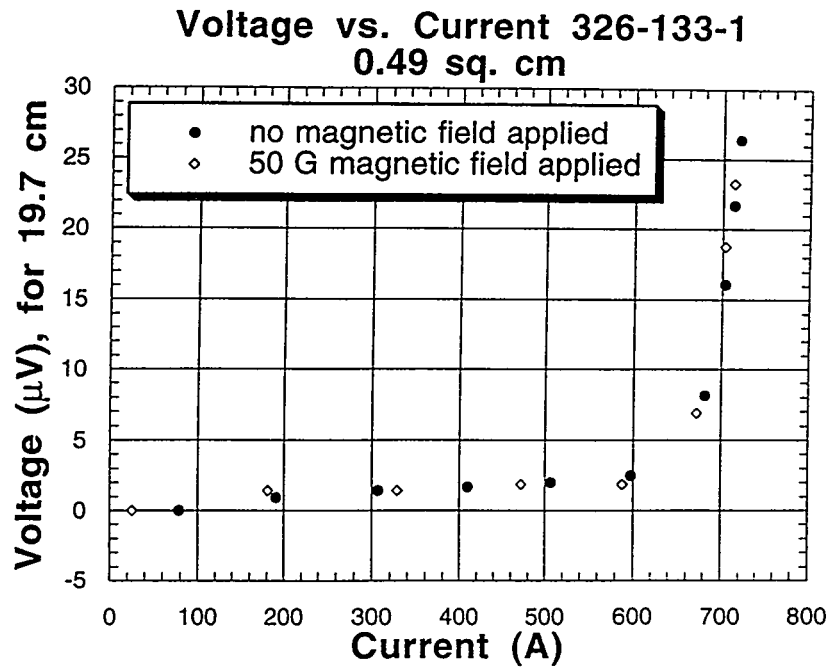

Fig. 33. Critical current test data from sinter-forged Bi-2223 bar at 77 K.

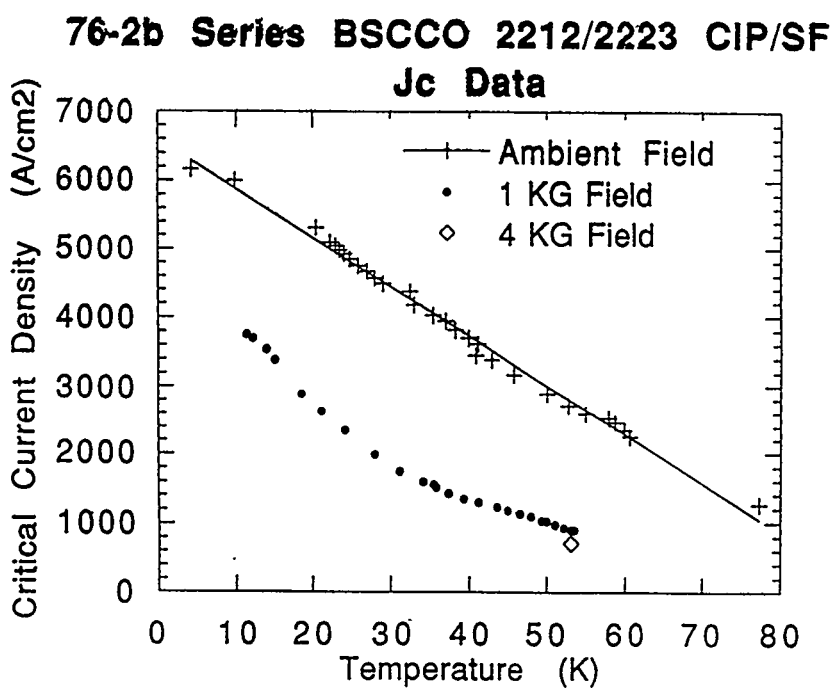

Fig. 34. J_c variation with temperature of sample sectioned from sinter-forged Bi-2223 bar: magnetic self-field, applied fields of 1 or 4 kG.

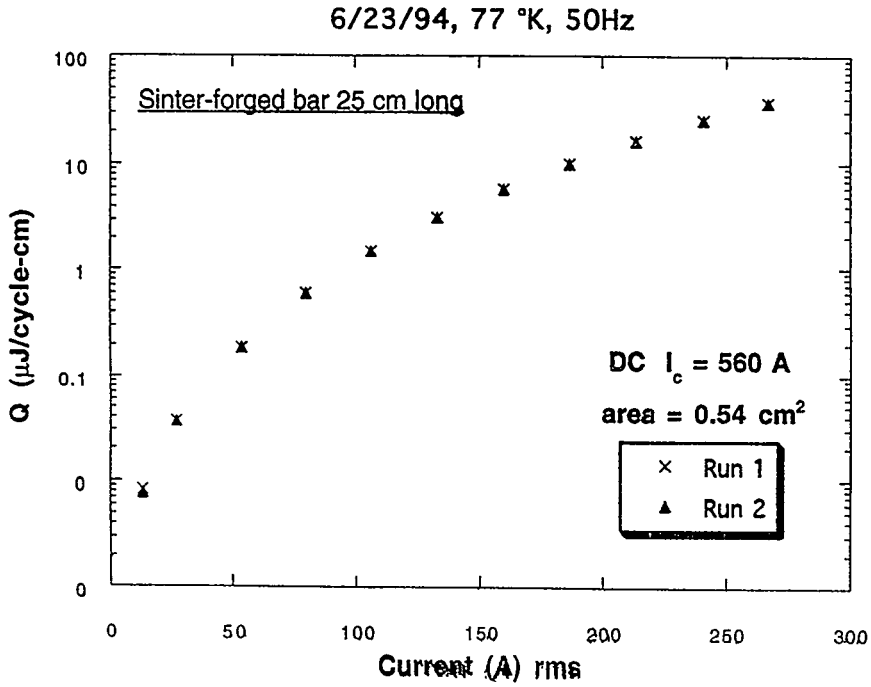

Fig. 35. Power loss vs. AC current in sinter-forged Pb-BSCCO bar at 77 K.

High-current apparatus developed for such AC loss measurements was described in the previous report (Poeppel et al., 1993). The 1500-A (peak) AC, variable frequency source was used to evaluate assembies of parallel bars (see AC downlinks below). More recently, the apparatus was upgraded to provide up to 2150 A RMS (>3000 A peak) variable-frequency sine waves to test an assembly being developed for 2000 A RMS service.

AC downlinks

Two arrays of Bi-2223 bars were designed and produced for use as current leads in a 77-4 K temperature gradient to a power utility fault-current limiter operating in liquid He. A computer spreadsheet program was produced to predict the amount of heat delivered by the bars to the liquid He as 1500 A (peak) of 50-Hz AC current was conducted. In the selected downlink design, each array consisted of four sinter-forged bars in parallel, each bar having a DC critical current density of 950-1300 A/cm^2 at 77 K and >5000 A/cm^2 at 4 K. Magnetic field sensitivity was relatively small. Thermal conductivity tests showed values higher than literature values for polycrystalline Bi-2223 made by other processes. Typical 50 Hz AC power losses at 77 K in each 0.54 cm^2 cross-section bar were 1 mW/cm length at 310 A (peak) and 1.75 mW/cm at 375 A (peak). Losses were much less at 4 K. Bar lengths were 25 cm, including ends having Ag contacts sinter-forged to the ceramic, with 21 cm of length in the thermal gradient between the fixed-temperature terminals. The downlinks are shown in Fig. 36. The calculated amount of heat delivered to the liquid He at full power was only 0.2 W per array. Correctness of the thermal efficiency prediction was supported by He boil-off tests with sinter-forged material conducting 60 Hz current in a similar temperature gradient.

Development is in progress of advanced downlinks for operation at 2000 A RMS within a 100-mm-diameter boundary. A dissipation of <0.4 W per downlink is sought. The moderate increment to the heating load, caused by the increased magnetic self-field, may be offset by further improvement in material grain alignment and bulk density and by

Fig. 36. AC downlinks (shown inverted); each array of four superconductor bars is capable of delivering 1500 A (peak) AC current at line frequency from copper connectors at 77 K to low-temperature superconductor wire leads at 4 K, with less than 0.2 W of heat conducted to the 4 K terminal.

more precise optimization of the superconductor geometry. In addition, modification of the sinter–forging apparatus to produce hollow cylinders rather than bars is being considered: Mechanical strength of a downlink may be improved by substitution of a single cylinder for the several bars, in order to better withstand the greater magnetic force caused by higher current.

2.4.3 Contact Resistivity

Past work has shown that low resistivities of Ag–to–superconductor interfaces can be made by applying Ag powder to surfaces of YBCO–Ag bars prior to sintering of the bars, by joining Ag to Bi–2212 during melt–casting, or by pressing Ag to Bi–2223 during sinter–forging (Poeppel et al., 1993). Recently, tests of soldered lap–joints between Ag–clad Bi–2223 tapes were made. Resistivities per half–joint were 30–40 nΩ cm^2 at 77 K. The joint section consisted of the Ag/Bi–2223 interface, Ag metal thickness, and solder thickness.

2.4.4 Mechanical Properties

Mechanical–property research has continued. Recent efforts have focused on Bi-2212, Bi-2223, and Tl-1223. Effects of Ag additions, texture, and plastic deformation continue to be examined.

Properties of monoliths and composites

Good strength and flexibility are required in most bulk applications. Various composite systems have been developed to improve both strength and toughness of high–temperature superconductors. Fracture toughness, K_{IC}, can be improved by addition of components that dissipate energy from the moving crack front. In general, fiber reinforcement improves K_{IC} by mechanisms related to fiber sliding, crack deflection, crack bowing, or microcrack formation. In many instances, the toughness increase is accompanied by an undesired decrease in strength.

Fabrication of dense composites is complicated because additions may inhibit sintering, agglomerate to form extended flaws in the sintered body, or introduce unwanted impurity phases. In addition, virtually all materials react to some extent with YBCO, Bi-2212, Bi–2223, and Tl–1223. Ideal reinforcements for high-temperature superconductors would be fully compatible chemically and strong mechanically. Y_2BaCuO_5 (211) is in equilibrium with YBCO at processing temperatures and is stronger, more stable, and more refractory than YBCO (De Arellano–López, 1991). 211 may be an excellent reinforcement in fiber form. Experimental 211 fibers were provided by SKY Fibretech (Plainfield, Illinois). For Bi–2212, alkaline earth cuprates such as $(Sr,Ca)_2CuO_3$ are in equilibrium with Bi–2212 during processing. These phases tend to be highly hygroscopic, however, and their success as reinforcements is not ensured. High-quality Bi–2212 fibers are available (Miller et al., 1991), and polycrystalline Bi–2212 may be reinforced with fibers of the same or different composition. The goals of this work were to fabricate dense bars of YBCO/211 and Bi–2212/Bi–2212 composites and to determine whether the reinforcements increased strength or K_{IC}. These reinforcement schemes employed in this study will, in all probability, be of use only in applications for which high J_c is not required.

YBCO and Bi–2212 powders were synthesized from mixtures of oxides and carbonates. Final grinding in a tungsten carbide rotary mill produced powders with average grain size of 2–5 μm. The 211 fibers were obtained as a tangled mass; individual fibers were ≈50–1000 μm long and ≈3–5 μm in diameter. The 2212 fibers were initially amorphous and were longer, thinner, and much smoother than the 211 fibers. Fiber strengths were estimated, by the sizes of fracture–surface mirrors, to be ≈1 GPa (Goretta et al., 1994b).

The fibers were mixed in 15 vol.% concentrations with the matrix powders and isopropyl alcohol. Ball milling reduced the fiber lengths substantially, but most of the fibers were still longer than 50 μm. Mechanical–property data for strength and K_{IC} are summarized in Table 4. For these sets of samples, which were all 85–90% dense, the fiber additions imparted modest improvements. J_c values were affected minimally by the fiber additions. The results to date offer some promise, but not enough to justify additional effort over the next year. The principal drawback to fiber additions is that they retard densification, and mechanical properties of high–temperature superconductors are strong functions of density (Martin et al., 1993).

Elastic–moduli studies continued in collaboration with the University of Bath, England. Following the success of measuring highly–textured Bi–2212 bars (Fanggao et al., 1993), we have supplied sinter–forged Bi–2223 and Tl–1223 bars. However, neither of these

Table 4. Summary of property data for monolithic and fiber/composite bars

Sample	Strength (MPa)	K_{IC} (MPa[m]$^{0.5}$)
YBCO	110 ± 15	1.4 ± 0.4
YBCO/211	100 ± 30	1.9 ± 0.3
Bi-2212	95 ± 15	1.5 ± 0.3
Bi-2212/Bi-2212	105 ± 10	1.8 ± 0.4

samples has the very high degree of phase purity of the Bi-2212 bars, and the quality of the data may not be so good. Studies have also been expanded to include the effects of oxygen content on the moduli of high-T_c superconductors (Cankurtaran, 1994).

As discussed previously (Poeppel et al., 1993), a goal of 0.2% strain to failure for clad tapes will be difficult to attain reliably, because the high-T_c superconductors are elastic solids, and thus $\sigma = e\,E$, where σ is the strength, e the strain, and E the modulus. A strain of 0.2% implies strengths > 200 MPa, which will be a challenge to attain reproducibly.

High-temperature deformation

High-temperature deformation is an important consideration for hot rolling because both the sheath and core are deformed. For Bi-based superconductors, the core can contain small amounts of phases such as $(Sr,Ca)_2CuO_3$, $(Sr,Ca)_{14}Cu_{24}O_x$, and CuO. Each phase in the composite will have a different plastic response. Of the many possible alkaline-earth cuprates to examine for high-temperature properties, Ca_2CuO_3 was selected because it can be readily synthesized in highly pure form and sintered to high density. To evaluate the mechanical properties of Ag, Bi-2212, Ca_2CuO_3, and CuO at high temperature, constant-strain-rate compression tests were performed (Schwartz et al., 1994; Goretta et al., 1994a,c).

Specimens were compressed at 800-990°C at an initial strain rate of 10^{-6}–10^{-5} s^{-1}. Most data were taken at 825°C, which is a typical temperature for hot rolling 2212 tapes (Schwartz et al., 1994). Load-versus-time data were recorded and stress-strain curves were generated. Typical curves are shown in Fig. 37. Dynamic recrystallization took place during deforming the Ag. At room temperature, the compressive fracture strength of Bi-2212 was ≈180 MPa, that of the Ca_2CuO_3 was ≈240 MPa, and that of CuO was ≈250 MPa. Both the Bi-2212 and Ca_2CuO_3 exhibited partially plastic responses when compressed at 825°C. CuO exhibited extensive plasticity at 870°C. However, the decreases in stress shown in Fig. 1 indicate occurrence of fracture. The average maximum strength was ≈20 MPa for the Bi-2212 and ≈160 MPa for the Ca_2CuO_3. The CuO exhibited sufficient plasticity that steady-state creep could be quantified. Above ≈870°C, the strain rate ($\dot{\varepsilon}$) could be expressed as

$$\dot{\varepsilon} = A\,\sigma^{2.96 \pm 0.45}\,pO_2^{-1/(0.8 \pm 0.3)} \exp -(362 \pm 130\ \mathrm{kJ/mole/RT}) ,$$

where A is a constant, σ is the steady-state stress, pO_2 is the oxygen partial pressure, and R and T have their usual meanings. The data, supported by TEM observations, indicated that the kinetics of creep were controlled by dislocation climb. Diffusional kinetics were controlled by motion of oxygen vacancies.

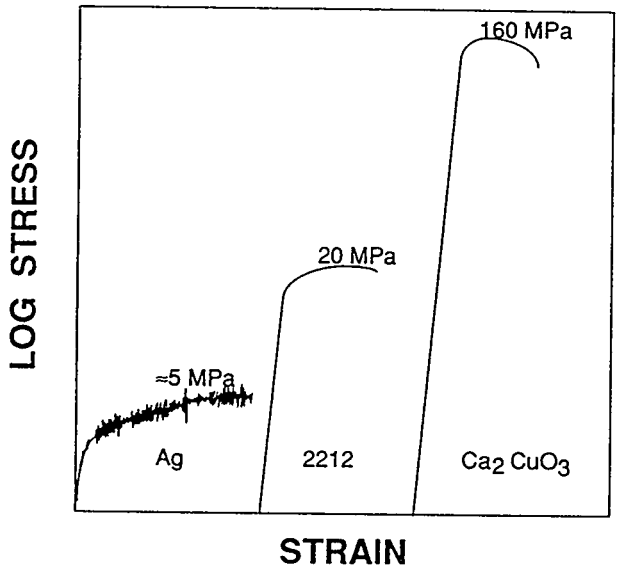

Fig. 37.
Schematic stress/strain curves at 825°C for materials shown.

The plastic responses of Ag, Bi-2212, Ca_2CuO_3, and CuO clearly indicate the need for good phase purity of the core when hot rolling. The Bi-2212 will exhibit substantially more plasticity than the alkaline-earth cuprates. Bi-2223 would be expected to be less plastic than Bi-2212, but much more plastic than Ca_2CuO_3 or CuO (Goretta et al., 1994a,c).

Additional high-temperature mechanical-property studies completed in support of hot rolling include measurement of friction between Bi-2212 and Ag as a function of temperature (Fang et al., 1994), examination of the phase stability of Bi-2212 under high-temperature deformation (Miller et al., 1993a), and steady-state creep studies of high-temperature superconductors, including Tl-1223 (Routbort et al., 1993 and 1994; Dominguez-Rodriguez et al., 1994).

2.4.5 Nondestructive Evaluation

Ultrasonic examination of tapes

A technique using ultrasonic velocity of sound has been developed to monitor incongruent melting during the fabrication of high-T_c tapes. The liquid phase is essential in achieving the proper phase development, grain alignment, and electrical properties. Sound velocity is sensitive to the amount of liquid present and to microstructural variations. Therefore, ultrasonic monitoring can provide valuable insight into fabrication processes and help to optimize them. This technique has been discussed previously (Poeppel et al., 1993).

A demonstration of how this technique can be used for in-situ process monitoring on a continuously moving tape has been completed recently. By use of two magnetostrictive transducers and remendur/Inconel rods of appropriate length, an ultrasonic thin-rod wave can be launched by one transducer and received by the second, permitting the velocity of sound to be determined between them. The rods need only rest on the tape to generate and detect the ultrasonic wave, thus eliminating need for a ceramic coupling. This method results in lower signal amplitude than when a ceramic joint is used. However, once the initial experiments with the ceramic cement bond have been completed and critical parameters determined, the two-probe method will be sufficient for continuous process monitoring of tapes. The attenuation of sound is very low at 100 kHz, and thus sections of the tape on the order of meters in length can be examined if desired.

We can assume that the long and narrow tape can be treated as a thin rod. This assumption allows for calculation of the Young's modulus (E) of the superconductor core (including E as a function of temperature) from the density and velocity of sound data of pure Ag and BAg–clad tapes. From the assumption that the tape can be treated as a thin rod it follows that

$$E = \rho V^2 \tag{1}$$

where ρ is the density and V is the longitudinal velocity of sound. The second assumption, which appears to be valid, is that the Reuss model (constant stress in the two constituents of a composite) applies to the calculation of velocity of sound in the superconducting composite tapes. Thus,

$$1/E_{comp} = f/E_{HTCS} + (1-f)/E_{Ag} \tag{2}$$

where f is the volume fraction of the superconductor (HTCS), (1–f) is the volume fraction of the Ag, E_{HTCS} is the Young's modulus of the HTCS and E_{Ag} is the modulus of the Ag. A standard pulse–echo technique for determining the velocity of sound was used to establish the room temperature modulus of silver as 70.91 GPa. The experimentally determined modulus at room temperature for a Bi–2223/Ag tape is 53.43 GPa, and from Eq. 2, the modulus of Bi–2223 is found to be 30.71 GPa. We have also measured the temperature–dependent velocity of sound for a pure Ag tape, which decreases monotonically and decreases about 15% from room temperature to 900°C.

In view of the Ag data, the sharp decrease in longitudinal velocity of sound in the tape at high temperature is attributed to the sharp drop in the elastic modulus of the Bi–2223 due to the presence of the liquid phase or other changes in microstructure. To better understand the sharp change in velocity of sound in the tape, we restate Eq. 2 to account for the change in modulus when liquid is formed. If we assume the thin rod relation of Eq. 1, where $E = C_{11} = \lambda + 2\mu$, Eq. 2 can be written as

$$1/(\lambda + 2\mu)_{comp} = f/(\lambda + 2\mu)_{HTCS} + (1-f)/(\lambda + 2\mu)_{Ag} \tag{3}$$

where C_{11} is the longitudinal elastic constant, λ the Lame' constant, μ the shear modulus, and $(\lambda + 2\mu)$ is the modulus of elasticity (Cottrell, 1964). The term μ is zero for a liquid. Thus, Eq. 3 can be written in two ways, one for the composite before melting and one when the Bi–2223 is melted. These equations are presented below as Eqs. 4 (before melting) and 5 (after melting).

$$1/(\lambda + 2\mu)_{comp(sol+sol)} = f/(\lambda + 2\mu)_{BSCCO\ solid} + (1-f)/(\lambda + 2\mu)_{Ag} \tag{4}$$

$$1/(\lambda + 2\mu)_{comp(sol+liq)} = f/(l\ )_{BSCCO\ liquid} + (1-f)/(\lambda + 2\mu)_{Ag} \tag{5}$$

Equations 4 and 5 can be rewritten, substituting the notation $M_{S,S}$ for modulus of elasticity of the composite with solid Bi–2223 and $M_{S,l}$ for modulus of elasticity of the composite with liquid Bi–2223. For the liquid BSCCO, $\lambda = K_{BSCCO,liq}$, where K is the bulk modulus (Cottrell, 1964). For the Ag and solid Bi–2223, $E = \lambda + 2\mu$, thus

$$1/M_{s,s} = f/E_{BSCCO\ solid} + (1-f)/E_{Ag} \tag{6}$$

$$1/M_{s,l} = f/K_{BSCCO\ liquid} + (1-f)/E_{Ag} \tag{7}$$

From Eq. 1, we can show that the change in elastic modulus during the formation of the liquid phase is approximately twice that of the change in velocity, thus

$$\Delta M/M_{s,s} \cong 2\ \Delta V/V = -\ 2\ \Delta t/t \tag{8}$$

We can predict the change in the ultrasonic echo transit time from the variation of elastic modulus during formation of liquid and compare it to experimental observation. If K for the liquid phase is not known, we can use, for an isotropic solid,

$$K = E/[3(1 - 2\nu)] \tag{9}$$

where ν is the Poisson ratio. For ν = 0.23–0.28, which is typical for a solid, K = 0.62–0.75 E. For an isotropic solid we can then write $\Delta M/M_{s,s}$ as a function of f. Equation 10 below shows, as an example, the equation for K/E = 0.75.

$$\Delta M/M_{s,s} = 2(\Delta t/t) = (f/3)(M_{s,l}/E) \tag{10}$$

A test of this model was carried out on a tape of NaCl sheathed in Ag. Figure 39 shows the change in transit time for the NaCl/Ag tape near the melting point of NaCl. For K = 25 GPa and E = 40 GPa for NaCl at ≈800°C and E = 61 GPa for Ag, we can predict $\Delta t/t$ as a function of volume fraction of NaCl. The result based on Eqs. 6 and 7 is shown in Fig. 39, along with the experimental observation from Fig. 38. The volume fraction of NaCl is estimated to be 0.25, which is in good agreement with the actual value.

Phase–pure and doped Tl–1223/Ag ribbons exposed to different pO_2 values continued to be studied. Results for phase–pure material are shown in Fig. 40. Shift in the initiation temperature of the melting phase is evident. Results for three $Tl_{0.78}Bi_{0.22}Sr_{1.6}Ba_{0.4}Ca_2Cu_3O_x$ (doped Tl–1223)/Ag ribbons are shown in Fig. 41. The shif in the initiation temperature of the melting phase is seen, although little melting is evident for the 100% O_2 specimen.

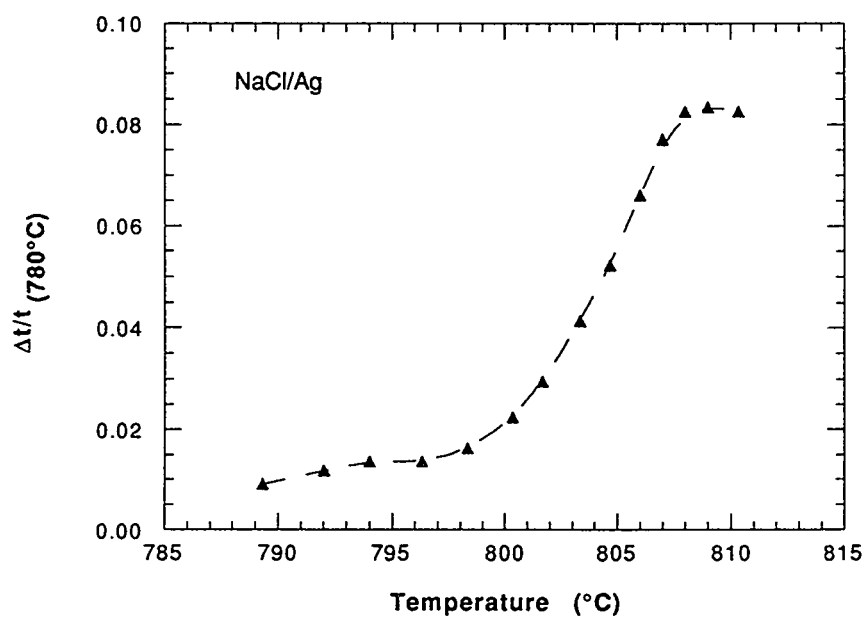

Fig 38. Variation of ultrasonic echo transit time relative to that at 780°C for ribbon consisting of NaCl sheathed with Ag; expected melting point of 801°C is consistent with ultrasonic data.

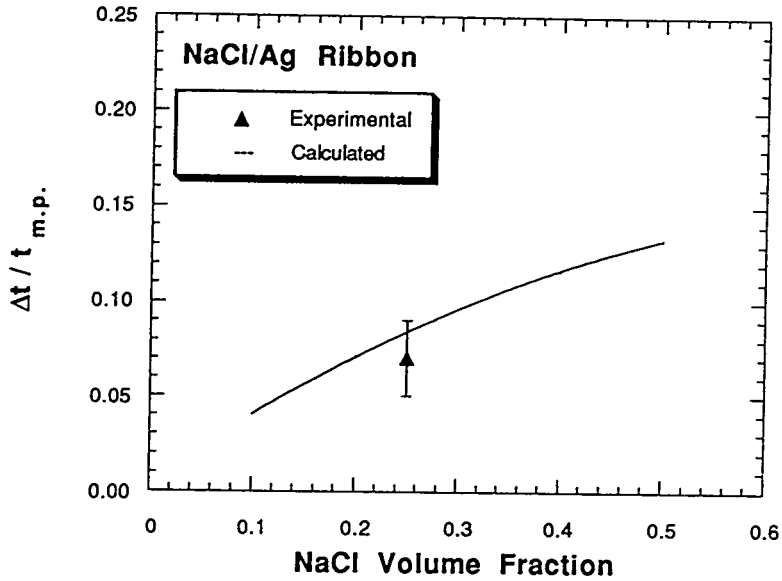

Fig. 39. Change in ultrasonic echo transit time vs. NaCl volume fraction; measured value (triangle) at volume fraction of 0.25 is in agreement with calculated value (line).

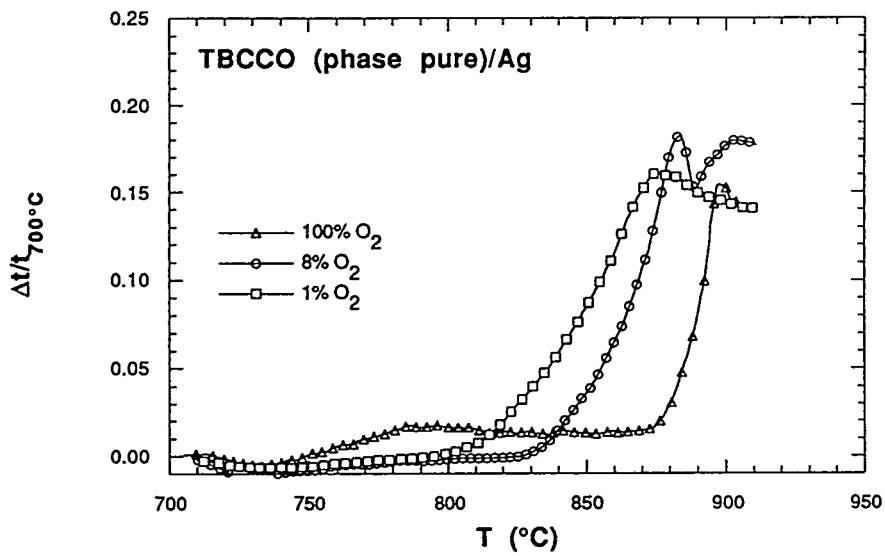

Fig. 40. Change in ultrasonic echo transit time as a function of temperature for three phase-pure Tl-1223/Ag ribbons.

In Fig. 42, the change in ultrasonic echo transit time in air as a function of temperature for Bi-2223/Ag ribbons provided by ASC is shown. Sample #1 is a monofilament, sample #2 is multifilament. Two separate specimens for each sample type were run, with all four specimens showing essentially the same behavior: slight densification before melting, followed by a moderate amount of liquid phase forming at ≈840°C.

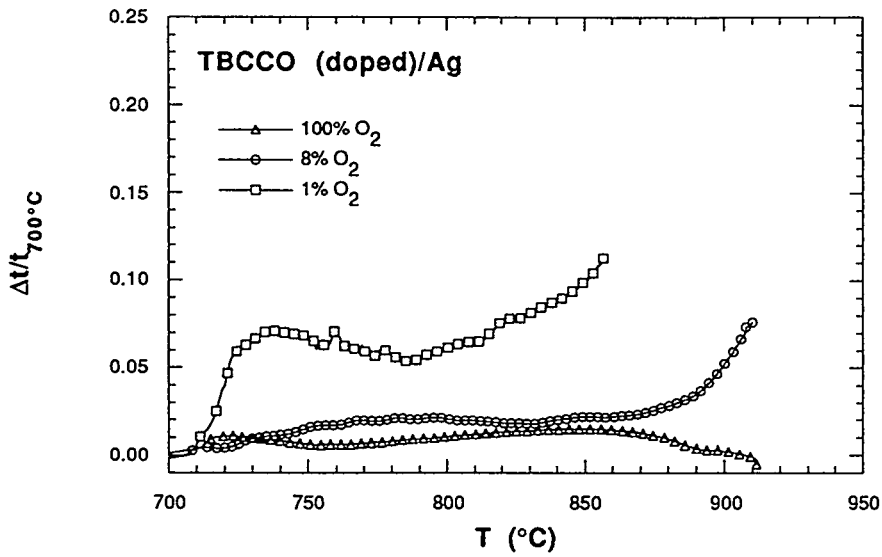

Fig. 41. Change in ultrasonic echo transit time as a function of temperature for three doped Tl-1223/Ag ribbons.

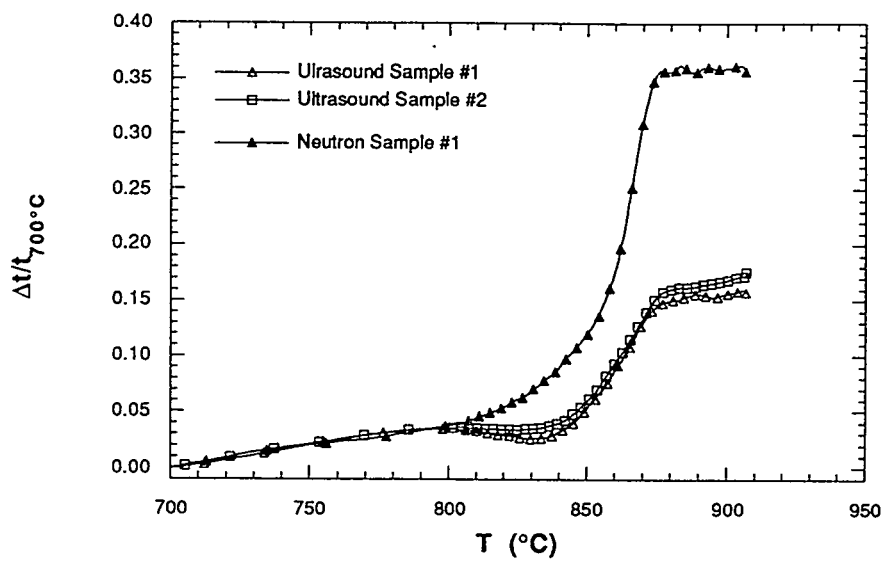

Fig. 42. Change in ultrasonic echo transit time as a function of temperature for Bi-2223/Ag ribbons provided by ASC; sample #1 is monofilament and sample #2 is multifilament.

Residual stress measured by neutron diffraction

Differences in coefficients of thermal expansion of the constituents of a composite lead to residual stresses. The situation for Bi-2223/Ag tapes is particularly complex because of the geometry and anisotropy of the superconductor. The thermal expansion of Ag ranges from 19 to 23 x 10^{-6} °C^{-1}. The thermal expansion coefficient for Bi-2223 is 14-24 x 10^{-6} °C^{-1}, with the greater expansion associated with the c axis (the expansion in the c-axis direction is ≈1.7 times that of the a-axis direction ([Arendt et al., 1992]). It is difficult to predict even the sign of the residual stresses in the Ag or Bi-2223. We have measured by neutron diffraction the average strains in the Ag and BSCCO in various crystallographic

directions. These data provide an experimental answer to the questions regarding magnitude and sign of fabrication-induced residual strain and provide data for validating models that are used to predict residual stresses.

For this experiment, a bundle of tape sections provided by ASC (each section was 100 μm thick and 20 mm long) filled a volume of about 10 mm in diameter and 20 mm high. The diffraction peaks were very sharp. The strains for various directions for the Ag and Bi-2223 are shown in Fig. 43. Ag tapes and Bi-2223 powder were used as references. The Ag strain is clearly tensile (up to 0.1%), whereas strains in the Bi-2223 are predominantly compressive for the c-axis directions and slightly tensile for directions in the a-b plane. The error in strain is ±0.02%. In the future, experiments will be carried out at elevated temperatures to establish the strain-free temperature and to study the formation of liquid phase.

2.5 Applications and Devices

Application research and development are focused on production and testing of components, analysis of performance (Cha et al., 1994a), and design of new systems.

2.5.1 Operation of R & A Superconducting Magnet

The R & A magnet was shipped from LANL to ANL in April 1994, and an all-aluminum stand was built and anchored on the floor of the H-wing high-bay in Building 212. Old vacuum seals were replaced and checked for leaks. The power supply and control systems were checked and became operational in June. Vacuum pumping and N_2 shield cooling were conducted in early August; there were no apparent problems. Shortly after, the magnet was precooled with liquid N_2 to approximately 80 K, followed by liquid-He cooling to 4.2 K. The magnet was then energized gradually to full capacity. The entire operation was successful, and no major problems were encountered, despite the magnet being unused for ≈10 years.

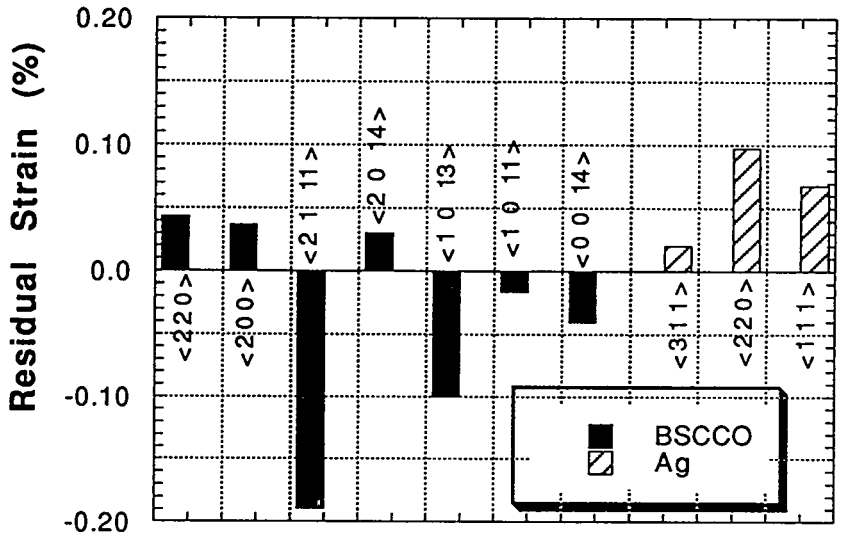

Fig. 43. Residual strains in Bi-2223/Ag monofilament supplied by ASC.

The R & A magnet can produce a maximum magnetic flux density of 2.5 T. It has two coils with a gap of 128 mm. The bore diameter is 356 mm. The size of the bore and the gap makes it feasible to test bulk samples with relatively large dimensions in magnetic fields of interest to most commercial applications. The magnet's power supply system can deliver current up to 500 A DC at very low voltages. Figure 44 shows the variation of magnetic flux density, measured at the geometric center of the magnet, with the current delivered by the power supply (Cha et al., 1993a; Cha 1994).

2.5.2 Measurement Facilities

Current–lead test facility

To aid in evaluating current leads with low heat leakage, a special cryostat with a background heat leak of about 10–15 mW has been developed (Niemann et al., 1993). Accurate pressure control of the cryostat vapor space has been developed and the calorimetry of the cryostat to allow accurate measurements has been examined (Cha et al., 1993b; Cha et al., 1994b). The facility measures leads with currents as high as 125 A and with heat leakage one order of magnitude lower than for conventional copper leads.

The measurement cryostat is all stainless steel and is made of two thin–walled concentric tubes sealed at one end and connected with a Conflat flange at the other end. The outside diameter of the inner tube is 7.62 cm and that of the outer tube is 10.16 cm. Length of the cryostat is approximately 1.22 m. Between the inner and the outer tubes are 35 layers of multilayer insulation (MLI). The inner tube was cold–shocked at liquid–N_2 temperature several times and the entire assembly was then leak–checked, after which the cryostat was filled with liquid He. He boil–off measurements were performed to determine the heat leak rate of the cryostat. Heat leak rates (Fig. 45) were acceptable for the duration of the tests to be conducted for the current leads.

A superconducting magnet capable of generating a uniform 2.5–T magnetic field over about a 10–cm diameter volume is available for lead characterization, along with a 5 kA DC power supply. Capability exists for measuring J_c over the range of temperatures and magnetic fields that most leads will be exposed to.

AC vs. DC tests

An analytical study (Hull, 1993) suggested that a voltage drop of up to 100 μV/cm could be tolerated in an HTS lead without significantly affecting performance. This suggests that the AC hysteresis losses in an HTS lead should not adversely affect performance. Many of the power applications for leads will have a substantial AC component to the current, as expected in the applications with several of our industrial collaborators. Performance of a Bi–2223 sinter–forged HTS lead pair was measured in the Current Lead Test Facility with both AC and DC currents. For currents up to 100 A, an AC current produced at most a 17% increase in the heat leak into the liquid He (Balachandran et al., 1994c).

2.5.3 Current–Lead Performance

Current leads are a near–term application of high–T_c superconductors. All current–lead activities have involved an industrial partner. As this application has matured, involvement has been limited to (1) designs that push the state of the art of materials; (2) assisting small companies that have active programs to commercialize leads but not the resources to have comprehensive materials; and (3) use of unique facilities to characterize

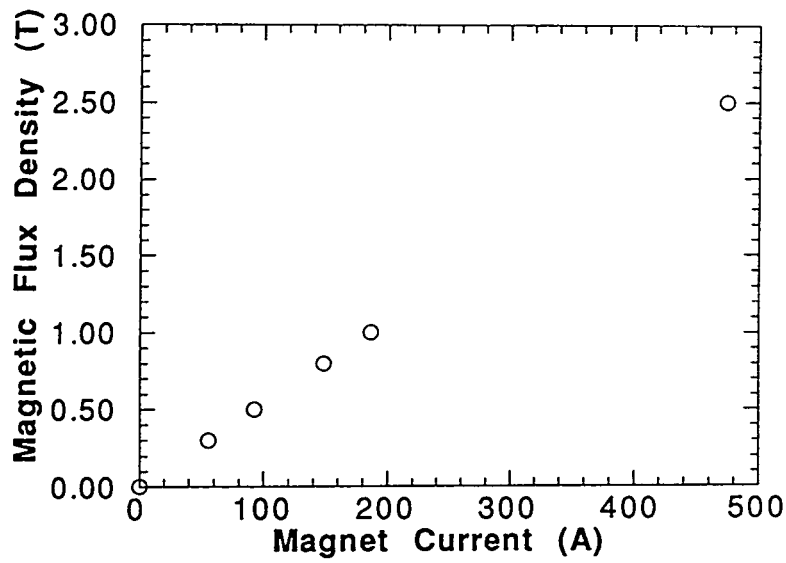

Fig. 44. Variation of magnetic flux density with current at center of R & A magnet.

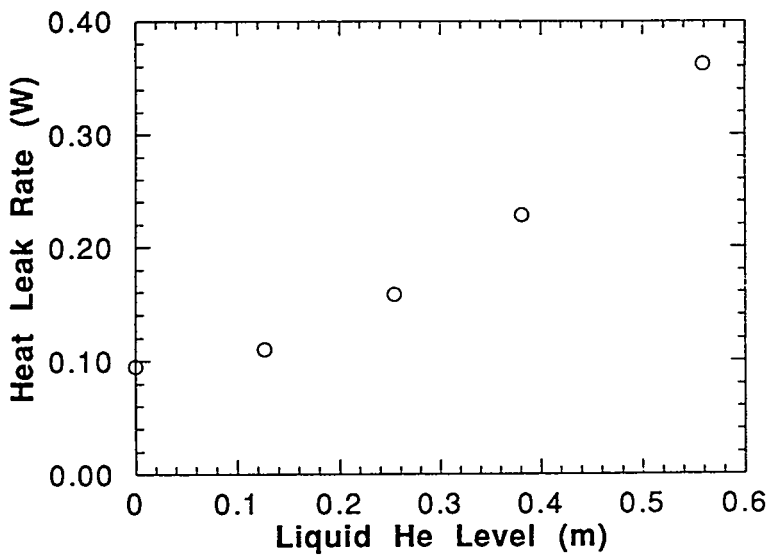

Fig. 45. Heat leak rate as a function of liquid-He level in cryostat.

lead performance so that these facilities need not be duplicated by companies with limited resources. In all collaborations, the preference is to construct leads with commercially available materials.

Zer Res Corporation leads

Two silicon diodes were installed to measure the temperatures at the upper and lower ends of the Zer Res current lead. Voltage taps were soldered in place and two resistive heaters were mounted on the brass caps of the lead for temperature control. A third heater was installed near the bottom of the cryostat in case more boil-off was needed for temperature control. The entire insert included a liquid-He level sensor and a current

return path for the lead. By adjusting the currents through the heaters and the liquid–He level in the cryostat, we obtained the desired temperatures and temperature gradients.

Critical current tests were conducted by pulsing a constant current through the lead. Two types of tests, isothermal and thermal gradient, were performed. Isothermal tests were carried out at 5, 20, and 60 K. Two temperature–gradient tests, 20–60 K and 5-70 K, were conducted. For each test, the lead was subjected to an constant applied field of 0, 260, 520, and 1040 gauss. Data are being analyzed and results will be reported to Zer Res in the near future.

IGC powder–in–tube leads

This work in collaboration with Intermagnetics General Corporation (IGC) was performed substantially during FY 93, but ended in FY 94 with publication of the results (Hull, 1993; Seol and Hull, 1993). Analysis of PIT Bi–2223 leads showed that use of a pure Ag sheath resulted in leads with poor thermal stability. However, use of an Ag–alloy sheath resulted in leads with thermal stability superior to that of a sintered YBCO or Bi–2223 lead without a sheath. Use of an alloy such as Ag/3% Au results in a lead that may achieve low thermal leakage and yet not burn out if the lead undergoes transition to the normal state. In addition, the optimal length of such a lead is convenient for most magnet designs. IGC was able to show that such a lead could be manufactured with reasonable values of J_c in a magnetic field.

Superconductivity, Inc., leads

An ongoing current–lead project is a collaboration with Superconductivity, Inc., for development of a 1500–A lead to be used in a superconducting magnetic energy storage (SMES) system for power quality control. Staff from the company have participated in all stages of the project, especially in assembly and component testing. Technical progress in FY94 consisted of final engineering design, component testing, and lead assembly (Niemann et al., 1994b and 1994c). Features of the lead include demountable HTS components (Niemann et al., 1994a), use of a sintered YBCO/15% Ag conductor rods, and capability for shielding from the magnetic field from SMES magnet fields. A key component in the project has been development of a heat intercept (at the warm end of the HTS component) with very high electrical resistivity but low thermal resistivity (Niemann et al., 1994e). Such intercepts are necessary features for HTS leads if their performance is to be substantially better than that of conventional copper leads (Hull, 1993). Lead performance will be measured in FY 95.

Babcock & Wilcox leads

In a collaborative project with the Babcock and Wilcox Company, a 16–kA HTS lead for use in a 0.5 MWh SMES device is being developed. Features of the design include conduction cooling and use of multiple elements of PIT Bi–2223 with a Ag/3% Au sheath embedded in a stainless steel safety lead (Niemann et al., 1994d). Work in FY94 included design of the lead and evaluation of vendor–supplied HTS elements. Staff from the company are involved in all stages of the development, including construction of the lead.

In FY 95, test of a completed HTS lead pair under the anticipated operational conditions of the magnet will be conducted.

2.5.4 Superconducting Magnetic Bearings

The collaborative effort continues with Commonwealth Research Corporation (CRC) to develop superconducting magnetic bearings for flywheel energy storage (FES) applications. Electrical energy storage on a utility scale is currently not practicable for most utilities because of the requirements for special geography and the inefficiencies of existing storage systems (Abboud et al., 1994). A potential solution to this problem is FES with very low rotational losses made possible through high-T_c superconducting magnetic bearings.

High-speed flywheels incorporating HTS bearings and inertial rims made from high-strength composite materials, combined with new-technology motor/generators, offer potential for very high (>90%) diurnal storage efficiencies. Such high efficiencies cannot be achieved by FES systems that use conventional bearing technologies, including active magnetic bearings. Flywheel-stored energy is lost due to friction with conventional bearings at rates of ≈1%/hr, but HTS magnetic bearings should result in idle losses of only 0.1%/hr.

Significant advances were made during FY 94 in development of materials and components for very-low-friction HTS magnetic bearings, and in establishment of a design data base through laboratory scale-up and spin-down tests. Major accomplishments included: significant enhancements in ANL's capabilities for processing bulk YBCO materials, establishment of a new record-low coefficient of friction of 3×10^{-7}, completion of the FES Test Apparatus (FTA) for magnetic bearing/flywheel rotor scale-up studies, and successful testing of a 12 kg flywheel rotor levitated over an array of HTS elements.

Task elements for FY 94 included:

- Development of HTS materials with improved levitation characteristics, and processing of large quantities of YBCO stator elements for magnetic-bearing experiments.
- Development and fabrication of improved permanent magnet (PM) materials for use in flywheel rotor/HTS bearing applications.
- Integration of HTS magnetic bearing components with high-strength graphite composite rims for laboratory FES tests.
- Establishment of a data base for HTS magnetic bearing design through a series of bell-jar experiments to delineate loss mechanisms.
- Fabrication and instrumentation of a large FTA vacuum chamber for testing prototype FES rotors.
- Performance of FTA spindown experiments with flywheel rotors to verify HTS bearing scaleup characteristics.
- Assessment of design alternatives for high-efficiency FES power input/output (I/O) with the utility grid.

The HTS materials effort included procurement of two new high-temperature furnaces by CRC for ANL's use in processing of bulk YBCO stator elements. Levitation characteristics of YBCO stator elements were improved during the year through use of Sm-123 and Nd-123 single-crystal seeds for improved HTS crystal structure, enhanced melt-processing techniques, and other innovations. The levitation characteristics of each HTS puck or tile were determined through force measurements by a standard reference magnet.

The collaborative efforts with UGIMAG (Valparaiso, IN) continued in development of high-strength permanent magnet (PM) rotors. The impact of azimuthal inhomogeneities and other characteristics of rare-earth PMs on rotor performance was assessed. A large number of 8.9-cm-outer-diameter NdFeB ring magnets were fabricated and delivered to ANL for characterization and use in magnetic-bearing experiments. A large NdFeB magnet assembly, designed by ANL and fabricated by UGIMAG, was used in the initial FTA tests.

A suitable high-speed flywheel requires integration of an inertial rim (a high-strength composite rotor to store the rotational kinetic energy), the superconducting bearing, and the power I/O components. Most designs for a superconducting bearing include an HTS stator composed of HTS elements enclosed in a liquid-N_2 canister, and a PM rotor, which must be attached to the inertial rim by an appropriate hub. A graphite fiber/epoxy composite rim was filament-wound, and a flywheel hub was fabricated. Work on integration of power I/O components has begun.

HTS bearing bell-jar experiments were continued in order to further delineate potential loss mechanisms in the HTS stator and PM rotor components. The bell jar is about 27 cm in diameter and contains a liquid-N_2 cryogenic chamber within the vacuum. One or more HTS elements can be placed either inside or on top of the liquid-N_2 chamber. This apparatus has been used to measure spin-down of flywheel rotors levitated above HTS stator arrays. Rotation rate is measured with a tachometer, and flywheel position is determined by a traveling telescope. Spin-up has been accomplished with both a gas jet and an induction motor.

Figure 46 shows rotation rate as a function of time for one of the experiments with a small disk magnet (19 mm diameter, 6.4 mm height, and 11.3 g mass) levitated over a single HTS element. To shorten the time required for the experiment, the magnet was slowed at intervals either by letting dry N_2 into the chamber or by introducing mechanical friction against the spinning rotor. These actions are responsible for the sharp decreases in rotation rate shown in Fig. 46, (e.g., at 7500 and 10,000 s). The coefficient of friction can be calculated directly from the rotor spin-down data by use of appropriate formulas (e.g., Hull et al., 1994). PM rotors that contain an NdFeB ring (88 mm outer diameter, 64 mm inner diameter, and 13 mm height) have also been used in bell-jar spin-down experiments. Ring-magnet rotor tests have been performed at various levitation heights and for various HTS element array configurations. Coefficients of friction of $\mu < 3 \times 10^{-7}$ were achieved in some tests.

Construction of the large FTA vacuum test chamber was completed and tests were initiated with flywheel rotors in the 2-15 kg range. The FTA test chamber is a cylindrical stainless steel vessel (inner diameter of 914 mm and height of 864 mm) with appropriate viewports and instrument feedthroughs. A liquid-N_2 cryochamber housing the HTS bearing stator elements is contained within the FTA vacuum chamber. The FTA includes a 1000 L/s turbomolecular vacuum pump and two rotary vacuum pumps. These pumps can create a vacuum of $<10^{-4}$ Pa when the cryogenic chamber is cold. A schematic diagram of the FTA chamber has been published (Poeppel et al., 1993). A 2.5 kg rotor was used in initial FTA magnetic bearing tests; this rotor consisted of a PM structure with a plastic turbine mounted on top, as shown in Fig. 47: the rotor is shown being held in place with a positioning device over the FTA cryochamber prior to levitation and spin testing. Levitation characteristics and friction results for this bearing are being evaluated.

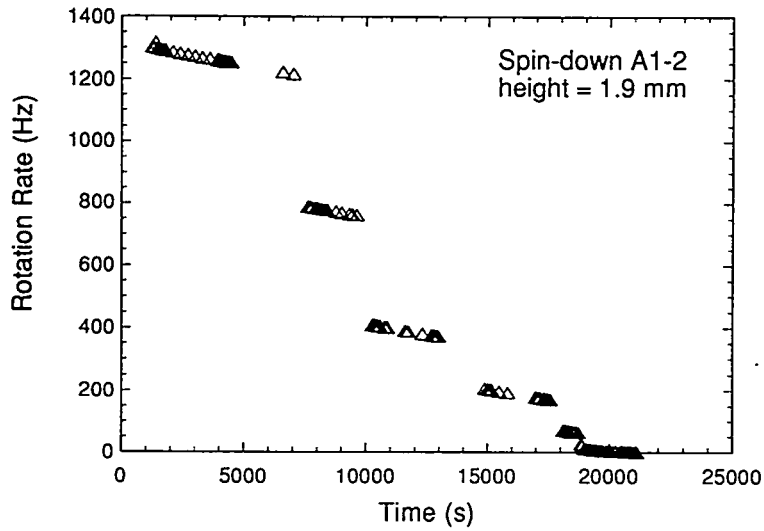

Fig. 46 Rotational rate vs. time for vacuum spin-down of 11.3 g permanent magnet disk rotor.

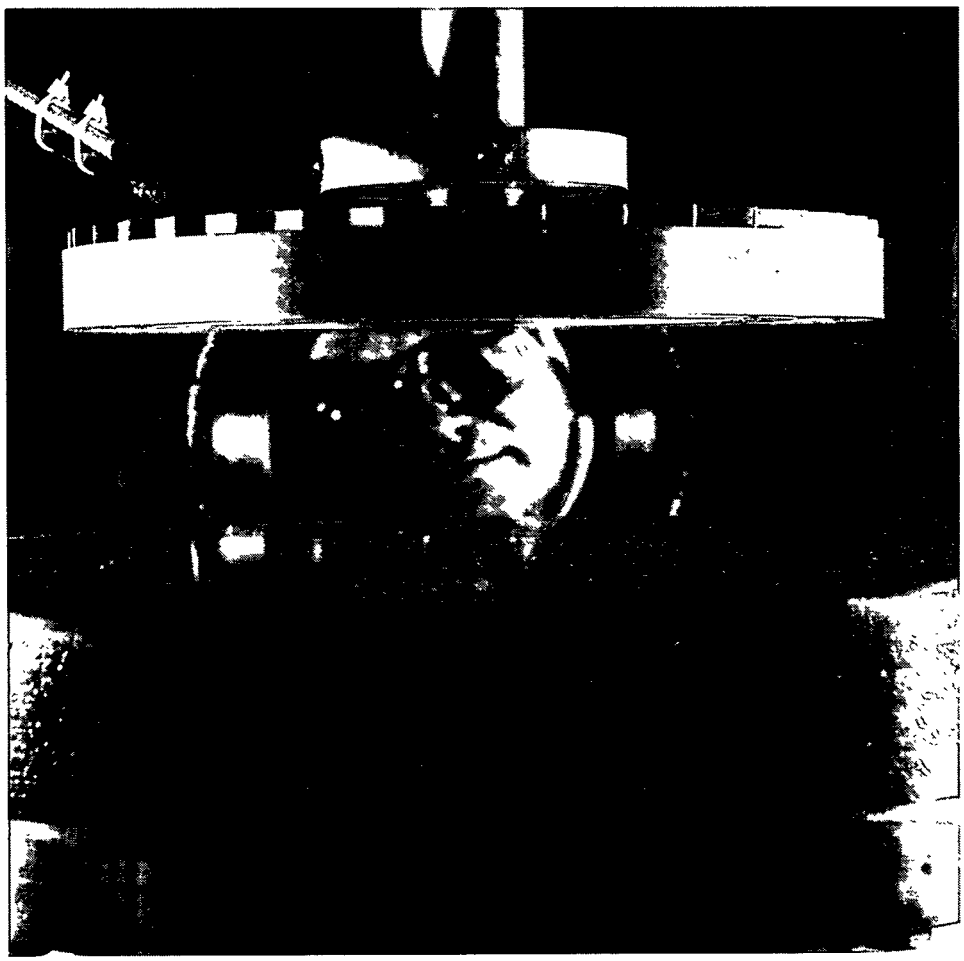

Fig. 47. Magnet and cryochamber used in large FTA vacuum chamber.

2.6 Fundamental Studies

2.6.1 Evaluation of Weak Links

Although we sometimes find correlations between gross microstructure and J_c, wide variation of important length scales (sample or grain sizes of 10–100 μm to grain-boundary widths 1–10 nm) makes definitive work almost impossible. One popular way to evaluate weak-link behavior is to study the field dependence of J_c, and we have measured this in most of our PIT and deposited samples. Features of these data are consistent with expectations for weak links, but our research has indicated that the use of a single parameter, J_c, may be inadequate to describe polycrystalline materials. We showed (Hettinger et al., 1993 and 1994) that such a J_c can be extracted by fitting current-voltage, I(V), measurements to a thermally activated flux-flow model in that absence of weak links; and the Ambegaokar-Halperin Josephson-junction model for artificial grain boundaries (in collaboration with Westinghouse and TRW). We have also demonstrated that one can distinguish between flux depinning and weak links by comparing I(V) data on polycrystalline and epitaxial deposits of Tl-1223.

Electric field, E, as a function of current density, J, has been studied in both epitaxial and polycrystalline $Tl_2Ba_2CaCu_2O_x$ (Tl-2212) thin films, and the importance of high-angle-grain boundaries (HAGB) in limiting J_c has been investigated. At low magnetic fields, J_c in the polycrystalline materials studied is severely reduced. However, as the magnetic field is increased, J_c of the polycrystalline material parallels that of the epitaxial grain-boundary-free material, suggesting that vortex motion is the limiting factor. However, measurements of the full E–J characteristic in polycrystalline materials indicate that there is a signature of the grain-boundary dissipation, even at large magnetic fields where vortex motion may limit J_c at a single critical criterion (Fig. 48a). Notice in this figure that J_c is very dependent upon the critical criterion used. For example, if an application requires a dissipation of less than 10^{-6} V/cm at 2 T, then the two materials would perform very similarly. However, if the application required 10^{-5} V/cm at this field, we see a factor of 2.5 difference in J_c. Figure 48a demonstrates the importance of measuring the full E–J characteristic rather than reporting a single J_c at a specific criterion.

2.6.2 Vortex Motion

It is clear that under some conditions vortex motion is important in polycrystalline materials and that it almost always limits the current-carrying performance of grain-boundary-free materials. To learn more about vortex motion and how to control it, columnar-nonsuperconducting tracks have been formed in several superconducting materials by bombardment with ≈650 MeV Xe ions at ANL's ATLAS heavy-ion accelerator. This work was performed in collaboration with GE, Superconductor Technologies Inc., and Westinghouse. Ions of this energy are expected to create continuous tracks through a material of the compositions under investigation to ≈25 μm. The material we have studied most completely is thin-film Tl-2212. Because these samples are typically 0.8 μm thick, every ion passes through the material. The average track diameter is 100 Å, which is nearly an ideal size for optimal pinning efficiency. As may be observed in Fig. 48b, J_c is improved at 1 T by four orders of magnitude. Other surprising conclusions that can be drawn from this work are (1) orientation of the defect with respect to the magnetic field is important even when the two-dimensional vortices are nearly decoupled from those in adjacent Cu-O bi-layers, and (2) vortex/vortex interactions are inadequate to pin several vortices by a single defect.

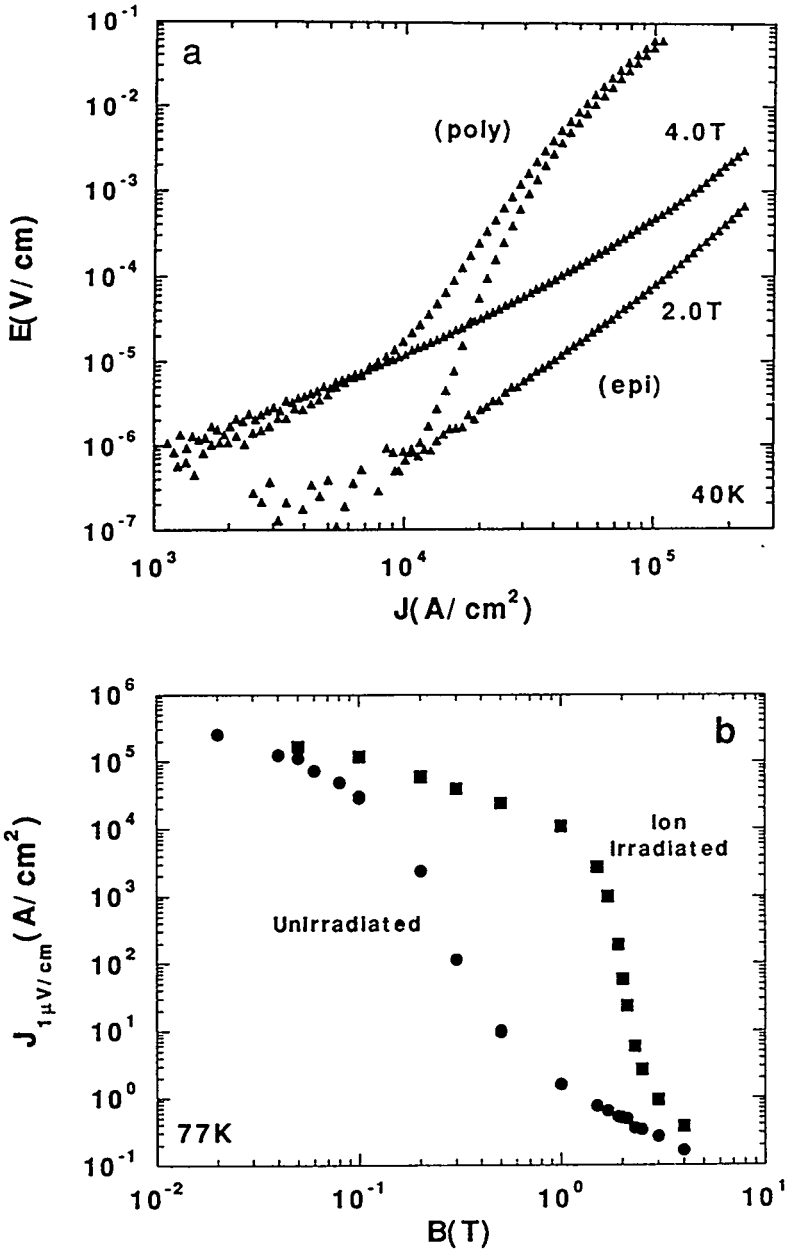

Fig. 48. Plots of (a) electric field vs. critical current density for Tl-2212 films and (b) J_c vs. field for Tl-2212 films.

Because the polycrystalline data cannot be fit to a single parameter, J_c, for any existing model, we feel that to make further progress, I(V) data must be used. Therefore, at the recent Wire Development Workshop (St. Petersburg, FL, February 1994), we made a proposal to "Develop Standardization of Measurement Procedures and Interpretation for Critical Currents" and invited industries and other laboratories to take part by sending us examples of I(V) data for their best samples. This proposal was made in conjunction with M. P. Maley of LANL.

2.7 Additional Interactions

Our studies in collaboration with Radiation Monitoring Devices, Inc. (RMD) have focused on obtaining stoichiometry control during metal/organic chemical spray pyrolysis (MOCSP). By making adjustments to the metal atom stoichiometry in the spray solution, RMD has achieved Bi–Pb–Sr–Ca–Cu atom ratios in the as-sprayed powder that are within the desired limits for producing high-phase-purity Bi-2223 in a sheath. Analytical measurements made at ANL have shown that cation loss during spraying, primarily Pb, is related in a predictable way to the spray-solution composition. A series of Bi-2223/Ag mono- and bifilaments prepared by RMD had a nominal composition of $Bi_{1.8}Pb_{0.4}Sr_{2.1}Ca_{2.2}Cu_{3.1}O_x$, with metal atom unit deviations of ± 0.1. SEM examinations performed on these specimens reveal considerably improved microstructures when compared to prior MOCSP specimens. The cores were densely packed, fairly uniform in thickness (≈50 μm), and well-bonded to the Ag sheath. There are still large numbers of second-phase particles in the 10-to 20-μm range that are mostly $(Ca,Sr)_2CuO_3$. Heat-treatment conditions for MOCSP composites are being optimized.

The collaboration between Superconducting Products Company (SPC) and ANL continues to involve fabrication of Ag-clad wires. A process for continuous forming of tapes from Ag plate or sheet has been developed and a U.S. patent has been applied for.

We continue to work with SSC, Inc. (Bothell, WA) on powder synthesis. SSC precursor powders have proved to be highly successful for Bi-2223 and Tl-1223.

In collaboration with Midwest Superconductivity, Inc., we obtained the first strength and K_{IC} data for bulk Tl-based superconductors. For ≈85% dense Tl-2223, the strength was 101 MPa and the K_{IC} was 1.2 MPa√m. These values are very close to those of YBCO for specimens of similar density.

Containerless melting of YBCO studies with Containerless Research, Inc., have revealed that the homogeneity of melts at temperatures greater than 1300°C is greatly improved in low-pO_2 atmospheres (Weber et al., 1993 and 1994). Such atmospheres can also be used for melt-processing Bi-2212 (Miller et al., 1993a).

University collaborations over the past year include continued interaction with the University of Wisconsin at Madison and the State University of New York at Buffalo on production of Ag-clad tapes; high-resolution electron microscopy studies with Prof. V. Dravid of Northwestern University, primarily on grain boundaries; production of textured conductors with Prof. J. A. Lewis of the University of Illinois at Urbana-Champaign and Prof. J. Schwartz of Florida State University; texture analysis of bulk materials with Prof. J. S. Kallend of the Illinois Institute of Technology; creep testing of superconductors with Profs. A. Domínguez-Rodríguez and A. R. de Arellano-López of the University of Seville; synthesis of Tl-based superconductors with Prof. Z. Z. Sheng of the University of Arkansas at Fayetteville; and shock-compaction studies of high-T_c superconductors with Iowa State University/Lawrence Livermore National Laboratory and the New Mexico Institute of Technology.

References

R. G. Abboud, J. R. Hull, K. L. Uherka, and T. M. Mulcahy, Proc. Am. Power Conf. **56-II**, 1356 (1994).

R. H. Arendt, M. F. Garbauskas, C. A. Meyer, F. J. Rotella, J. D. Jorgensen, and R. L. Hitterman, Physica C **194**, 397 (1992).

U. Balachandran, R. B. Poeppel, J. E. Emerson, and S. A. Johnson, U.S. Patent 5,086,034 (Feb. 4, 1992).

U. Balachandran, A. N. Iyer, P. Haldar, and L. R. Motowidlo, J. Met. **45**, 54 (1993a).

U. Balachandran, W. Zhong, C. A. Youngdahl, and R. B. Poeppel, J. Electron. Mater. **22**, 1285 (1993b).

U. Balachandran, A. N. Iyer, P. Haldar, J. G. Hoehn Jr., L. R. Motowidlo, and G. Galinski, Appl. Supercond. **2**, 251 (1994a).

U. Balachandran, A. N. Iyer, C. A. Youngdahl, L. R. Motowidlo, and P. Haldar, Adv. Cryo. Eng. **40A**, 289 (1994b).

U. Balachandran, C. A. Youngdahl, M. T. Lanagan, S. E. Dorris, J. J. Picciolo, J. Cluff, T. Brent, M. Marinelli, B. Fisher, P. Winandy, J. Wenzlaff, T. Askew, R. Niemann, and R. B. Poeppel, to be presented at 7th Intl. Symp. on Superconductivity, ISS'94, Fukuoka, Japan (Nov. 1994c).

A. C. Biondo, M. T. Lanagan, K. C. Goretta, J. Hu, D. J. Miller, C.-T. Wu, C. A. Youngdahl, and R. B. Poeppel, Adv. Cryo. Eng. **40A**, 229 (1994).

M. Cankurtaran, G. A. Saunders, and K. C. Goretta, Supercond. Sci. Technol. **7**, 4 (1994).

Y. S. Cha, J. R. Hull, and R. C. Niemann, Paper No. 93-WA/AES-2, Presented at 1993 ASME Winter Annual Meeting, New Orleans, Nov. 1993a.

Y. S. Cha, R. C. Niemann, and J. R. Hull, Cryogenics **33**, 675 (1993b).

Y. S. Cha, Cryogenics, in press (1994).

Y. S. Cha, M. T. Lanagan, K. E. Gray, V. Z. Jankus, and Y. Fang, Appl. Supercond. **2**, 47 (1994a).

Y. S. Cha, R. C. Niemann, and J. R. Hull, Cryogenics **34**, 99, (1994b).

N. Chen, A. C. Biondo, S. E. Dorris, K. C. Goretta, M. T. Lanagan, C. A. Youngdahl, and R. B. Poeppel, Supercond. Sci. Technol. **6**, 674 (1993a).

Z. Y. Chen, Z. Z. Sheng, Y. Q. Tang, Y. F. Li, D. O. Pederson, K. Goretta, P. Kostic, and D. Shi, Physica C **212**, 206 (1993b).

A. H. Cottrell, The Mechanical Properties of Matter (John Wiley and Sons, New York, 1964).

J. T. Dawley, S. E. Dorris, M. T. Lanagan, E. P. Kvam, and R. B. Poeppel, Supercond. Sci. Technol. **7**, 587 (1994).

A. R. De Arellano-López, K. C. Goretta, J. L. Routbort, D. J. Miller, and A. Domínguez-Rodríguez, Ceramica Acta **3**, 5 (1991).

J. A. DeLuca, P. L. Karas, J. E. Tkaczyk, C. L. Briant, M. F. Garbauskas, and P. J. Bednarczyk, Mater. Res. Soc. Symp. Proc. **275**, 669 (1992).

A. Domínguez-Rodríguez, M. Jiménez-Melendo, Nan Chen, K. C. Goretta, S. J. Rothman, and J. L. Routbort, J. Phys. III France **4**, 253 (1994).

S. E. Dorris, B. C. Prorok, M. T. Lanagan, S. Sinha, and R. B. Poeppel, Physica C **212**, 66 (1993).

S. E. Dorris, B. C. Prorok, M. T. Lanagan, N. M. Browning, M. R. Hagen, J. A. Parrell, Y. Feng, A. Umezawa, and D. C. Larbalestier, Physica C **223**, 163 (1994).

Y. Fang, S. Danyluk, M. T. Lanagan, and K. C. Goretta, J. Mater. Sci. Lett. **13**, 852 (1994).

C. Fanggao, P. J. Ford, G. A. Saunders, L. Jiaquing, D. P. Almond, B. Chapman, M. Cankurtaran, R. B. Poeppel, and K. C. Goretta, Supercond. Sci. Technol. **6**, 484 (1993).

Y. Feng, Y. E. High, D. C. Larbalestier, Y. S. Sung, and E. E. Hellstrom, Appl. Phys. Lett. **62**, 1553 (1993).

R. Flükiger, A. Jeremie, B. Hensel, E. W. Seibt, J.Q. Xu, and Y. Yamada, Adv. Cryo. Eng. **38**, 1073 (1992).

K. C. Goretta, C.-T. Wu, M. T. Lanagan, R. B. Poeppel, J. Schwartz, and S. Wu, J. Electron. Mater. **22**, 1289 (1993).

K. C. Goretta, J. A. Cluff, M. A. Boling-Risser, and J. L. Routbort, Scripta Metall. Mater. **31**, 641 (1994a).

K. C. Goretta, L. J. Martin, D. Singh, R. B. Poeppel, N. Chen, C.-Y. Chu, and J. L. Routbort, Adv. Cryo. Eng. **40A**, 63 (1994b).

K. C. Goretta, E. J. Zamirowski, J. M. Calderoñ-Moreno, D. J. Miller, N. Chen, T. G. Holesinger, and J. L. Routbort, J. Mater. Res. **9**, 541 (1994c).

K. E. Gray, J. D. Hettinger, and D. H. Kim, in "Superconducting Superlattices and Multilayers," ed. I. Bozovic (SPIE, New York, 1994) in press.

J. Guo, J. Schwartz, Y. S. Cha, C.-T. Wu, and K. C. Goretta, Adv. Cryo. Eng. **40A**, 169 (1994a).

J. Guo, J. Schwartz, C.-T. Wu, and K. C. Goretta, IEEE Trans. Magn. **30**, 2098 (1994b).

P. Haldar, J. G. Hoehn Jr., L. R. Motowidlo, U. Balachandran, and Y. Iwasa, Adv. Cryo. Eng. **40A**, 313 (1994).

J. D. Hettinger, D. H. Kim, D. J. Miller, J. G. Hu, K. E. Gray, J. E. Sharping, K. Daly, C. Pettiette-Hall, J. E. Tkaczyk, and J. Deluca, IEEE Trans. Appl. Supercond. **3**, 1211 (1993).

J. D. Hettinger, D. J. Miller, K. E. Gray, D. H. Kim, J. Deluca, P. Karas, J. E. Tkaczyk, and M. Eddy, unpublished information (1994).

W. L. Holstein, J. Phys. Chem. **97**, 4224 (1993).

J. R. Hull, IEEE Trans. Appl. Supercond. **3**, 869 (1993).

J. R. Hull, T. M. Mulcahy, K. L. Uherka, R. A. Erck, and R. G. Abboud, Appl. Supercond. Conf., Boston, Oct. 16, 1994.

J. Joo, J. P. Singh, and R. B. Poeppel, Supercond. Sci. Technol. **6**, 421 (1993).

D. H. Kim, K. E. Gray, R. T. Kampwirth, J. C. Smith, D. S. Richeson, T. J. Marks, J. H. Kang, J. Talvacchio, and M. Eddy, Physica C **177**, 431 (1991).

Y. F. Li, Z. Z. Sheng, S. Sengupta, K. C. Goretta, and P. E. D. Morgan, Physica C, in press (1994).

J. S. Luo, N. Merchant, V. A. Maroni, D. M. Gruen, B. S. Tani, W. L. Carter, and G. N. Riley, Jr., Appl. Supercond. **1**, 101 (1993).

P. Majewski, B. Hettich, K. Schulze, and G. Petzow, Adv. Mater. **3**, 488 (1991).

P. Majewski, S. Kaesche, H–L. Su, and F. Aldinger, Physica C **221**, 295 (1994).

L. J. Martin, K. C. Goretta, J. Joo, J. P. Singh, S. R. Olson, S. Wasylenko, R. B. Poeppel, and N. Chen, Mater. Lett. **17**, 232 (1993).

D. J. Miller, T. G. Holesinger, J. L. Routbort, K. C. Goretta, and L. S. Chumbley, J. Electron. Mater. **22**, 1263 (1993a).

D. J. Miller, J. G. Hu, J. D. Hettinger, K. E. Gray, J. E. Tkaczyk, J. DeLuca, P.L. Karas, and M.F. Garbauskas, Appl. Phys. Lett. **63**, 556 (1993b).

T. A. Miller, J. E. Ostenson, Q. Li, L. A. Schwartzkopf, D. K. Finnemore, J. Righi, R. A. Gleixner, and D. Zeigler, Appl. Phys. Lett. **58**, 2159 (1991).

R. C. Niemann, Y. S. Cha, and J. R. Hull, IEEE Trans. Appl. Supercond. **3**, 392 (1993).

R. C. Niemann, Y. S. Cha, J. R. Hull, W. E. Buckles, and M. A. Daugherty, Adv. Cryo. Eng. **39B**, 1153 (1994a).

R. C. Niemann, Y. S. Cha, J. R. Hull, W. E. Buckles, M. L. Daugherty, and B. R. Weber, IEEE Trans. Magn. **30**, 2589 (1994b).

R. C. Niemann, Y. S. Cha, J. R. Hull, W. E. Buckles, and B. R. Weber, Appl. Supercond. Conf., Boston, MA, Oct. 1994c.

R. C. Niemann, Y. S. Cha, J. R. Hull, S. F. Kral, and C. M. Rey, Appl. Supercond. Conf., Boston, MA, Oct. 1994d.

R. C. Niemann, J. D. Gonczy, and T. H. Nicol, Adv. Cryo. Eng. **39B**, 1665 (1994e).

K. Osamura, S. Sato, W. Zhang, and T. Kizu, Physica C **185–189**, 589 (1991).

R. B. Poeppel, et al., Practical Superconductor Development for Electrical Power Applications: Annual Report for FY 1993, Argonne National Laboratory Report ANL–93/33, 1993.

Z. F. Ren and J. H. Wang, Physica C **216**, 199 (1993).

Z. F. Ren, J. H. Wang, D. J. Miller, and K. C. Goretta, Physica C **229**, 137 (1994).

J. L. Routbort, D. J. Miller, E. J. Zamirowski, and K. C. Goretta, Supercond. Sci. Technol. **6**, 337 (1993).

J. L. Routbort, D. J. Miller, M. A. Boling–Risser, J. A. Dunlap, and K. C. Goretta, Scripta Metall. Mater. **30**, 1241 (1994).

J. Schwartz, J. K. Heuer, K. C. Goretta, R. B. Poeppel, J. Guo, and G. W. Raban Jr., Appl. Supercond. **2**, 271 (1994).

E. W. Seibt, A. Jeremie, and R. Flükiger, Thin Sol. Films **228**, 196 (1993).

S. Sengupta, Donglu Shi, J. S. Luo, V. R. Todt, Z. Wang, C. Varanasi, P. J. McGinn, U. Balachandran, and K. C. Goretta, Adv. Cryo. Eng. **40A**, 87 (1994).

S. Y. Seol and Y. S. Cha, Appl. Supercond. **2**, 7 (1994).

S. Y. Seol and J. R. Hull, Cryogenics **33**, 966 (1993).

J. P. Singh, J. Joo, D. Singh, T. Warzynski, and R. B. Poeppel, J. Mater. Res. **8**, 1226 (1993a).

J. P. Singh, J. Joo, N. Vasanthamohan, and R. B. Poeppel, J. Mater. Res. **8**, 2458 (1993b).

V. R. Todt, S. Sengupta, and D. J. Miller, Appl. Supercond., in press (1995).

V. R. Todt, S. Sengupta, D. Shi, P. R. Sahm, P. J. McGinn, R. B. Poeppel, and J. R. Hull, J. Electron. Mater., in press (1994).

J. L. Wagner, P. G. Radaelli, D. G. Hinks, J. D. Jorgensen, J. F. Mitchell, B. Dabrowski, G. S. Knapp, and M. A. Beno, Physica C **210**, 447 (1993).

J. R. K. Weber, D. R. Merkley, W. P. Zima, P. C. Nordine, K. C. Goretta, and R. B. Poeppel, in "Containerless Processing: Techniques and Applications," ed. W. Hofmeister (The Metallurgical Society, Warrendale, PA, 1993) p. 123.

J. K. R. Weber, P. C. Nordine, K. C. Goretta, and R. B. Poeppel, J. Mater. Res. **9**, 1657 (1994).

C.-T. Wu, K. C. Goretta, M. T. Lanagan, A. C. Biondo, and R. B. Poeppel, in "Long Lengths of High-Temperature Superconductor Wires and Tapes," eds. U. Balachandran, E. W. Collings, and A. Goyal (The Metallurgical Society, Warrendale, PA, 1994) p. 101.

Distribution for ANL-94/39

Internal:

T. Askew
U. Balachandran (10)
I. D. Bloom
Y. S. Cha
N. Chen
G. Crabtree
D. R. Diercks
S. E. Dorris
H. Drucker
B. Dunlap
J. T. Dusek
W. A. Ellingson
J. E. Emerson
F. Y. Fradin
R. Giese
K. C. Goretta
K. E. Gray
D. Gruen
M. Hanley
M. Hash
J. Hettinger
J. Hu
J. R. Hull
J. Jorgensen
R. T. Kampwirth
M. Kirk
D. S. Kupperman
S. Lake
M. T. Lanagan
C. A. Malefyt
M. Marinelli
V. A. Maroni
R. L. McDaniel
D. J. Miller
T. Mulcahy
R. C. Niemann
J. J. Picciolo
R. B. Poeppel
A. C. Raptis
J. L. Routbort
W. J. Shack
T. P. Sheahen
J. P. Singh
C. E. Till
K. L. Uherka
A. Wagh
A Wantroba
R. W. Weeks
A. M. Wolsky
C. A. Youngdahl
TIS Files

External:

DOE-OSTI, for distribution per UC-1394 (154)
ANL Libraries
ANL-E (2)
ANL-W

Chicago Field Office, DOE:
Manager
F. Herbaty

U.S. Department of Energy, Washington:

Office of Advanced Utility Concepts, Conservation and Renewable Energy:
J. Daley
R. Eaton III
M. Gunn
Basic Energy Sciences-Materials Science, Energy Research:
I. L. Thomas

Energy Technology Division Review Committee:
H. K. Birnbaum, University of Illinois at Urbana-Champaign, Urbana
R. C. Buchanan, University of Cincinnati, Cincinnati, OH
M. S. Dresselhaus, Massachusetts Institute of Technology, Cambridge, MA
B. G. Jones, University of Illinois at Urbana-Champaign, Urbana
C.-Y. Li, Cornell University, Ithaca, NY
S.-N. Liu, Fremont, CA
R. E. Smith, SciTech, Inc., Morrisville, NC

Other – Industry – University

R. G. Abboud, Commonwealth Edison, Zion, IL
J. Badin, Energetics, Inc., Columbia, MD
A. L. Bement, Jr., Midwest Superconductivity Consortium, Purdue University
T. Bickel, Sandia National Laboratories
K. Blohowiak, Boeing Corporation, Seattle, WA
R. W. Boom, University of Wisconsin – Madison
J. Bray, General Electric Company, Schenectady, NY
W. Buckles, Superconductivity, Inc., Madison, WI
D. Burlone, BASF Corp., Enka, NC
L. Capuano, Conductus, Sunnyvale, CA
R. Cass, HiTc Superconco, Inc., Lambertville, NJ
D. L. Chung, State University of New York – Buffalo
J. Clem, Ames Laboratory
B. Currie, Pacific Northwest Laboratory
S. Danyluk, Georgia Institute of Technology
M. DeGuire, Case Western Reserve University
L. P. de Rochemont, Radiation Monitoring Devices, Inc., Watertown, MA
D. Divecha, Naval Surface Warfare Center, Silver Spring, MD
B. Dorothy, DuPont, Wilmington, DE
M. Eddy, Superconductor Technologies, Inc., Santa Barbara, CA
N. Eror, University of Pittsburgh
D. K. Finnemore, Ames Laboratory
M. Fluss, Lawrence Livermore National Laboratory
S. Foner, Francis Bitter National Magnet Lab., Massachusetts Institute of Technology
J. R. Gaines, Jr., Superconductive Components, Inc., Columbus, OH
C. Gallo, Superconix, St. Paul, MN
T. Grudkowski, United Technologies Research Center, East Hartford, CT
D. Gubser, Naval Research Laboratory
P. Haldar, Intermagnetics General Corp., Latham, NY
S. D. Harkness, Westinghouse, Pittsburgh, PA
R. A. Hawsey, Oak Ridge National Laboratory
J. Hodge, Illinois Superconductor Corp., Evanston, IL
D. L. Johnson, Northwestern University
J. B. Ketterson, Northwestern University
J. L. Kirtley, Jr., Massachusetts Institute of Technology
M. Klein, University of Illinois at Urbana–Champaign
S. F. Kral, Babcock and Wilcox, Lynchburg, VA
D. K. Kroeger, Oak Ridge National Laboratory
H. Kroger, Microelectronics and Computer Technology Corporation, Austin, TX
D. C. Larbalestier, University of Wisconsin – Madison
A. Lauder, DuPont, Wilmington, DE
E. Leung, General Dynamics, San Diego, CA
M. Levy, University of Wisconsin – Milwaukee
J. Lewis, University of Illinois at Urbana–Champaign
D. H. Liebenberg, Office of Naval Research, Arlington, VA
P. Lindhorst, MagneTek, St. Louis, MO
R. Loehman, Sandia National Laboratories
J. Loncoski, Virginia Power, Glen Allen, VA
H. Madler, J. C. Petlau, Inc., Wheeling, IL
D. Madura, General Dynamics, San Diego, CA
A. Malozemoff, American Superconductor Corp., Westborough, MA
C. Martin, SSC, Inc., Woodinville, WA

A. Marwick, IBM, Yorktown Heights, NY
T. Mason, Northwestern University
R. Mathisen, Foster-Miller, Inc., Waltham, MA
B. McConnell, National Renewable Energy Laboratory
P. J. McGinn, University of Notre Dame
D. Moon, Westinghouse, Pittsburgh, PA
F. C. Moon, Cornell University
M. W. Morgan, Ability Engineering Technology, Inc., South Holland, IL
L. Motowidlo, IGC Advanced Superconductors, Inc., Waterbury, CT
W. Nellis, Lawrence Livermore National Laboratory
C. A. Parker, AlliedSignal, Inc., Des Plaines, IL
D. Peterson, Los Alamos National Laboratory
N. Phillips, Lawrence Berkeley Laboratory
R. Raman, Ceracon, Sacramento, CA
R. F. Ranellone, Newport News Shipbuilding, Newport News, VA
R. A. Roehl, Commonwealth Edison Company, Chicago, IL
C. H. Rosner, Intermagnetics General Corp., Latham, NY
R. Schiferl, Reliance Electric, Cleveland, OH
D. K. Sharma, Electric Power Research Institute, Palo Alto, CA
S. Sinha, University of Illinois at Chicago
G. Smith, SSC, Inc., Woodinville, WA
O. Smith, Illinois Superconductor Corp., Evanston, IL
D. M. Smyth, Lehigh University
M. Suenaga, Brookhaven National Laboratory
P. T. Tsivitse, Reliance Electric, Cleveland, OH
R. Weber, Containerless Research, Inc., Evanston, IL
B. Weinberger, United Technologies Research Center, East Hartford, CT
D. O. Welch, Brookhaven National Laboratory
R. E. Williams, Ocean and Atmospheric Science, Inc., Dobbs Ferry, NY
J. Wu, Westinghouse Electric Corporation, Science and Technology Center, Pittsburgh, PA
G. J. Yurek, American Superconductor Corporation, Westborough, MA
C. Zahopoulos, Northeastern University
G. O. Zimmerman, ZerRes Corp., Boston, MA